CERAMIC MEMBRANES FOR HIGH TEMPERATURE HYDROGEN SEPARATION

D. E. Fain and G. E. Roettger

Oak Ridge K-25 Site*
P. O. Box 2003
Oak Ridge, TN 37831-7271

ABSTRACT

Ceramic gas separation membranes can provide very high separation factors if the pore size is sufficiently small to separate gas molecules by molecular sieving and if oversized pores are adequately limited. Ceramic membranes typically have some pores that are substantially larger than the mean pore size and that should be regarded as defects. To assess the effects of such defects on the performance of ceramic membranes, a simple mathematical model has been developed to describe flow through a gas separation membrane that has a primary mode of flow through very small pores but that has a secondary mode of flow through undesirably large pores. This model permits separation factors to be calculated for a specified gas pair as a function of the molecular weights and molecular diameters of the gases, the membrane pore diameter, and the diameter and number of defects. This model will be described, and key results from the model will be presented.

The separation factors of our membranes continue to be determined using a permeance test system that measures flows of pure gases through a membrane at temperatures up to 275 °C. A primary goal of this project for FY 1996 is to develop a mixed gas separation system for measuring the separation efficiency of membranes at higher temperatures. Performance criteria have been established for the planned mixed gas separation system and design of the system has been completed. The test system is designed to measure the separation efficiency of membranes at temperatures up to 600 °C and pressures up to 100 psi by separating the constituents of a gas mixture containing hydrogen. The system will accommodate our typical experimental membrane that is tubular and has a diameter of about 9 mm and a length of about 23 cm. The design of the new test system and its expected performance will be discussed.

INTRODUCTION

The goal of this project is to develop methods for fabricating ceramic membranes that will efficiently separate hydrogen from gasified coal at temperatures of 1,000 °F or higher. Previous work has demonstrated that high separation factors can be achieved with ceramic membranes if the mean pore size is sufficiently small to separate gas molecules by molecular sieving.[1] Since ceramic membranes typically

---

*The Oak Ridge K-25 Site is managed by Lockheed Martin Energy Systems, Inc. for the U.S. Department of Energy under contract No. DE-AC05-84OR21400.

have some pores that are substantially larger than the mean pore size, recent modeling work has sought to determine the effects of oversized pores on separation factors. The separation factors of our membranes have been measured to date using a permeance test system that measures the flows of pure gases through a membrane at temperatures up to 275°C. An important current objective of the project is to develop a mixed gas separation system that will measure the separative performance of membranes with gas mixtures at temperatures up to 600°C.

DISCUSSION OF CURRENT ACTIVITIES

Model for Free Molecule Flow Through an Inorganic Gas Separation Membrane Containing Leaks

Inorganic membranes typically have some pores that are substantially larger than the mean pore size and that should be regarded as leaks or defects. A means to determine the effects of such leaks on the performance of inorganic membranes has been needed. To meet this need, a simple mathematical model has been developed to describe free molecule gas flow through an inorganic membrane containing some undesirable large pores, which will be referred to as leaks. The model was developed to study the effects of leaks on the performance of inorganic gas separation membranes that have small pores and that would be operated at high temperatures. For this case, the equation for free molecule diffusion of a gas through a circular capillary will be used as a starting point. This equation is usually expressed as

$$F = \frac{1}{12} \bar{v} \pi d^3 \frac{T_o \Delta P}{T P_o \ell}, \qquad (1)$$

where

F = flow rate in standard cc per second,

$\bar{v}$ = mean molecular velocity of the gas molecules,

d = mean capillary diameter

T_o = standard temperature,

ΔP = pressure difference across the capillary,

T = temperature,

P_o = standard pressure, and

ℓ = capillary length.

Equation (1) approximates the gas transport through the capillary so long as the pore diameter is large compared to the diameter of the gas molecules. If the effective pore diameter approaches the size of the gas molecules, as is the case with a molecular sieve gas separation membrane, then the size of the gas molecule should be taken into account. If we consider a circular capillary with rigid, smooth walls as a model, then the distance of closest approach of the center of a gas molecule to a wall is the radius of the molecule. Therefore, the effective diameter of the capillary for transport is the difference between the capillary diameter and the molecule diameter. As discussed elsewhere,[2] Eq. (1) then becomes

$$F = \frac{1}{12}\,\bar{v}\pi(d - \sigma)^3\,\frac{T_o \Delta P}{T P_o \ell}\,, \tag{2}$$

where σ is the diameter of the gas molecule.

Equation (2) may be used to describe flow through a gas separation membrane that has a primary mode of flow through very small pores but that has a secondary mode of flow through undesirably large pores, or leaks. Consider a representative section of the membrane containing one leak of diameter d_L and a related number, n, of small pores having mean diameter of d_P. The total gas flow through this representative section of the membrane can be expressed using Eq. (2) as follows

$$F\ total = \frac{n}{12}\,\bar{v}\pi(d_P - \sigma)^3\,\frac{T_o \Delta P}{T P_o \ell} + \frac{1}{12}\,\bar{v}\pi(d_L - \sigma)^3\,\frac{T_o \Delta P}{T P_o \ell}\,, \tag{3}$$

where n is the ratio of the number of small pores per one leak.

Equation (3) may be simplified and expressed as

$$F\ total = \frac{1}{12}\pi\,\frac{T_o \Delta P}{T P_o \ell}\,\bar{v}\left[n(d_P - \sigma)^3 + (d_L - \sigma)^3\right]. \tag{4}$$

The ideal separation factor, α, of a membrane for a binary gas mixture is the ratio of the specific flows (the flow rate per unit pressure difference) of the individual gases. Thus, using Eq. (4), the ideal separation factor can be expressed as

$$\alpha = \frac{\bar{v}_1}{\bar{v}_2}\left[\frac{n(d_P - \sigma_1)^3 + (d_L - \sigma_1)^3}{n(d_P - \sigma_2)^3 + (d_L - \sigma_2)^3}\right] \tag{5}$$

where

$\overline{v}_1, \overline{v}_2$ = mean molecular velocities of gas 1 and gas 2, and

σ_1, σ_2 = molecular diameters of gas 1 and gas 2.*

Since the ratio of the molecular velocities is equivalent to the inverse ratio of the square root of molecular weights, Eq. (5) may be expressed in the more convenient form

$$\alpha = \left(\frac{M_2}{M_1}\right)^{0.5} \left[\frac{n(d_P - \sigma_1)^3 + (d_L - \sigma_1)^3}{n(d_P - \sigma_2)^3 + (d_L - \sigma_2)^3}\right], \tag{6}$$

where M_1, M_2 are the molecular weights of gas 1 and gas 2.

Equation (6) is appropriate assuming $d_P \geq \sigma_1$ and σ_2. In other words, the pore diameter is as large or larger than the molecular diameter of both gas 1 and gas 2, such that both gases will flow through the pores.

If $d_P < \sigma_2$, then there is no flow of the larger gas molecules (gas 2) through the pores. Gas 2 would flow only through the leaks. Thus, for $\sigma_1 < d_P < \sigma_2$

$$\alpha = \left(\frac{M_2}{M_1}\right)^{0.5} \left[\frac{n(d_P - \sigma_1)^3 + (d_L - \sigma_1)^3}{(d_L - \sigma_2)^3}\right]. \tag{7}$$

If $d_P < \sigma_1$, then there is no flow of either gas through the pores. The gases can flow only through the leaks. Thus, for $d_P < \sigma_1$ and σ_2

$$\alpha = \left(\frac{M_2}{M_1}\right)^{0.5} \left[\frac{(d_L - \sigma_1)^3}{(d_L - \sigma_2)^3}\right]. \tag{8}$$

The above equations permit ideal separation factors to be calculated for a specified gas pair as a function of the molecular weights and molecular diameters of the gases, the membrane mean pore diameter, and the diameter and frequency of leaks. The frequency of leaks is expressed by n, the number of pores per each leak. Obviously, a higher value of n represents a lower frequency of leaks.

Finally, for the special case of a membrane that has no leaks, an equation for the ideal separation factor can be derived readily from Eq. (2) as discussed elsewhere.[2] For a membrane having no leaks,

---

*In this model, σ_1 denotes the smaller gas molecule and σ_2 the larger gas molecule.

$$\alpha = \left(\frac{M_2}{M_1}\right)^{0.5} \left[\frac{(d_P - \sigma_1)^3}{(d_P - \sigma_2)^3}\right]. \quad (9)$$

In studying a gas separation membrane containing leaks, it is also useful to determine how much of the gas flow through the membrane occurs through the small pores (as contrasted to the leaks). For a particular gas flowing through a membrane having n small pores per each leak, the ratio of (flow through pores)/(total flow through pores plus leaks) can be readily determined using Eq. (2). Expressed as a percentage rather than a fraction, this percentage for gas 1 is given by

$$\%\ of\ flow\ through\ pores = \frac{100\ n(d_P - \sigma_1)^3}{n(d_P - \sigma_1)^3 + (d_L - \sigma_1)^3}. \quad (10)$$

This equation applies when $d_P \geq \sigma_1$. When $d_P < \sigma_1$, there is no flow through the small pores and the above ratio is zero. The ratio shown in Eq. (10) is illustrated for gas 1 having molecular diameter of σ_1. Clearly, the value of the ratio would be different for gas 2 having a larger molecular diameter, σ_2.

Results from Model Studies

The mathematical model described above permits ideal separation factors to be calculated for inorganic gas separation membranes containing leaks. The model has been used to study the effects of leak size and frequency on the separation factors of membranes having various mean pore sizes. Several examples of model results are presented below for the helium/carbon tetrafluoride (He/CF_4) gas pair, which we commonly use to test membranes.

Separation factors calculated from the model are presented in Fig. 1 as a function of the membrane mean pore size for membranes containing leaks of 2,000 Å (0.2 μm) arbitrary diameter. Plots are shown for a leak frequency (n) of 10^9 pores per leak and 10^7 pores per leak and contrasted with results for a membrane containing no leaks. For the membrane containing no leaks, the separation factor increases continually with declining pore size, and the separation factor becomes infinite when the pore size becomes smaller than the larger gas molecule (4.7 Å for CF_4) but larger than the smaller gas molecule. For the membrane containing 10^9 pores per each 2,000 Å leak, the separation factor is severely limited to

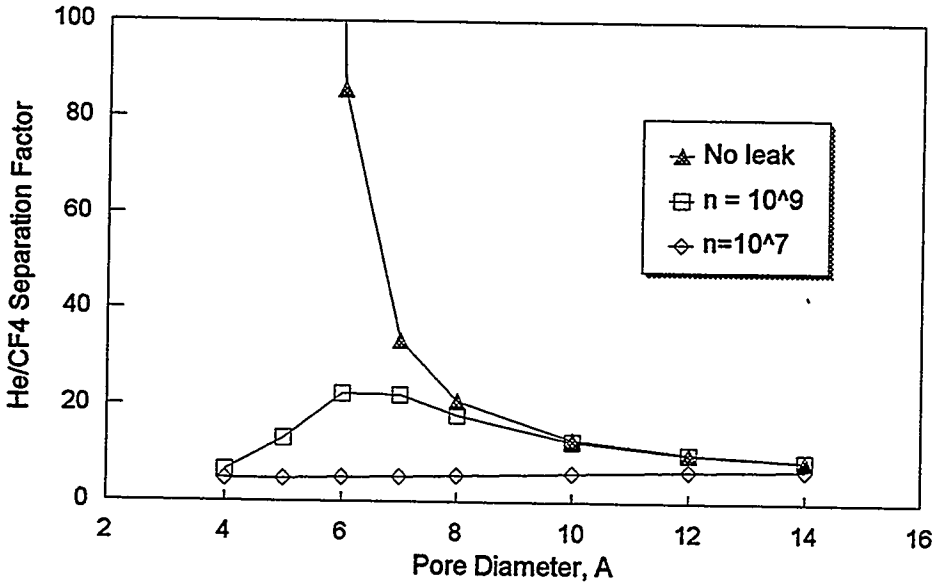

Fig. 1. Model calculated separation factors for He/CF_4 as a function of membrane mean pore size showing the effects of leak frequency (n) for 2,000 Angstrom diameter leaks.

a maximum value of about 22 at a pore size of about 6 Å. Further reduction of pore size below 6 Å actually results in lower separation factors because an increasingly larger fraction of the flow occurs through the leaks as the "good" pores are reduced in size. Calculations using Eq. (10) show 16.6% of the flow through leaks for the 6 Å membrane, and 73.4% of the flow through the leaks for the 4 Å membrane. For the membrane containing only 10^7 pores per each 2,000 Å leak, the separation factor continually declines with decreasing pore size. In this case, 34.8% of the flow is through leaks for the 14 Å membrane, increasing to 99.64% of the flow through leaks for the 4 Å membrane.

Separation factors calculated from the model are presented in Fig. 2 as a function of the membrane mean pore size for membranes containing an arbitrary leak frequency of 10^8 pores per leak. Plots are shown for leak diameters of 2,500 Å, 1,000 Å, and 500 Å, and are contrasted with results for a membrane containing no leaks. The results show that the separation factor achievable by reducing pore size can be severely limited if the size of leaks is large.

Model results presented in Fig. 3 show the effect of leak diameter on separation factor for a membrane having a pore diameter of 6 Å and a leak frequency of 10^8 pores per leak. The results show that the separation factor can be dramatically increased by reducing the leak diameter from 2,500 Å to

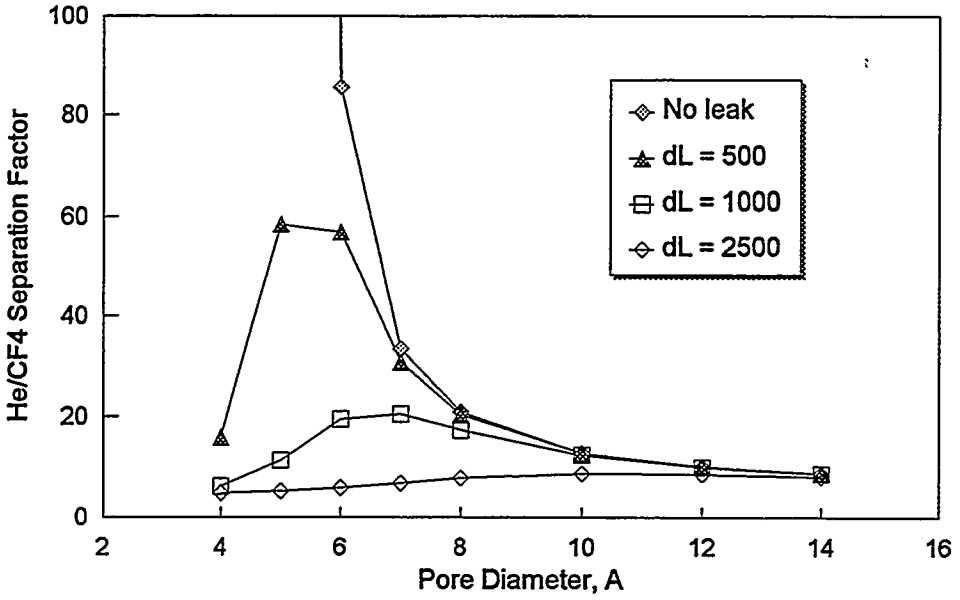

Fig. 2. Model calculated separation factors for He/CF_4 as a function of membrane mean pore size showing the effects of leak diameter (dL) for a leak frequency of 10^8 pores per leak.

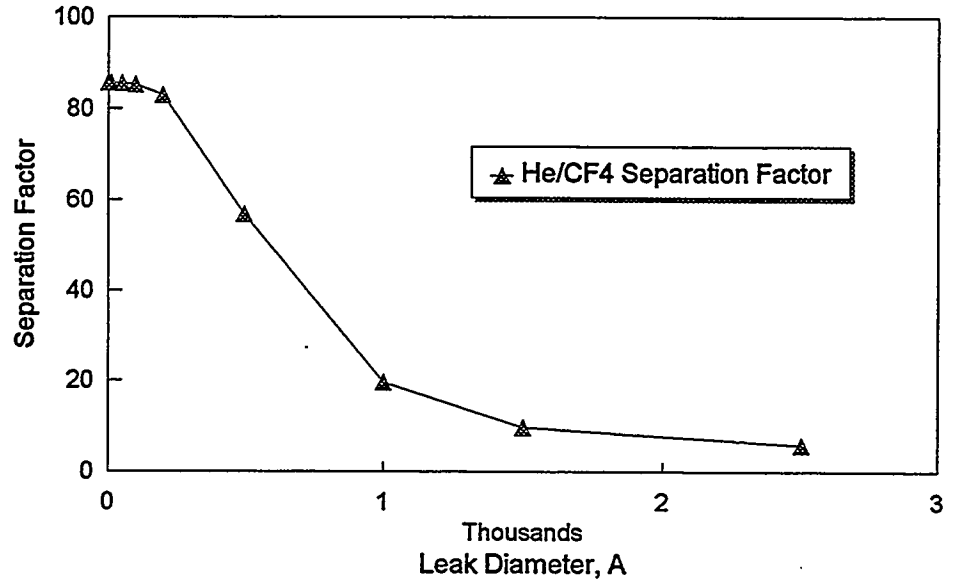

Fig. 3. Model calculated separation factors for He/CF_4 as a function of leak diameter for a membrane having a leak frequency of 10^8 pores per leak and a pore diameter of 6 Å.

about 200 Å. Further reducing the size of the leaks below 200 Å results in only a slight additional increase in separation factor. Various studies performed with the model generally indicate that reducing the size of leaks (in contrast to completely eliminating them) can be a very effective means of increasing separation factors.

Mixed Gas Separation System

The separative performance of our membranes has been determined to date using a permeance test system that measures flows of pure gases through a membrane at temperatures up to 275°C. Using these data, the separation factor of the membrane for a particular gas pair is determined from the ratio of the pure gas specific flows.

An important goal for FY 1996 is to develop a mixed gas separation system for measuring the separation efficiency of membranes at higher temperatures. Performance criteria have been established for the planned mixed gas separation system. The test system will measure the separation efficiency of membranes at temperatures up to 600°C and pressures up to 100 psi by separating the constituents of a gas mixture containing hydrogen. The system will accommodate our typical experimental membrane that is tubular and has a diameter of about 9 mm and a length of about 23 cm. Design of this test system has been completed, and specifications have been developed for system components. A diagram of the system is shown in Fig. 4. The test system has been designed to operate with binary gas mixtures such as hydrogen/methane or hydrogen/carbon dioxide. The mixed gas will be fed into the tubular membrane at pressures up to 100 psi, and the membrane will separate the gas mixture into a permeate stream and a raffinate stream. The membrane will be sealed in a holder mounted in a split tube furnace to permit membrane separations to be evaluated at temperatures up to 600°C. The compositions of the three gas streams will be measured with a gas chromatograph equipped with a thermal conductivity detector. Other variables to be measured include the flow rate of the feed gas stream and the temperatures and pressures of all three of the gas streams. These data taken over a range of flows and pressures will permit the separation efficiency to be determined as a function of the operating conditions and from these data the separation factor can be evaluated.

One of the significant technical challenges involved in designing the test system was to establish a method for sealing a tubular alumina membrane into a metal holder to provide an assembly that would tolerate heating to 600°C. A method has been developed that involves joining a tubular section of a low-thermal-expansion metal alloy to the ends of the porous alumina tube using a glass glazing technique as

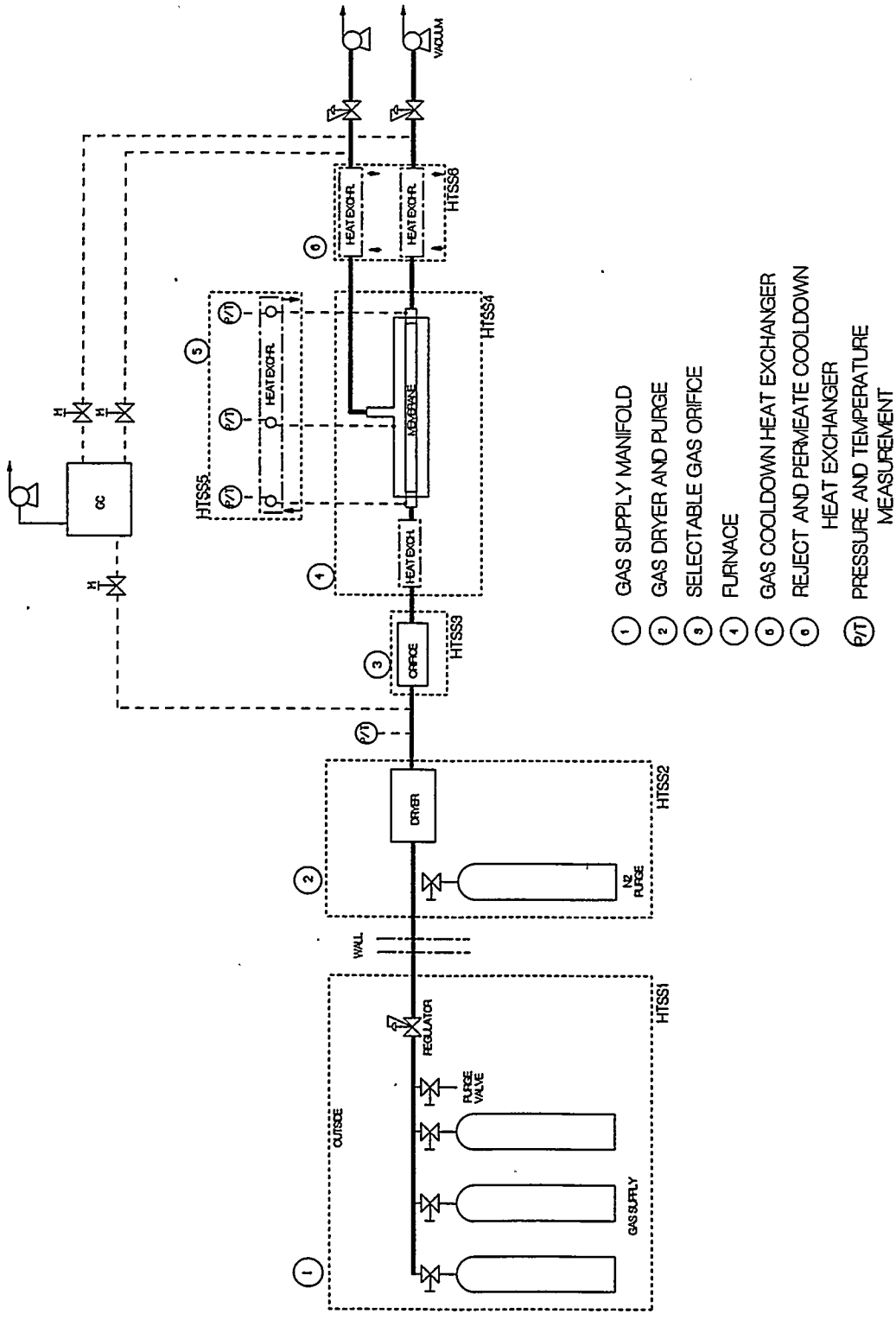

Fig. 4. Diagram of the mixed gas separation system being developed to measure the separation efficiency of membranes at temperatures up to 600°C.

shown in Fig. 5. Several test assemblies have been prepared with the alloy tubing glazed to the end of the ceramic membrane. These glazed assemblies have been thermally cycled to 600°C and back to room temperature as many as six times. The test assemblies have remained leak free following such thermal cycling, indicating that this sealing method should be suitable for use in the test system.

REFERENCES

1. D. E. Fain and G. E. Roettger, "High Temperature Inorganic Membranes for Separating Hydrogen," in *Proceedings of the Ninth Annual Conference on Fossil Energy Materials*, Oak Ridge, Tennessee, May 16-18, 1995, pp. 185-193.

2. D. E. Fain and G. E. Roettger, "Coal Gas Cleaning and Purification with Inorganic Membranes," *Transactions of the ASME*, 115 (3), pp. 628-633 (July 1993).

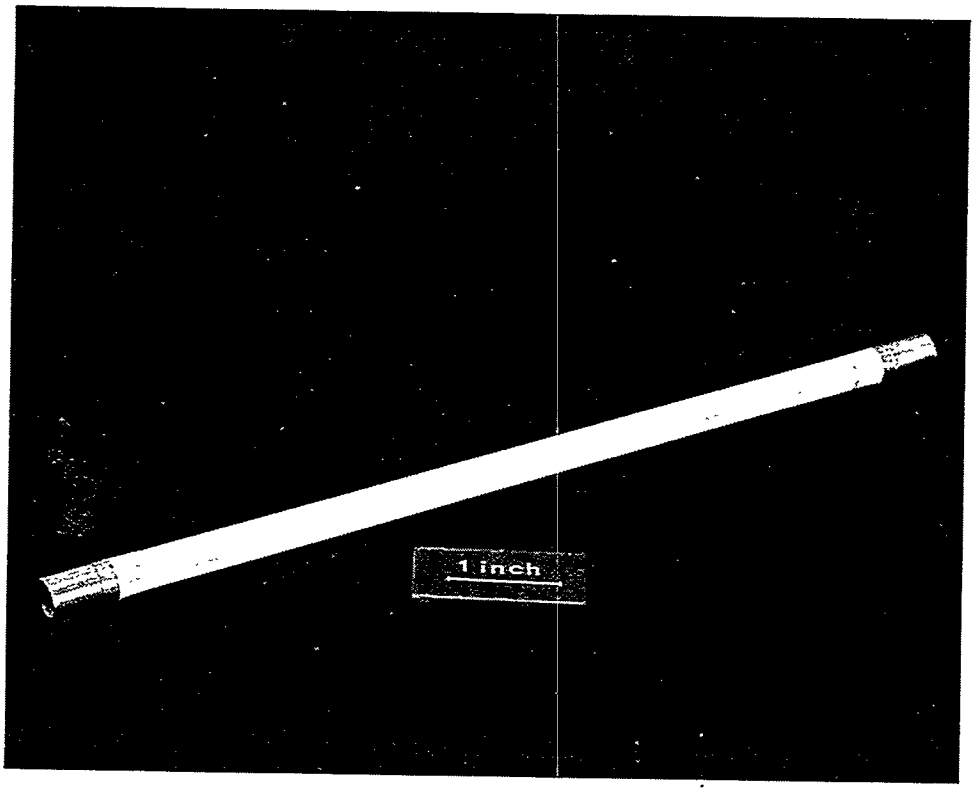

Fig. 5. Metal end pieces glazed to ends of a porous alumina tube.

MIXED OXYGEN ION/ELECTRON-CONDUCTING CERAMICS FOR OXYGEN SEPARATION[1]

J. W. Stevenson, T. R. Armstrong, B. L. Armstrong, J. L. Bates,
G. Hsieh, L. R. Pederson, and W. J. Weber

Pacific Northwest National Laboratory
P.O. Box 999
Richland, WA 99352

ABSTRACT

Mixed oxygen ion and electron-conducting ceramics are unique materials that can passively separate high purity oxygen from air. Oxygen ions move through a fully dense ceramic in response to an oxygen concentration gradient, charge-compensated by an electron flux in the opposite direction. Compositions in the system $La_{1-x}M_xCo_{1-y-z}Fe_yN_zO_{3-\delta}$, perovskites where M=Sr,Ca, and Ba, and N=Mn, Ni, Cu, Ti, and Al, have been prepared and their electrical, oxygen permeation, oxygen vacancy equilibria, and catalytic properties evaluated. Tubular forms, disks, and asymmetric membrane structures, a thin dense layer on a porous support of the same composition, have been fabricated for testing purposes. In an oxygen partial gradient, the passive oxygen flux through fully dense structures was highly dependent on composition. An increase in oxygen permeation with increased temperature is attributed to both enhanced oxygen vacancy mobility and higher vacancy populations. Highly acceptor-doped compositions resulted in oxygen ion mobilities more than an order of magnitude higher than yttria-stabilized zirconia. The mixed conducting ceramics have been utilized in a membrane reactor configuration to upgrade methane to ethane and ethylene. Conditions were established to balance selectivity and throughput in a catalytic membrane reactor constructed from mixed conducting ceramics.

INTRODUCTION

Mixed oxide compositions in the $(La,Sr)(Co,Fe)O_{3-\delta}$ system (ABO_3 perovskite structure) are known to exhibit substantial ionic and electronic conductivity at elevated temperatures.[1-5] This behavior makes them attractive candidate materials for many important applications, including solid oxide fuel cell cathodes, oxygen separation membranes, and membrane reactors for synthesis gas production (carbon monoxide and hydrogen) and the partial oxidation of hydrocarbons. While the ionic conductivity in these materials frequently accounts for less than 1% of the overall electrical conductivity, the magnitude of the ionic conductivity can be quite large relative to other oxygen ion conductors such as yttria-stabilized zirconia. A spontaneous flux of oxygen through fully dense, mixed conducting

[1] Research sponsored by the U. S. Department of Energy, Fossil Energy AR&TD Materials Program. Pacific Northwest National Laboratory is operated by Battelle for the U. S. Department of Energy under Contract DE-AC06-76RLO 1830.

specimens will occur when these materials are placed in an oxygen partial pressure gradient at elevated temperatures. The ionic current resulting from this flux of oxygen ions is compensated internally by an electronic current, so that no electrodes or external circuitry are required for the oxygen flux through the membrane to occur. Passive oxygen flux through a fully dense, mixed conducting ceramic membrane is shown schematically in Figure 1.

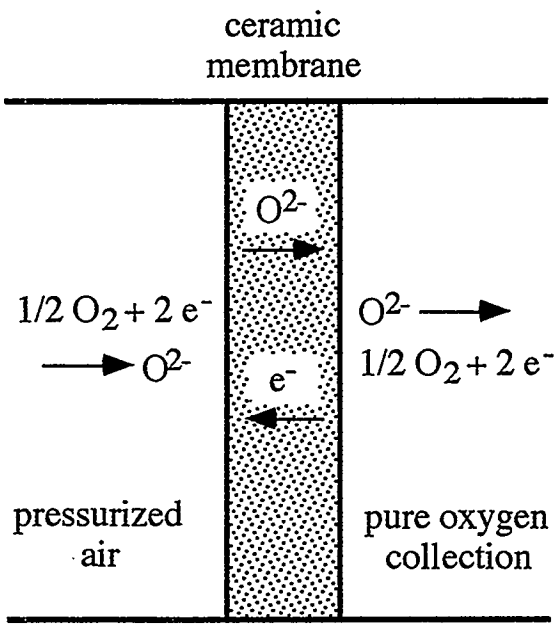

Figure 1. Schematic of oxygen separation using mixed electron and ion-conducting ceramic membranes.

In this study, perovskite compositions in the system $La_{1-x}M_xCo_{1-y-z}Fe_yN_zO_{3-\delta}$, where M=Sr,Ca, and Ba, and N=Mn, Ni, Cu, Ti, and Al, have been prepared and their electrical, oxygen permeation, oxygen vacancy equilibria, and catalytic properties evaluated. The purpose of this work is to develop compositions and forms that support a high oxygen flux, yet retain sufficient chemical and mechanical stability to enable the use of this class of materials as oxygen separation membranes, as membrane reactors operating in dual oxidizing and reducing environments, and as the cathode in a fuel cell operating at intermediate temperatures.

EXPERIMENTAL METHODS

Compositions within the system $La_{1-x}M_xCo_{1-y-z}Fe_yN_zO_{3-\delta}$ (M=Sr,Ba,Ca; $0.4 \le x \le 0.8$; $0.2 \le y \le 0.8$; N=Mn, Ni, Cu, Ti, and Al) were prepared using the glycine-nitrate combustion synthesis technique.[6] After mixing metal nitrate solutions in the appropriate proportions, glycine was added as a fuel and complexant. The resulting mixtures were then heated in stainless steel beakers on a hot plate to the point of combustion. The resulting ash was calcined at 850°C for 12 h in air. The calcined powders were compacted using uniaxial pressure (55 MPa) and then pressed isostatically (138 MPa). The pressed compacts were sintered in air in a $MoSi_2$ furnace using a heating rate of 5°C/min and a cooling rate of 2°C/min; typical sintering conditions to achieve relative densities ≥ 90% were 1150-1250°C for 2-4 h.

Electrical conductivities of sintered bars were measured as a function of temperature (25-1100°C) in air by a 4-point pulsed dc method using platinum electrodes and a heating and cooling rate of 1.6°C/min. Thermogravimetric analyses(TGA) were performed on calcined powder specimens using a heating rate of 5°C/min and a cooling rate of 2°C/min. The TGA measurements were performed in several different atmospheres (dry air; 10,000, 1,000, and 100 ppm O_2 in N_2). Passive (i.e., no applied field) oxygen permeation measurements were performed between 720 and 950°C using sintered disc specimens (nominal dimensions: 20 mm dia. x 2 mm thick) sealed in an alumina test cell with gold gaskets. Oxygen or air was used as the source gas with nitrogen as the carrier gas. An oxygen sensor and mass spectrometer were used in calculating the oxygen fluxes. Phase development was determined by x-ray diffraction analysis using Cu Kα radiation. Semi-quantitative analysis of phase concentrations was based on comparison of observed peak heights after background subtraction. Room temperature oxygen stoichiometries of calcined powder specimens were determined by iodometric titration.[7]

RESULTS AND DISCUSSION

Phase Development

Phase development after calcination in air at 850°C and sintering in air at 1200°C were determined by x-ray diffraction analysis for each of the compositional series. The $(LaSr)(CoFe)O_{3-\delta}$ compositions were essentially single-phase perovskite solid solutions after heating to 850°C, while the calcium and barium-containing compositions typically required higher temperature treatment to yield a high proportion (≥ 95 wt %) of the desired perovskite phase. In the $(LaCa)(CoFe)O_{3-\delta}$ materials, additional phases observed included $Ca_2Fe_2O_5$, $Ca_2Co_2O_5$, $CaFe_3O_5$, and CoO. Compositions of $(LaBa)(CoFe)O_{3-\delta}$ with a Ba content ≥ 0.6 mole fraction contained multiple perovskite-type phases, as well as other phases (e.g., $Ba_5Fe_{14}O_{26}$, $BaCO_3$), after the 850°C calcination. After heat treatment at 1200°C, they were nearly single-phase perovskites, with small quantities of additional phases (e.g., $BaFe_2O_4$, $Ba_2Fe_2O_5$, and $Ba_3Fe_2O_6$).

Oxygen Stoichiometry

All of the materials studied exhibited a substantial reversible weight loss when heated in air. This weight loss upon heating was due to a partial loss of lattice oxygen, so that the

oxygen stoichiometry, 3-δ, decreased with increasing temperature. The magnitude of the oxygen loss during heating was highly dependent on composition, and tended to increase with increasing acceptor (Sr,Ba,Ca) content. The temperature at which oxygen loss began to occur was also highly dependent on the composition, with oxygen loss beginning to occur at lower temperatures as the acceptor content increased. Coupled with iodometric titration results,the oxygen stoichiometry (3-δ) could be determined. Results for $(LaSr)(CoFe)O_{3-\delta}$ are given in Figure 2. Compositions in the series $(LaBa)(CoFe)O_{3-\delta}$ tended to exhibit a higher degree of oxygen non-stoichiometry. Lower oxygen loss found for compositions high in cobalt compared to those compositions high in iron indicate that cobalt is more resistant to oxidation than iron in the perovskite structure. The absence of hysteresis in the TGA results during heating and cooling at different rates indicates that the materials were close to their equilibrium oxygen contents during the measurements.

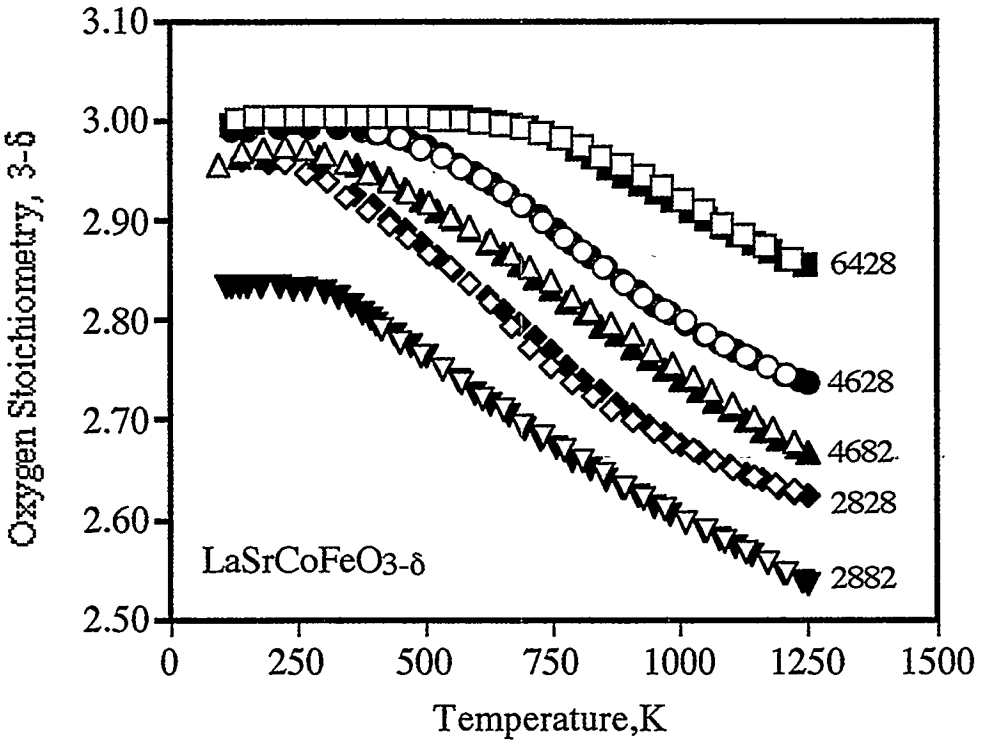

Figure 2. Oxygen stoichiometry as a function of temperature for the indicated $LaSrCoFeO_{3-\delta}$ compositions, measured in air. Open symbols refer to heating data; closed symbols refer to cooling data.

Electrical Conductivity

Electrical conductivities for each compositional series were determined as a function of temperature using the 4-probe dc method. Because the ionic transport number in these compositions is low (typically less than 1%), the bulk conductivities obtained by these dc 4-probe measurements were representative of the electronic conductivity of the materials. The conductivity was enhanced by increasing the Co content; this result is consistent with previous studies on acceptor-doped $LaFeO_3$ and $LaCoO_3$.[8, 9] Activation energies ranged from 0.03-0.29 eV. This behavior is consistent with small polaron conduction, with localized electronic carriers having a thermally activated mobility.

At higher temperatures, a substantial decrease in electronic conductivity with increasing temperature was observed. When a divalent acceptor (e.g., Sr) is substituted for trivalent La, electroneutrality requires that the effective negative charge of the Sr cations be compensated by an increase in valence of some of the B-site cations (electronic compensation) and/or the formation of oxygen vacancies (ionic compensation). Electronic compensation results in an increase in the average valence of the transition metal cations, while ionic compensation reduces the oxygen stoichiometry. At low temperatures, the charge compensation for $La_{0.6}Sr_{0.4}Co_{0.2}Fe_{0.8}O_{3-\delta}$ is primarily electronic, with a substantial fraction of B-site cations being converted from the trivalent to the tetravalent state due to the presence of the acceptor cations. At higher temperatures, ionic compensation becomes significant, while the electron hole population is lowered.

Oxygen Permeation and Ionic Conductivity

Oxygen permeation rates through sintered specimens of several $(LaSr)(CoFe)O_{3-\delta}$ compositions are shown as a function of temperature in Figure 3. The specimen thickness was ≈2 mm. Oxygen or air was the source gas on the high $P(O_2)$ side, with nitrogen being used as the carrier gas. In the $(LaSr)(CoFe)O_{3-\delta}$ compositions, the oxygen flux increased significantly with increasing Sr content,. Oxygen flux also increased with increasing temperature, attributed to an increase in the mobility of the lattice oxygen vacancies (the hopping of vacancies from site to site is thermally activated), as well as the increase in the concentration of lattice oxygen vacancies. Fluxes for the $(LaCa)(CoFe)O_{3-\delta}$ compositions were much lower than for the $(LaSr)(CoFe)O_{3-\delta}$ compositions. Barium-substituted compositions gave oxygen fluxes comparable to those containing a like concentration of Sr, and higher fluxes than those containing Ca.

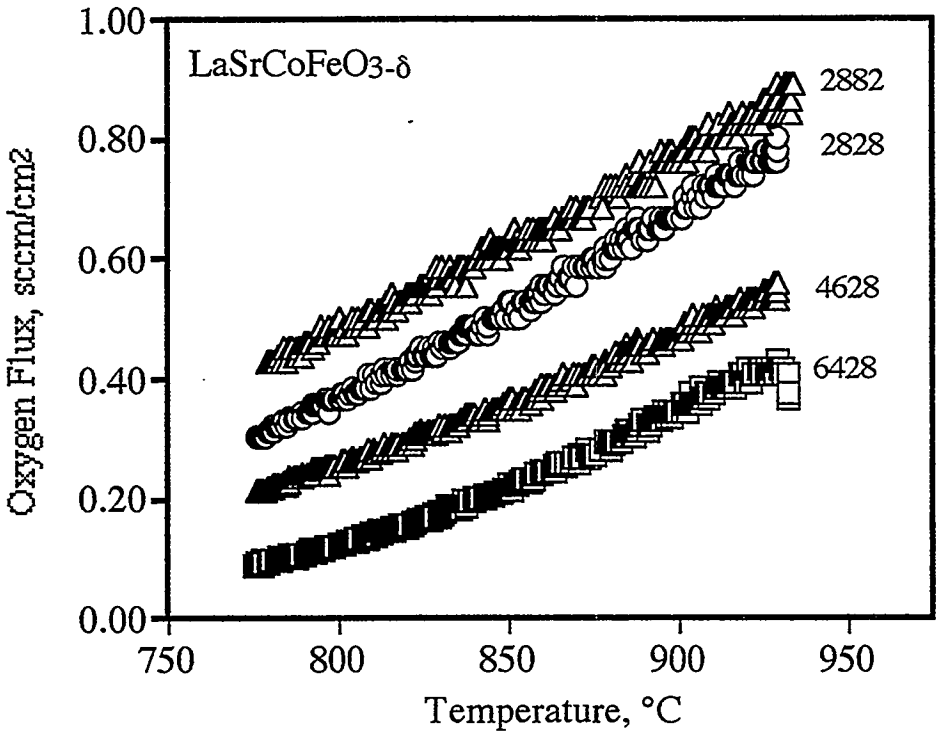

Figure 3. Oxygen permeation as a function of temperature through sintered specimens of the indicated $LaSrCoFeO_{3-\delta}$ composition. The membrane thickness was approximately 2 mm for each composition, while the oxygen partial pressure gradient was approximately 10.

The oxygen flux through the bulk of a mixed conducting membrane should be inversely proportional to the thickness of the membrane. Thus, to maximize oxygen flux, the membrane thickness should be minimized. Very thin, self-supporting membranes of this type are mechanically very weak and of little practical importance. When thin films were prepared on a porous MgO or Al_2O_3 support, differences in thermal expansion behavior resulted in membrane cracking. A promising alternative approach is to fabricate an asymmetric membrane structure, consisting of a thin, dense membrane on a porous support of the same composition, by tape calendering. An organic phase was included in the ceramic powder plus plasticizer mixture that formed a porous structure during burnout. The porous support allowed relatively free transport of oxygen to the dense membrane surface, and provided much needed mechanical support. Because the support and dense membrane consisted of the same composition, there was no thermal expansion mismatch. A micrograph

of a cross-section of an $LaSrCoFeO_{3-\delta}$-6428 membrane is given in Figure 4. Molecular oxygen fluxes as a function of temperature for an approximately 2 mm thick and an approximately 15 μm thick asymmetric membrane are given in Figure 5, along with calculated fluxes for different membrane thicknesses. An improvement of approximately two orders of magnitude was realized for the 15 μm thick membrane compared to the 2 mm thick membrane.

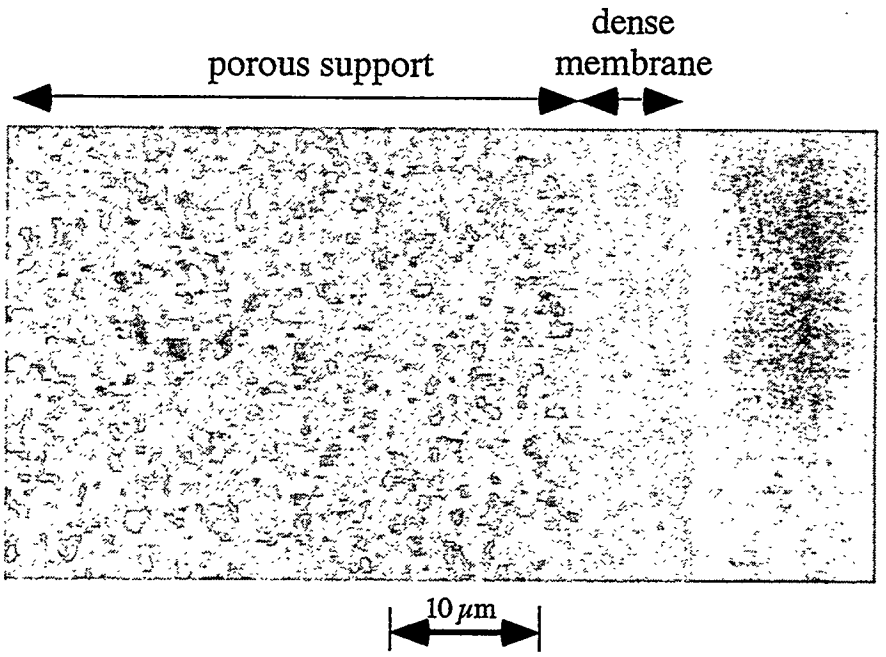

Figure 4. Asymmetric membrane structure consisting of a fully dense layer on a porous support of the same composition, made by tape calendering.

At some point, however, surface exchange kinetics will become rate limiting, so that any further reduction in membrane thickness will not result in an increase in the oxygen flux. Bouwmeester et al.[10] calculated the characteristic thickness of various membrane compositions, below which oxygen permeation is controlled by surface exchange kinetics. The characteristic thickness for Sr-doped $LaCoO_3$ and $LaFeO_3$ varied from 20 to 500 μm at 900°C.

If a material is to be a successful candidate for oxygen membrane applications, it must exhibit long-term phase stability under the membrane operating conditions. In general, the perovskite systems evaluated in this study do not exhibit high stability towards reducing atmospheres at elevated temperatures, typical of membrane reactor applications. These materials are stable under oxidizing condtions, typical of oxygen separation devices. A

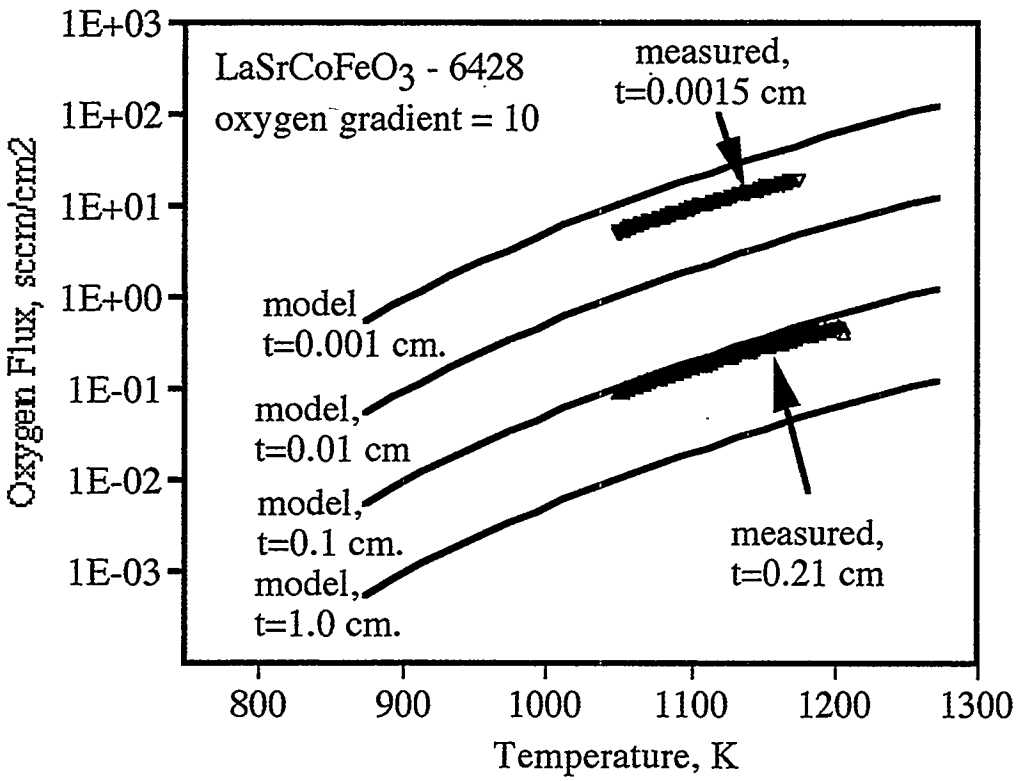

Figure 5. Oxygen flux versus temperature for two different thicknesses of the composition $LaSrCoFeO_3$-6428. Oxygen flux is inversely proportional to membrane thickness, to a limit imposed by surface processes.

membrane of composition $La_{0.2}Sr_{0.8}Co_{0.2}Fe_{0.8}O_{3-\delta}$ operated for 340 h in an oxygen gradient of 10 at 775°C with minimal decrease in oxygen flux (<5 %), as given in Figure 6. Similarly, $La_{0.6}Sr_{0.4}Co_{0.2}Fe_{0.8}O_{3-\delta}$ gave an essentially constant flux at 800°C for nearly 1400 h. These observations are in contrast to the results of a study by Kruidhof et al.[11] for a related composition ($La_{0.6}Sr_{0.4}CoO_{3-\delta}$) at a slightly lower temperature, 750°C. The observed long-term stability indicates that the oxygen fluxes measured during the oxygen permeation trials in this study were true fluxes through the membrane rather than false transient fluxes resulting from oxygen depletion of the perovskite lattice.

From the rates of oxygen permeation, membrane thicknesses, and oxygen partial pressure gradients, oxygen ion conductivities were calculated. Activation energies for oxygen ion conductivities varied from approximately 0.6 to 1.8 eV, depending on composition, as given in Table 1. The activation energies reflect not only the mobility of oxygen ions in the solid, but also the formation of oxygen vacancies at elevated temperatures.

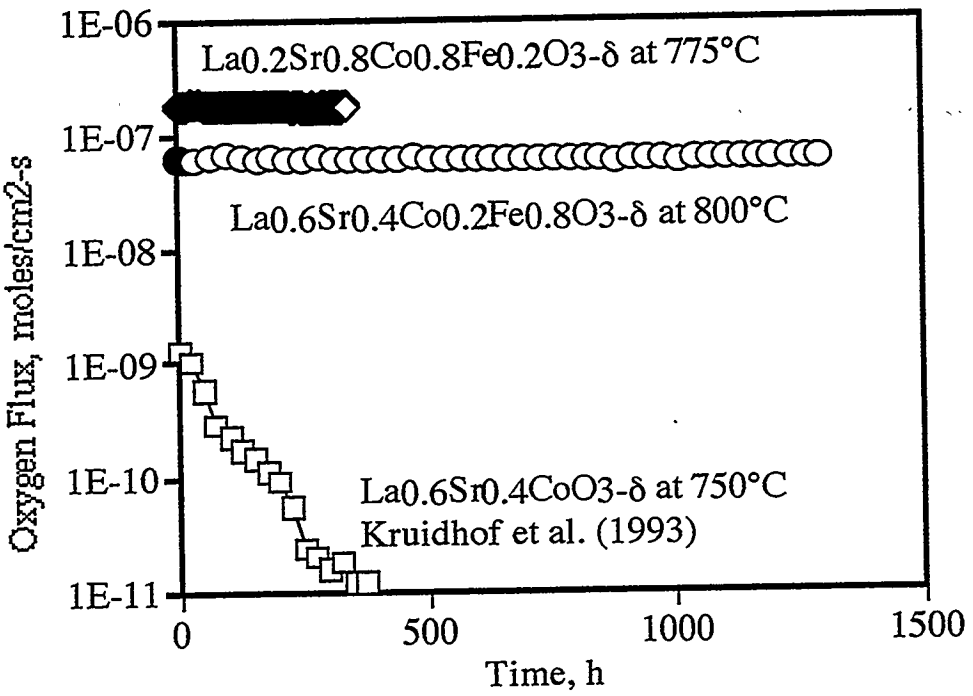

Figure 6. Long-term oxygen flux measurements for several mixed conductor compositions.

Table 1. Ion Conductivities at 900°C and Activation Energies for Oxygen Ion Conduction for Mixed Electron and Ion-Conducting Membranes

Composition	Ionic Conductivity at 900°C (ohms-cm)	Activation Energy (eV)
$La_{0.6}Sr_{0.4}Co_{0.2}Fe_{0.8}O_{3-\delta}$	0.23	1.30
$La_{0.4}Sr_{0.6}Co_{0.2}Fe_{0.8}O_{3-\delta}$	0.40	0.95
$La_{0.2}Sr_{0.8}Co_{0.2}Fe_{0.8}O_{3-\delta}$	0.62	0.85
$La_{0.2}Sr_{0.8}Co_{0.8}Fe_{0.2}O_{3-\delta}$	0.87	0.66
$La_{0.4}Ca_{0.6}Co_{0.2}Fe_{0.8}O_{3-\delta}$	0.03	0.70
$La_{0.4}Ca_{0.6}Co_{0.8}Fe_{0.2}O_{3-\delta}$	0.01	1.80
$La_{0.6}Ba_{0.4}Co_{0.2}Fe_{0.8}O_{3-\delta}$	0.01	1.64
$La_{0.4}Ba_{0.6}Co_{0.2}Fe_{0.8}O_{3-\delta}$	0.33	0.90
$La_{0.2}Ba_{0.8}Co_{0.2}Fe_{0.8}O_{3-\delta}$	0.37	0.65
$La_{0.6}Sr_{0.4}Co_{0.2}Fe_{0.6}Al_{0.2}O_{3-\delta}$	0.15	0.83
$La_{0.6}Sr_{0.4}Co_{0.2}Fe_{0.6}Cr_{0.2}O_{3-\delta}$	0.03	1.63
$La_{0.6}Sr_{0.4}Co_{0.2}Fe_{0.6}Cu_{0.2}O_{3-\delta}$	0.10	1.34
$La_{0.6}Sr_{0.4}Co_{0.2}Fe_{0.6}Ni_{0.2}O_{3-\delta}$	0.10	0.84
$La_{0.6}Sr_{0.4}Co_{0.2}Fe_{0.6}Ti_{0.2}O_{3-\delta}$	0.04	1.34

SUMMARY

Perovskite ceramics in the system $La_{1-x}M_xCo_{1-y-z}Fe_yN_zO_{3-\delta}$, where M=Sr,Ca, and Ba, and N=Mn, Ni, Cu, Ti, and Al, have been prepared and their electrical, oxygen permeation, oxygen vacancy equilibria, and catalytic properties evaluated. These materials exhibit mixed electron and oxygen ion conductivity, and are useful as oxygen separation membranes, fuel cell cathodes, and membrane reactors. Highly acceptor-doped compositions resulted in oxygen ion mobilities more than an order of magnitude higher than yttria-stabilized zirconia. An asymmetric membrane structure was fabricated by tape calendering, consisting of a fully dense, thin layer on a porous support of the same composition. This arrangement provided a high molecular flux, yet was mechanically robust. Little degradation in molecular flux was found for times up to approximately 2 months for most compositions.

REFERENCES

1. T. Ishigaki, S. Yamauchi, K. Kishio, J. Mizusaki, and K. Fueki, *J. Solid State Chem.* 73, 179 (1988).

2. Y. Teraoka, H. Zhang, K. Okamoto, and N. Yamazoe, *Mat. Res. Bull.* 23, 51 (1988).

3. Y. Teraoka, T. Nobunaga, K. Okamoto, N. Miura, and N. Yamazoe, *Solid State Ionics* 48, 207 (1991).

4. J. W. Stevenson, T. R. Armstron, R. D. Carneim, L. R. Pederson, and W. J. Weber, *J. Electrochem. Soc.* (1996, in press).

5. U. Balachandran, S. Morissette, J. Picciolo, J. Dusek, and R. Peoppel, Proc. International Gas Research Conference, Ed. H. Thompson, Government Institutes, Rockville, MD, p. 565 (1992).

6. L.A. Chick, L.R. Pederson, G.D. Maupin, J.L. Bates, L.E. Thomas, and G.J. Exarhos, *Materials Letters* 10, 6 (1990).

7. R. Nadalin and W. Brozda, *Analytica Chimica Acta* 28, 282 (1963).

8. J. Mizusaki, T. Sasamoto, W. Cannon, and H. Bowen, *J. Am. Ceram. Soc.* 66, 247 (1983).

9. J. Mizusaki, J. Tabuchi, T. Matsuura, S. Yamauchi, and K. Fueki, *J. Electrochem. Soc.* 136, 2082 (1989).

10. H. Bouwmeester, H. Kruidhof, and A. Burggraaf, *Solid State Ionics* 72, 185 (1994).

11. H. Kruidhof, H. Bouwmeester, R. v. Doorn, and A. Burggraaf, *Solid State Ionics* 63-65, 816 (1993).

PREPARATION AND EVALUATION OF COAL EXTRACTS AS PRECURSORS FOR CARBON AND GRAPHITE PRODUCTS

J. W. Zondlo, A. W. Stiller, and P. G. Stansberry
West Virginia University, Department of Chemical Engineering
P. 0. Box 6101
Morgantown, WV 26506-6101

I. C. Lewis, R. T. Lewis, and H. K. Mayer
UCAR Carbon Company Inc.
P. 0. Box 6116
Cleveland, OH 44101

ABSTRACT

A coal extraction process coupled with coal hydrotreatment has been shown capable of producing suitable precursors for a variety of commercially important carbon and graphite products. The N-methylpyrolidone (NMP) extracts of hydrotreated coals have been analytically and chemically characterized and shown to have properties acceptable for use as binder and impregnation pitch. Mesophase formation studies have demonstrated their capability for producing both needle and anode grade coke as well as precursors for mesophase pitch fibers. A graphite artifact has been produced using a coal extract as a binder and coke derived from the extract as a filler. Further evaluation of the extract materials is being carried out by industrial members of the Carbon Products Consortium.

I. WVU Extraction Process and Preparation of Coal Extracts

For the past eight years, workers in the Chemical Engineering Department at West Virginia University have been developing a technique based on solvent extraction of coal whereby significant quantities of the organic material in coal can be separated from the inorganic contaminants([1]). The process employs a novel class of organic compounds known as dipolar aprotic solvents. When bituminous coal is treated with these solvents at their normal boiling point, much of the carbonaceous material in the coal is solubilized and the inorganic matter remains as an undissolved solid. Through simple filtration the solution is separated from

the residual inorganic solids and the organic material is reconstituted by evaporation of the solvent. Through efficient use of evaporative technologies, virtually all of the solvent is recovered and recycled in the process.

It has been found that for most bituminous coals indigenous to the Appalachian region, extract yields in the range of 30 to 50% by weight of the original coal can be realized. Moreover, if the raw coal is first treated by mild hydrogenation, extract yields high as 80% can be achieved. Most importantly, by adjusting processing conditions and/or blending extracts. A variety of extracts with different properties can be obtained.

A successful program was completed for the U. S. Department of Energy in which cokes produced from the solvent extraction process were utilized as feedstocks for the production of fine-grained, isotropic, graphite[2]. Furthermore, the program demonstrated that precursors suitable for a number of other carbon products could be produced from the process.

The objective of this present program was to establish the suitability of the extracts as precursors for commercially significant carbon products including the following: binder pitch, impregnating pitch, needle coke for electrodes, anode grade coke, carbon/carbon matrices, and a precursor for mesophase pitch. The ultimate evaluation of materials would be made by Industrial Partners of a Consortium formed for investigation of coal-based precursors for carbon products.

This study reports results for materials prepared by the extraction of hydrotreated coals with N-methylpyrrolidone (NMP) solvent. Two different sub-bituminous West Virginia coals were employed in the process. Initially, the coals were hydrogenated in a one-liter autoclave using 2,000 psi hydrogen and temperatures of 350-450 in both the presence and absence of a catalyst. Tetralin was employed as a hydrogen donor.

The hydrogenated coal was transferred to a rotary evaporator to remove unreacted tetralin. After tetralin removal, N-methylpyrrolidone was added to the mixture and agitated at 140°C for 1 hour. The NMP-hydrogenated-coal slurry was then transferred to a centrifuge to separate the solids. Finally, NMP soluble coal extract was isolated from the NMP by rotary evaporation and then vacuum dried. Larger-size samples were produced using 1-gallon autoclaves. Typically, 600g of powdered coal and 1.8L tetralin were placed into the stirred reactor and pressurized to 2,000 psig, initial cold hydrogen pressure. Between 3 and 4 hours were required to reach final temperature after which several more hours were needed to reach ambient temperature. The extract separations were performed similarly to the small-scale samples.

II. Characterization of Coal Extracts

The NMP extracts prepared at WVU from hydrotreated coals were characterized by a variety of analytical techniques including: elemental C, H, N, O, S, analysis, thermogravimetric analysis (TGA), Proton NMR, solvent extraction with toluene and trichlorobenzene (TCB), Mettler softening point measurement, determination of modified Conradson carbon content (MCC), and Gel Permeation Chromatography (GPC) for evaluation of molecular weight distribution (MWD). Mesophase formation studies were also carried out by direct observation on the microscope hot stage and by separate heat treatment for subsequent examination by polarized light microscopy. Although these evaluations were performed for a variety of extract materials, prepared using different reaction conditions, results are reported here only for NMP extracts from coal hydrotreated at 450°C. These products were found to be the most suitable for the wide variety of carbon products encompassed by the Consortium Team.

Two different West Virginia bituminous coals designated as WVGS-13421 and WVGS-13423 were hydrotreated at 450°C for 2 hours without use of a catalyst. The NMP extracts obtained in 70-85% yields were then characterized in detail. The analytical results are summarized in Table I.

Table I
Properties for NMP Coal Extracts of Hydrotreated Coals

	450°C - 2 Hrs. Coal 13421	450°C - 2 Hrs. Coal 13423
SP, °C	104.7	115.3
MCC %	52.9	51.7
TGA Yd%	34	31
C, %	88.9	89.6
H, %	5.85	5.78
C/H Ratio	1.28	1.30
N, %	2.20	1.90
O, %	2.74	2.49
S, %	0.45	0.33
Ar H %	45	48
Mn (GPC)	367	389
Mesophase (μ)	272	136

The Mettler softening points and carbon yield (MCC) values are in the range of commercially produced binder and impregnant pitches. However, in addition to being solids free, these extracts differ in a number of properties from conventional pitches. The very low aromatic hydrogen contents from NMR, reflect the extensive hydrogenation of aromatic ring systems during the coal pretreatment. The extracts also have substantially higher N and O contents than standard coal tar or petroleum-derived pitches. The molecular weight distributions are comparable to those of commercial pitches.

III. Mesophase Evaluation of Coal Extracts

The nature of the formed mesophase is a suitable guide for the applicability of these extracts for many different carbon precursors. The extracts were heat treated for mesophase domain size evaluation using a published technique[3]. The results are listed in Table I and as can be seen, the WVGS-13421 gave a substantially larger domain size than the WVGS-13423 extract. The large domain size of 272μ is comparable to that found for needle coke precursors for high-performance graphite electrodes and is in the range of materials suitable for mesophase pitch fibers. This large domain size is surprising in view of the high-oxygen content of the extract. A high-oxygen content has been believed to be detrimental for mesophase formation in coal extracts.

IV. Fabrication of Graphite Artifacts from Hydrotreated Coal Extracts

We produced a graphite artifact using coke derived from the WVGS-13421 extract as the filler and the coal extract itself as the binder. The raw coke was prepared at WVU and then calcined to 1,100°C by T. Burchell at the Oak Ridge Laboratory. The calcined coke was mixed with 1/3 by weight of the coal extract binder and then extruded to produce 19mm-diameter rods. The rods were baked and graphitized to 3,000°C. The properties measured for the graphitized rods were the following:

Coefficient of Thermal Expansion (CTE) = 0.26×10^{-6}/°C

Specific Resistance = 9.55 micro-ohm-meters

Density = 1.38/gcc

The very low CTE value of 0.26 is similar to that measured for electrode graphite derived from petroleum needle coke.

V. Activation of Coal Extraction Residues

The economics of the coal extraction process would be improved if the extraction residues also had some value. For this purpose, we attempted to activate these materials to produce a high surface area carbon. We obtained samples of the NMP extraction residue of raw coal WVGS-13421, as well as the extraction residue of the coal hydrotreated at 450°C for 2 hours. Both materials were activated in an H_2O/N_2 mixture at 900°C using a tumbling furnace.

After activation, the measured surface area for the activated residue from the untreated coal was 770 m^2/gm while that for the hydrotreated coal was 212 m^2/gm. The lower surface area of the hydrotreated residue is expected since it would have a greater ash content than the residue from the untreated coal.

VI. Conclusions

Our evaluation studies have demonstrated that the coal extraction process coupled with hydrotreatment can produce materials that are suitable for use as pitches, coke precursors, or mesophase raw materials. We have also demonstrated that coke derived from hydrotreated coal extract can be used to produce graphite with a low coefficient of thermal expansion, a requisite for graphite electrodes. By altering the processing conditions and the use of blends, it would be possible to produce graphites with varying degrees of anistropy. Additionally, the extraction residue can

be activated to produce an activated carbon. No other known process has the flexibility for producing this range of carbon materials.

REFERENCES

1. K. Renganathan, J. W. Zondlo, E. A. Mintz, P. Kneisl, and A. H. Stiller, Fuel Proc. Tech., 18, p. 273 (1988).

2. Coal-Based Nuclear Graphites for the NP Gas-Cooled Reactors, USDOE Contract DE-FG02-91NP00159.

3. R. T. Lewis, I. C. Lewis, R. A. Greinke, and S. L. Strong, Carbon 25, 289 (1987).

A NOVEL APPROACH TO THE REMOVAL OF CO_2

T. D. Burchell, R. R. Judkins, M. R. Rogers, and A. M. Williams

Oak Ridge National Laboratory
P.O. Box 2008
Oak Ridge, TN 37831-6088

ABSTRACT

The removal of CO_2 from gas streams is becoming increasingly significant in the field of energy production. A porous monolithic activated carbon material (CFCMS) has been developed that is both strong and rigid, yet is permeable, and thus offers little resistance to the free-flow of fluids. The material has a unique combination of properties, including reasonable compressive strength, electrical conductivity, a large micropore volume, and a large CO_2 adsorption capacity. At 30°C and atmospheric pressure, CFCMS has a CO_2 uptake >100 mg/g. The uptake is reduced at elevated temperatures, dropping to ~40 mg/g at 100°C. However, the CO_2 uptake increases substantially with pressure, such that at 25°C and 58 bar the mass of CO_2 adsorbed is >490 mg/g. The ability of CFCMS to selectively remove CO_2 from a CO_2/CH_4 gas mixture is demonstrated in a series of breakthrough experiments. The unique combination of properties of CFCMS has been exploited to effect the rapid desorption of CO_2 under the influence of a low applied dc voltage.

INTRODUCTION

The removal of CO_2 is of significance in several energy applications. The combustion of fossil fuels, such as coal or natural gas, releases large volumes of CO_2 to the environment. Several options exist to reduce CO_2 emissions, including substitution of nuclear power for fossil fuels, increasing the efficiency of fossil plants, and capturing the CO_2 prior to emission to the environment. All of these techniques have the attractive feature of limiting the amount of CO_2 emitted to the atmosphere, but each has economic, technical, or societal limitations. In the production of natural gas, the feed stream from the well frequently contains contaminants and diluents which must be removed before the gas can enter the pipeline distribution system. Notable amongst these diluent gasses is CO_2, which has no calorific value. Currently, the pipeline specification calls for <2 mol % CO_2 in the gas. Gas separation is thus a relevant technology in the field of energy production. A novel separation system based on a parametric swing process

has been developed that utilizes the unique combination of properties exhibited by our carbon fiber composite molecular sieve (CFCMS).

The CFCMS is a monolithic activated carbon composed of petroleum pitch-derived carbon fiber and a phenolic resin-derived binder[1-3]. Routinely, fiber microporosity with surface areas >1000 m^2/g are obtained using pitch fibers. The binder phase content is quite low and provides a monolithic structure by bonding the fibers at contact points only, thus rendering the CFCMS macroporous. The CFCMS offers, therefore, a highly adsorbent material with very little resistance to bulk gas flow. Experiments conducted at ORNL have shown the CFCMS to have a high affinity for carbon dioxide compared to zeolites and conventional granular activated carbons. The CFCMS also allows certain equipment variations not possible with granular materials. It can be molded into almost any shape, i.e., shape is constrained only by the ability to fabricate molds, where constraints appear to be minimal. The CFCMS can be machined by skilled operators using conventional tooling. These features permit the activated carbon to be formed to a desired shape to meet process equipment constraints as opposed to conventional filling of vertically-oriented vessels with granular carbon. Granular carbon systems are also subject to attrition due to abrasive wear in service, and channeling of the gas being processed as a result of inhomogeneous packing in the beds. Use of the CFCMS would permit the employment of, for example, horizontally-oriented vessels with controlled flow of the natural gas with the contaminants/diluents to be adsorbed through the adsorbent without risk of channeling and bypass flows.

The CFCMS is, as a result of the continuity of the fiber-matrix unit, electrically conductive. Advantage has been taken of this property to develop a novel desorption process we have termed electrical (or voltage) swing adsorption. On saturation of the CFCMS with, for example, carbon dioxide, immediate desorption can be accomplished by application of very low voltages (in our experiments we have used 0.5-1 volt) across the adsorbent. There are many important operational implications of this desorption process. The system pressure and temperature do not have to be altered as they do in other parametric swing processes such as pressure swing adsorption (PSA) or temperature swing adsorption (TSA). The electrical swing adsorption process is extremely fast in comparison to PSA or TSA. It is an inherently low-energy process compared to the energy requirements of PSA or TSA processes. All of these features suggest a great deal of system and operational simplicity. We present below the results of several experiments which demonstrate the performance of the CFCMS and the electrical swing adsorption process.

EXPERIMENTAL

The CFCMS material used in this study was fabricated using a process initially developed by the U. S. Department of Energy (USDOE) for the production of thermal insulators for NASA space missions[4]. The CFCMS synthesis route has been described in detail previously[1]. Isotropic pitch-derived carbon fibers are mixed with powdered phenolic resin to form a water slurry. The slurry is transferred to a molding tank and the water drawn through a porous screen under vacuum. The resultant green artifact is dried, cured at 60°C in air, and stripped from the mold screen. The composite is cured at ~150°C in air prior to carbonization at 650°C in an inert gas. The final synthesis stage involves activation of the composite in moisture saturated He in the temperature range 800-950°C.

Porosity characterization was performed using nitrogen adsorption and mercury intrusion. Nitrogen adsorption isotherms were measured at 77 K using our Autosorb-1 instrument. Micropore size analysis used a variety of methods, including the Brunauer, Emmett, and Teller (BET)[5] method for surface area and the Dubinin-Astakhov (DA)[6] method for micropore radius and the t-method for micro-pore volume. CO_2 and CH_4 adsorption isotherms for CFCMS were also obtained using the Autosorb-1 apparatus over the pressure range 0.1 to 760-mm Hg and at temperatures of 30, 60, and 100°C. High pressure CO_2 and CH_4 adsorption data (850 psi max.) were obtained using a gravimetric apparatus, courtesy of Westvaco Corporation.

A schematic diagram of our experimental breakthrough apparatus is shown in Fig. 1. The feed gas flows through a CFCMS sample (25.4-mm diameter and 76.2-mm long) to a vent. A sample of the downstream gas is fed to a mass spectrometer allowing on-line monitoring of the exit gas composition. Flowmeters (F1 & F2) are positioned either side of the CFCMS sample. Electrical leads are connected to each end of the sample creating an electric circuit through the sample which allows an electric current to flow. On saturation of the CFCMS with, for example, carbon dioxide, immediate desorption can be accomplished by application of very low voltages (in our experiments we have used 0.5-1 volt) across the adsorbent.

RESULTS AND DISCUSSION

Our previous gravimetric studies of CO_2 adsorption indicated that at 25°C and atmospheric pressure CFCMS can adsorb >100 mg of CO_2 per gram of CFCMS[7,8]. Here we

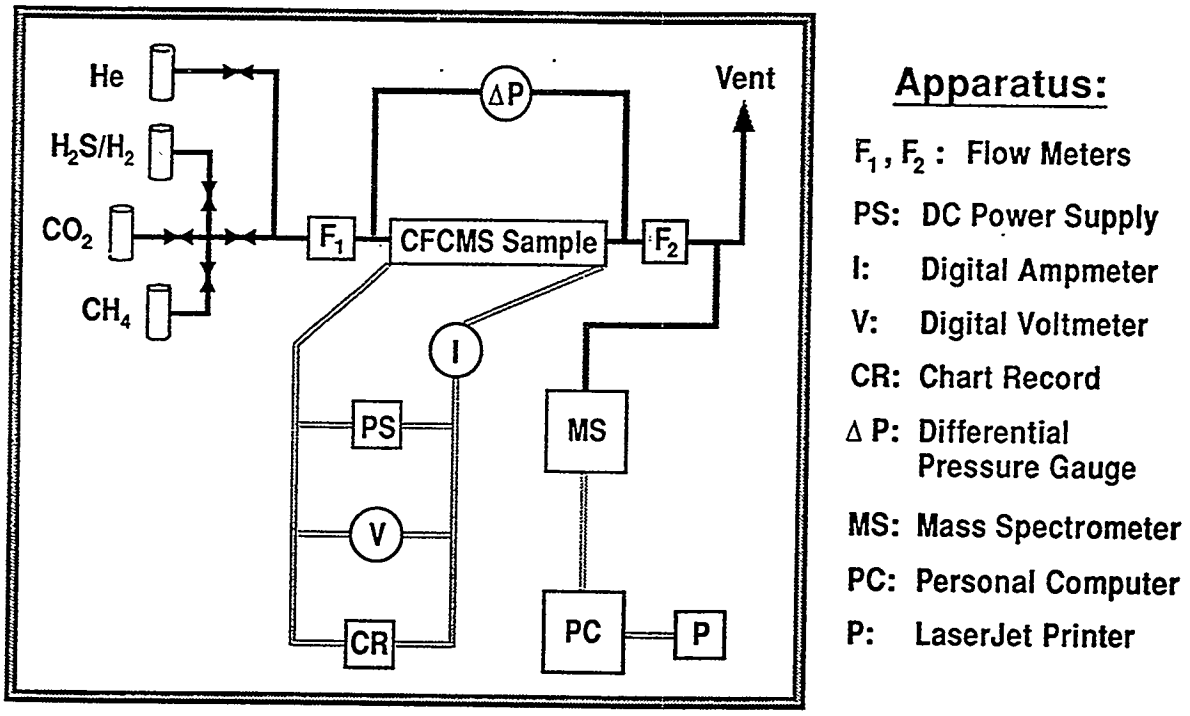

Fig. 1. Schematic drawing of our experimental breakthrough apparatus.

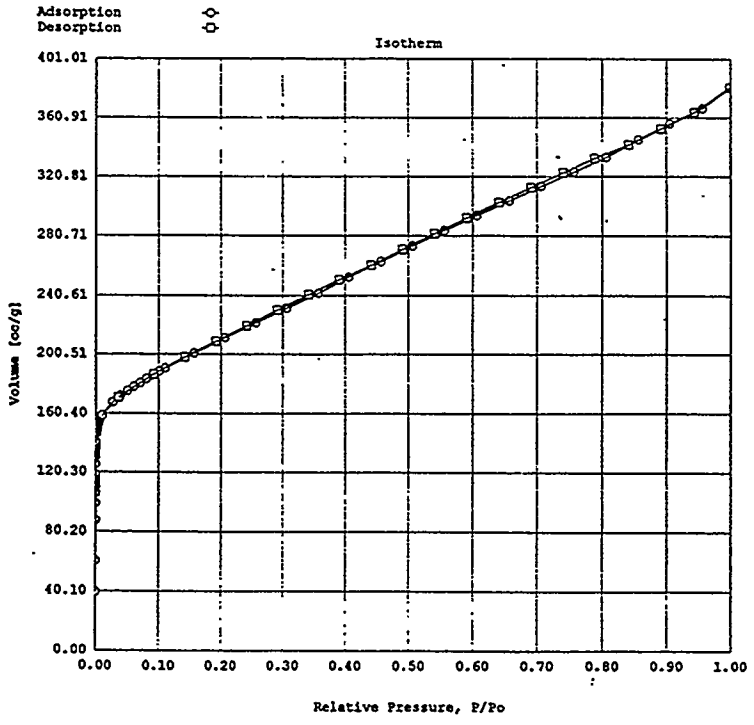

Fig. 2. Nitrogen adsorption isotherm at 77K on CFCMS activated to 9% burn-off.

report the extension of our CO_2 adsorption data to higher temperatures and pressures. Moreover, breakthrough experiments were conducted to determine the efficacy of CFCMS at separating CO_2 from CH_4.

Micropore Structure Analysis

A series of CFCMS cylinders was prepared and activated to burn-offs ranging from 9 to 36% and the BET surface area and micropore size/volume determined from the N_2 adsorption isotherms. Table 1 reports the mass and average burn-off for each of the four cylinders (25-mm diameter x 75-mm length), and their BET surface area, micropore volume (t-method), and mean micropore radius (DA method). Samples were taken from the top (T) and bottom (B) of each cylinder for analysis. Where the measured BET surface areas were widely different between the top and bottom of the cylinders a repeat measurement was performed.

Table 1. Micropore analysis data for activated CFCMS samples.

Specimen	Mass (g)	Burn-off (%)	BET Area (m^2/g)	Pore Volume [t-method] (cm^3/g)	DA Pore Radius (nm)
21-11 T	11.96	9	485	-	0.70
21-11 B	11.96	9	540	0.212	0.65
21-2B T	11.01	18	770	0.282	0.72
21-2B B	11.01	18	1725	0.603	0.70
21-2B B (repeat)	11.01	18	961	0.328	0.71
21-2D T	9.86	27	939	0.305	0.75
21-2D B	9.86	27	2470	0.866	0.75
21-2D B (repeat)	9.86	27	2477	0.791	0.75
21-2C T	8.86	36	923	0.235	0.87
21-2C B	8.86	36	2323	0.723	0.75
21-2C B (repeat)	8.86	36	856	0.270	0.75

The BET surface area increases with burn-off, approaching 2500 m^2/g at >25% burn-off. The micropore size (DA pore radius) is apparently less sensitive to burn-off (Table 1) and increases only slightly over the weight loss range reported here. The pore volume (t-method) varies with the BET surface area, increasing with burn-off. The observed variations in BET surface area and micropore volume and radius are in agreement with our previous data[8]. In addition to the data reported above, a density function theory (DFT) analysis was performed on the N_2 adsorption isotherm for sample 21-11B. The isotherm (Fig. 2) is a "type I" isotherm[9], as were all the isotherms obtained for our CFCMS materials. Figure 3 shows the DFT analysis results, which indicate a micropore (<2-nm width) distribution centered at approximately 0.4-0.5-nm radius. This value is somewhat smaller than DA pore radii reported in Table 1, but agrees well with our previously published DR method pore width data for CFCMS with similar burn-offs[8]. The pore volume attributable to the micropores is also shown in Fig. 3. Summing the volume elements for pore half widths <10Å yields a micropore volume of approximately 0.16 cm^3/g, which is in reasonable agreement with the "t-method" micropore volume data in Table 1 for CFCMS samples 21-11 B and T.

CO_2/CH_4 Adsorption Studies

Adsorption isotherms were obtained at temperatures of 30, 60, and 100°C at pressures up to one atmosphere for CO_2 and CH_4 (Figs. 4 and 5). Both of the CFCMS samples analyzed (21-11 and 21-2B) adsorbed less CO_2 at 60 and 100°C than at 30°C. At 100°C the amount of CO_2 adsorbed was approximately one third that adsorbed at 30°C. Both CFCMS specimens displayed similar trends with respect to CH_4 adsorption. CFCMS has a greater uptake of CO_2 compared to CH_4 at all of the temperatures studied here. For example, at 30°C approximately 50 cm^3/g of CO_2 was adsorbed whereas only approximately 27 cm^3/g of CH_4 was adsorbed at one atmosphere pressure. Figure 6 shows the variation of the amount of gas adsorbed (CO_2 or CH_4) at one atmosphere pressure with temperature for two CFCMS specimens. The greater selectivity of specimen 21-11 at 30°C is apparent. However, the selectivity of the two specimens is very similar at 60 and 100°C.

Figure 7 shows CO_2 adsorption isotherms for CFCMS specimens 21-11 and 21-2B over the pressure range 0.5-59 bar (8-850 psi), and CH_4 adsorption isotherms for the same specimens over the pressure range 0.5-39 bar (8-560 psi). The measured volumetric (Fig. 6) and gravimetric (Fig. 7) adsorption capacities at one atmosphere for both CH_4 and CO_2 are in good agreement

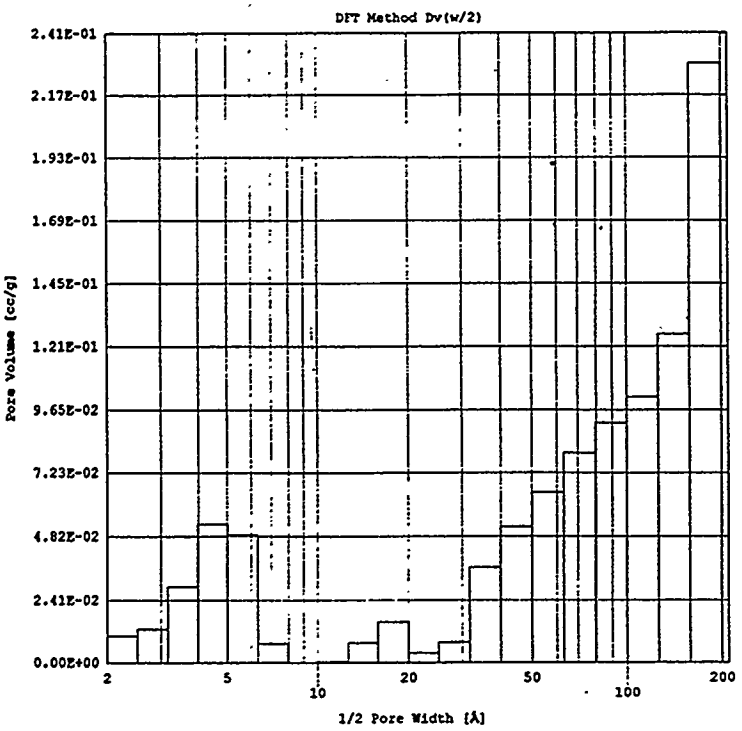

Fig. 3. DFT micropore size analysis of nitrogen adsorption isotherm at 77K on CFCMS (9% burn-off).

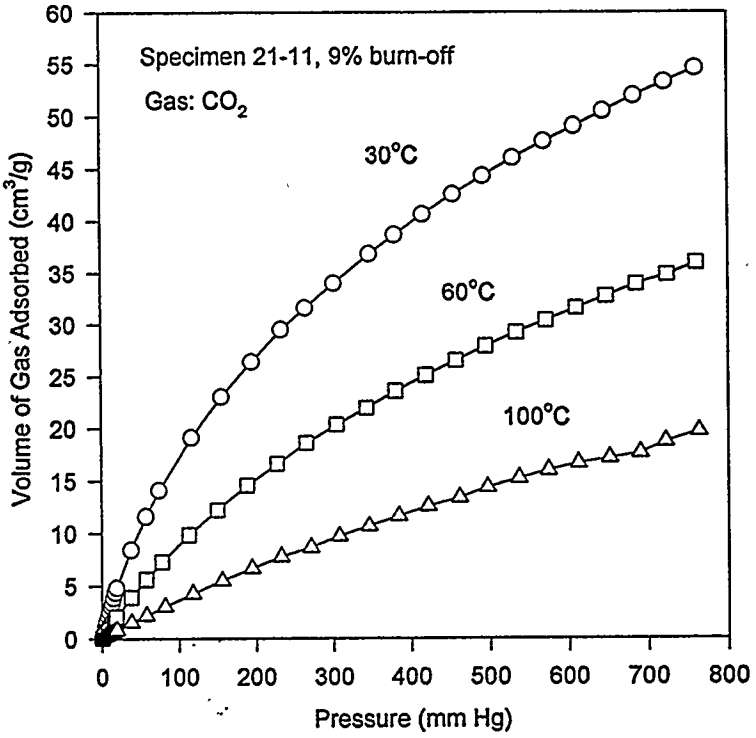

Fig. 4. Carbon dioxide adsorption isotherms at 30, 60, and 100°C on CFCMS (9% burn-off).

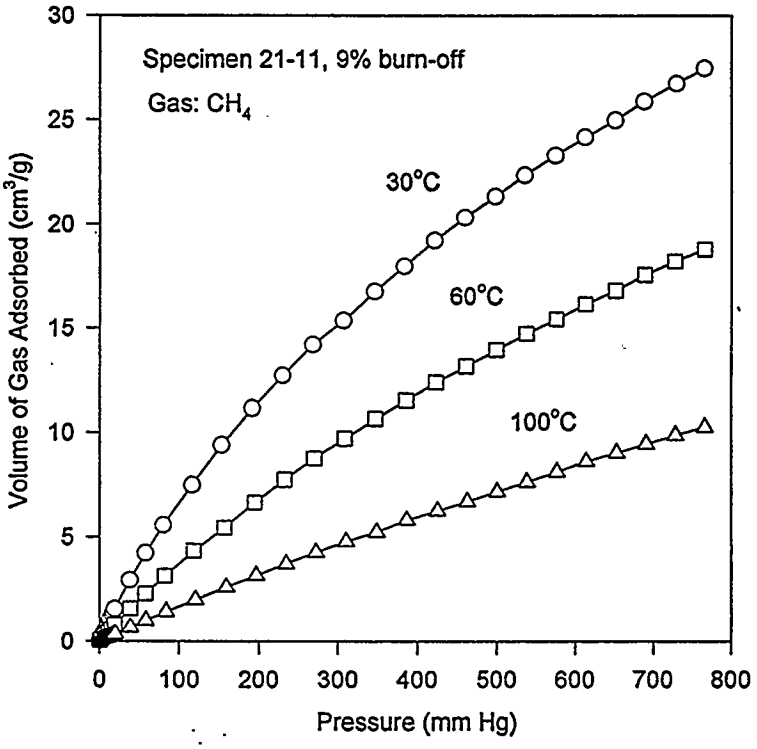

Fig. 5. Methane adsorption isotherms at 30, 60, and 100°C on CFCMS (9% burn-off).

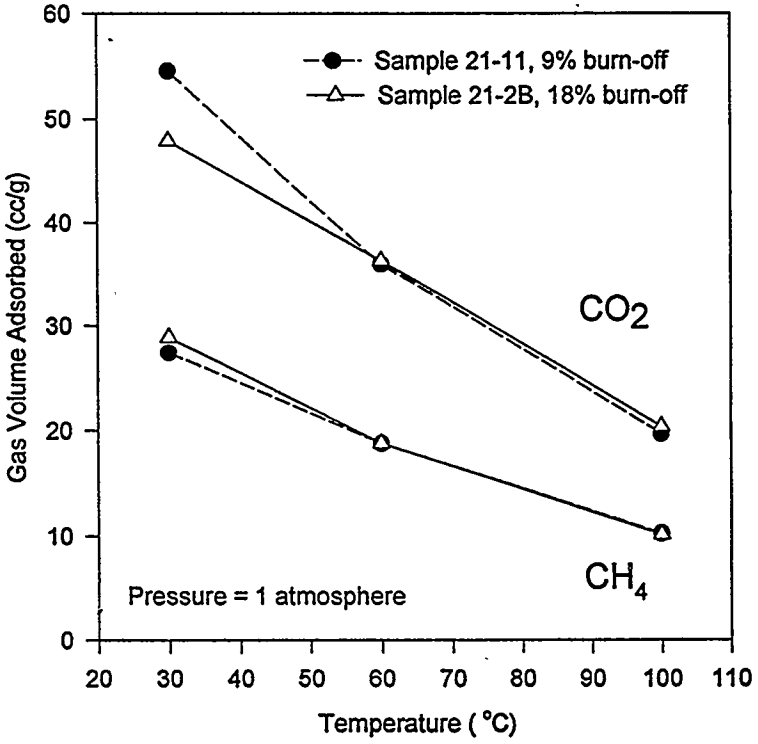

Fig. 6. A comparison of CO_2 and CH_4 gas adsorption for CFCMS at different burn-offs as a function of adsorption temperature.

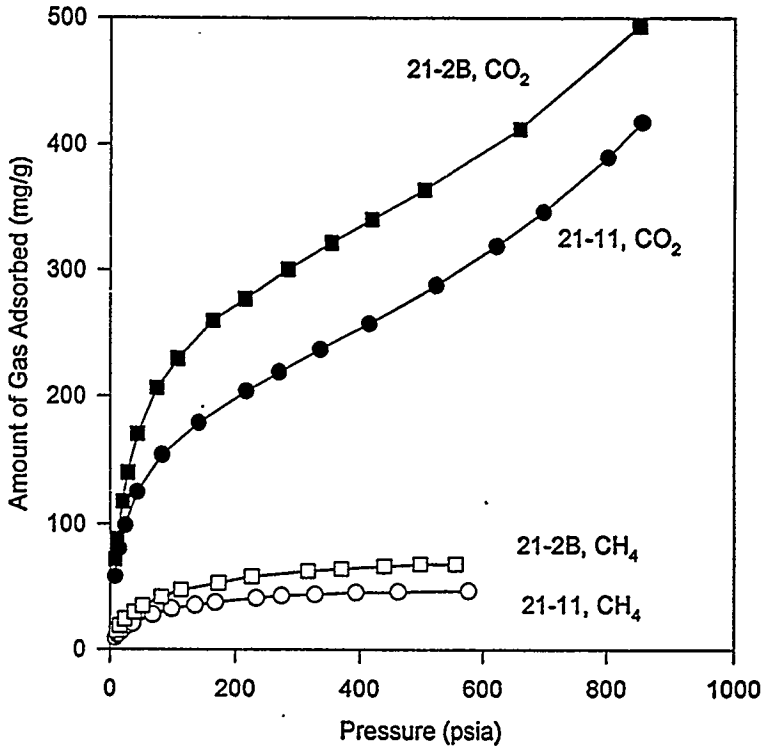

Fig. 7. High pressure CO_2 and CH_4 adsorption isotherms on CFCMS.

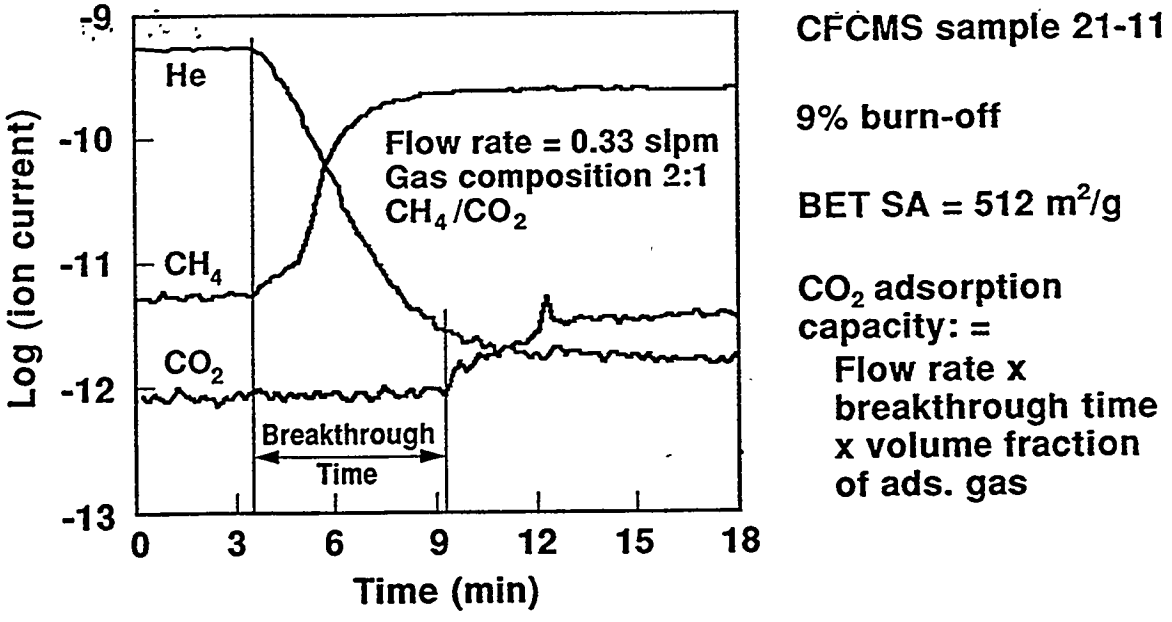

Fig. 8. Typical CO_2/CH_4 breakthrough plots on CFCMS sample 21-11 (9% burn-off).

for the CFCMS specimens. At one atmosphere, approximately 100 mg of CO_2 per g of CFCMS and approximately 19 mg of CH_4 per g of CFCMS were adsorbed. The quantities of gas adsorbed rose to >490 mg/g (CO_2 on specimen 21-2B) and >67 mg/g (CH_4 on specimen 21-2B). Moreover, the CO_2 isotherms are still increasing with pressure whereas the CH_4 isotherms have flattened (i.e., the CFCMS has become saturated with CH_4). However, the data in Fig. 7 clearly shows that CFCMS exhibits selective adsorption of CO_2 over CH_4.

The CO_2 adsorption data discussed above suggests that CFCMS might provide for the effective separation of CO_2 from CH_4. To determine the efficacy of CFCMS for this purpose, several steam activated samples were tested in the breakthrough apparatus (Fig. 1) described previously. A typical breakthrough plot for a CH_4/CO_2 mixture is shown in Fig. 8. Any entrained air is initially driven out with a He purge. The input gas is then switched to a 2:1 mixture of CH_4/CO_2 at a flow rate of 0.33 slpm. The outlet stream He concentration decreases and the CH_4 concentration increases rapidly (i.e., CH_4 breaks through). Adsorption of CO_2 occurs and, therefore, the CO_2 concentration remains constant at a low level for approximately six minutes before the CO_2 concentration begins to increase, i.e., "breakthrough" occurs. Table 2 reports data from our preliminary study of CO_2 separation. CO_2 capacities are reported as determined from pure CO_2 and CO_2/CH_4 mixtures on each specimen examined. The reported CO_2 capacities are the means of several repeats of the breakthrough experiments, and the BET surface areas are the means of the data reported in Table 1. Two of the CFCMS samples (lowest burn-off) had CO_2 adsorption capacities of almost one liter on 0.037 liters of adsorbent, and only a small capacity reduction was observed in the CO_2/CH_4 gas mixture. The CO_2 adsorption capacity decreases with increasing burn-off, in agreement with the isotherm data.

A Novel Gas Separation System

CFCMS has a continuous carbon skeleton which imparts electrical conductivity to the material. The carbon fibers used in the synthesis of CFCMS have, according to their manufacture, an electrical resistivity of 5 milliohm.cm. Figure 9 is a plot of the current-voltage characteristics of a 2.5-cm diameter, 7.5-cm long CFCMS cylinder. The plot is linear, indicating that in CFCMS electrical conduction obeys ohm's law. At an applied dc potential of one volt, approximately 5 amps flows through the CFCMS. The CFCMS samples electrical resistance is thus 0.2 ohm and the resistivity is 131 milliohm.cm. This resistivity is considerably greater than that of the fibers, and is attributed to contact resistance and the lower electrical conductivity of

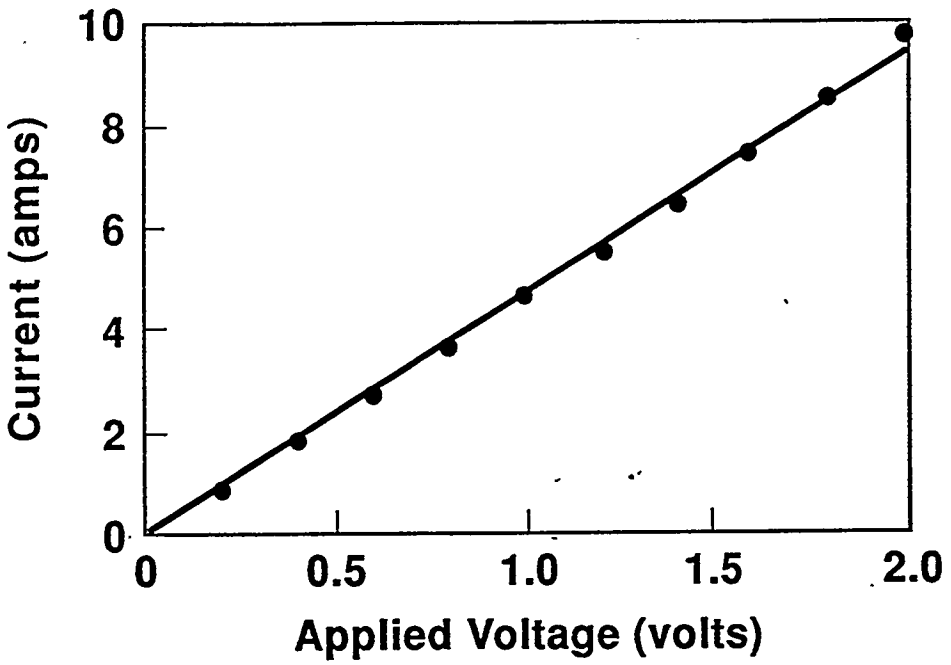

Fig. 9. The current-voltage relationship for CFCMS (sample 21-2B, 18% burn-off, 25-mm diameter x 76-mm length)

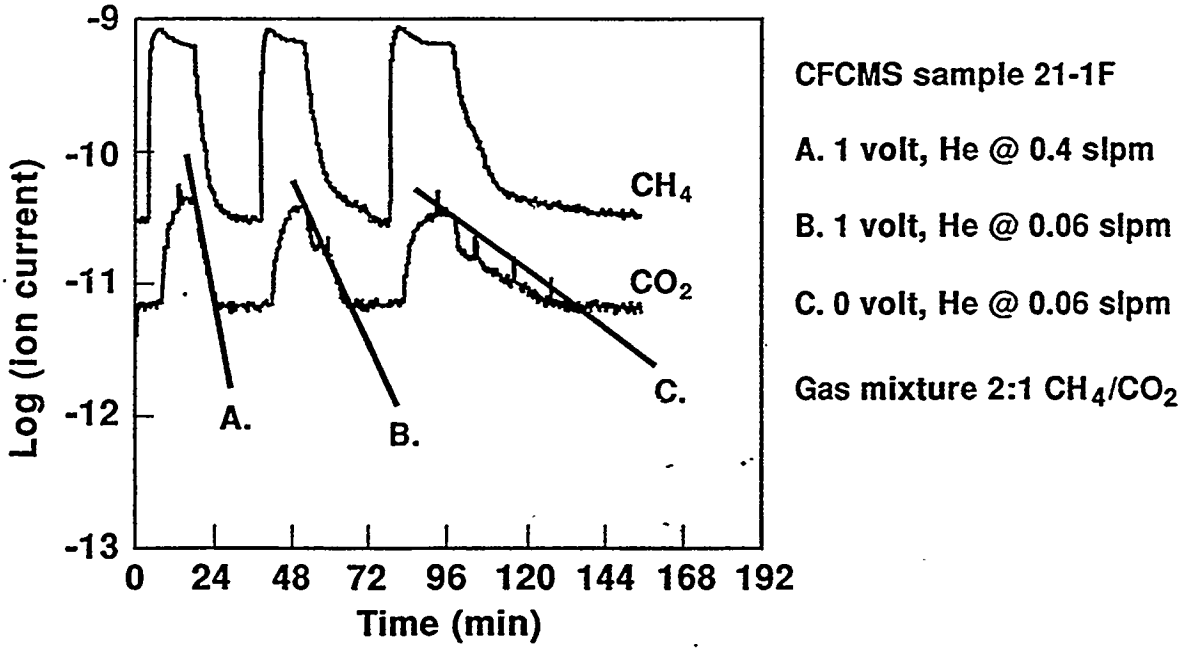

Fig. 10. CO_2/CH_4 breakthrough plots on CFCMS showing the benefit of electrically enhanced desorption.

the phenolic resin derived carbon binder. A consequence of the passage of an electric current through the CFCMS is a heating effect, which causes the CFCMS to increase in temperature to approximately 50-60°C.

Table 2. CO_2 separation data from our CO_2 and CO_2/CH_4 breakthrough experiments.

Specimen No.	Burn-off (%)	BET Surface Area (m^2/g)	CO_2 Capacity (Liters)	
			CO_2/CH_4	CO_2 only
21-11	9	512	0.73	0.97
21-2B	18	1152	0.45	0.98
21-2D	27	1962	0.39	0.80
21-2C	36	1367	0.35	0.80

We have utilized the electrical properties of CFCMS to effect a rapid desorption of adsorbed gases in our breakthrough apparatus. The process has been named electrically enhanced desorption, and the benefit of this technique is shown in Fig. 10 where the CO_2 and CH_4 gas concentrations in the outlet gas stream of our breakthrough apparatus (Fig. 2) are shown as a function of time. Three adsorption/desorption cycles are shown in Fig. 10. In the first and second cycles (A and B in Fig. 10) desorption is caused by the combined effect of an applied voltage (1 volt) and a He purge gas. In the third cycle (C in Fig. 10) desorption is caused only by the He purge gas. A comparison of cycles B and C indicated that the applied voltage reduces the desorption time to less than one third of that for the He purge gas alone (cycle C). Clearly, the desorption of adsorbed CO_2 can be rapidly induced by the application of an electric potential. We postulate two explanations for this effect. First, the passage of an electric current through the CFCMS causes an increase in the materials temperature, which in turn thermally excites the adsorbed gas, effecting the desorption. Second, the flow of electrons through the CFCMS disrupts the weak dispersion or polar attractive forces which bind the gas in the micropores. The ability of CFCMS to selectively adsorb CO_2 from a CH_4/CO_2 mixture, combined with the electrically enhanced desorption of the CO_2, allow for a gas separation system where the separation is effected by electrical swing, rather than the more conventional pressure or temperature swings.

CONCLUSIONS

A porous monolithic activated carbon material (CFCMS) has been developed that is strong, rigid, and which overcomes problems associated with operation using granular adsorbents. The open structure of CFCMS results in a permeable material which offers little resistance to the free-flow of fluids. The material has a unique combination of properties, including reasonable compressive strength, electrical conductivity and a large micropore volume.

CO_2 and CH_4 isotherms have been obtained for samples of CFCMS both volumetrically and gravimetrically. At 30°C and atmospheric pressure the CFCMS material has a CO_2 uptake of >50 cm^2/g (>100 mg/g). The CO_2 uptake is reduced at elevated temperature, and falls to approximately 20 cm^2/g (40 mg/g) at 100°C. However, the adsorption of CO_2 increases with increasing pressure such that at 58 bar the mass of CO_2 adsorbed increases to >490 mg/g. Similar trends were observed for CH_4 adsorption on CFCMS, except that the adsorption capacity was much less.

A series of breakthrough experiments was performed on CFCMS specimens and their ability to selectively remove CO_2 demonstrated. The unique combination of properties of CFCMS has been exploited to effect the rapid desorption of CO_2 from the materials. It has been shown that for adsorbent configuration reported here a 4-5 amp current flowing under an applied dc voltage of one volt causes a rapid desorption of the CO_2.

REFERENCES

1. T. D. Burchell. Carbon Fiber Composite Molecular Sieves, In *Proceedings of Eighth Annual Conference on Fossil Energy Materials*, Oak Ridge, Tennessee, U.S.A., May 1994. ORNL/FMP-94/1, CONF-9405143, pp. 63-70. Pub. Oak Ridge National Lab, U.S.A., August 1994.

2. T. D. Burchell, C. E. Weaver, F. Derbyshire, Y. Q. Fei, and M. Jagtoyen. Carbon Fiber Composite Molecular Sieves: Synthesis and Characterization, In *Poc. Carbon '94*, Granada, Spain, July 3-8, 1994. Pub. Spanish Carbon Group, July 1994.

3. F. Derbyshire, Y. Q. Fei, M. Jagtoyen, G. Kimber, M. Matheny, and T. Burchell, Carbon Fiber Composite Molecular Sieve for Gas Separation. "*New Horizons for Materials*". *Advances in Science and Technology, 4.* P. Vincenzini (Ed.), pp. 411-417 (1995). Pub. Techna Srl, Faenza, Italy, 1995.

4. G. C. Wei and JM Robbins, Carbon-Bonded Carbon Fiber Insulation for Radioisotope Space Power Systems, *Ceramic Bulletin*, Vol. 64, No. 5, p. 691 (1985).

5. S. Brunauer, P. H. Emmett and E. Teller, *J. Am. Chem. Soc.*, Vol. 60, p. 309 (1938).

6. R. C. Bansal, J-B Donnet and F. Stoeckli, *Active Carbon*, Pub. Marcell Dekker, Inc., New York (1988).

7. T. D. Burchell, J. W. Klett and C. E. Weaver, A Novel Carbon Fiber Based Porous Carbon Monolith, In *Proceedings of Ninth Annual Conference on Fossil Energy Materials*, Oak Ridge, Tennessee, U.S.A., May 1995. ORNL/FMP-95/1, CONF-9505204, pp. 447-456. Pub. Oak Ridge National Lab, U.S.A., August 1995.

8. T. D. Burchell and R. R. Judkins, *Energy Convers. Mgmt* Vol. 37, Nos. 6-8, pp. 947-954, 1996.

9. S. J. Gregg and K. S. W. Sing, *Adsorption, Surface Area and Porosity, 2nd Edition,* Pub. Academic Press, San Diego, CA (1982).

SESSION II

CERAMICS, NEW ALLOYS, AND FUNCTIONAL MATERIALS

OXIDATION-RESISTANT INTERFACE COATINGS FOR SiC/SiC COMPOSITES

D. P. Stinton, E. R. Kupp, J. W. Hurley and R. A. Lowden

Oak Ridge National Laboratory
P. O. Box 2008
Oak Ridge, TN 37831-6063

S. Shanmugham and P. K. Liaw

University of Tennessee
427b Dougherty Engineering
Knoxville, TN 37922

ABSTRACT

The characteristics of the fiber-matrix interfaces in ceramic matrix composites control the mechanical behavior of these composites. Finite element modeling (FEM) was performed to examine the effect of interface coating modulus and coefficient of thermal expansion on composite behavior. Oxide interface coatings (mullite and alumina-titania) produced by a sol-gel method were chosen for study as a result of the FEM results. Amorphous silicon carbide deposited by chemical vapor deposition (CVD) is also being investigated for interface coatings in SiC-matrix composites. Processing routes for depositing coatings of these materials were developed. Composites with these interfaces were produced and tested in flexure both as-processed and after oxidation to examine the suitability of these materials as interface coatings for SiC/SiC composites in fossil energy applications.

INTRODUCTION

Continuous fiber ceramic matrix composites require fiber/matrix interfaces which allow load transfer from the matrix to the fibers when the composite materials are stressed. Crack deflection and fiber pullout are also necessary components of the mechanical behavior of composites. Fiber/matrix interfaces are currently on of the weak links in continuous fiber ceramic matrix composites materials for applications in the oxidative environments which are typical of fossil energy applications. Pyrolytic carbon performs well as an interfacial coating for Nicalon fiber-reinforced silicon carbide-matrix composites, however it's use in fossil energy applications may be limited because of its poor oxidation resistance. If stressed above the point where the matrix cracks, air can penetrate into the composites and oxidize the fiber/matrix interfaces. After very short times the composite's mechanical properties suffer and eventually the material becomes brittle.[1] Alternate interface coatings need to be developed that are chemically stable with respect to the fiber and matrix materials, and thermally stable and oxidation resistant at use temperatures.

Shanmugham et al[2] conducted FEM analysis and reported that a low modulus interfacial coating will be effective in reducing the radial stresses that result on cooling to room temperature from processing temperature. Further, for interfacial materials with the same modulus, a material with

a higher thermal expansion coefficient than that of the fiber and the matrix may be more effective in reducing the radial stresses than a material with a lower thermal expansion coefficient. These FEM results were similar to the analytical modeling results of Hsueh et al[3]. In order to investigate the above hypothesis, mullite and aluminum titanate were chosen as candidate interface materials for further study.

Another approach being investigated is to deposit a modified form of SiC in the interface. This idea was described previously by Lowden et al[4]. In a SiC fiber/SiC matrix composite, such an interface would be chemically and mechanically stable and as thermally stable as the other components of the composite. The modified SiC, amorphous in this case, would have a relatively low modulus to encourage crack propagation at the fiber/matrix interface.

EXPERIMENTAL PROCEDURE

Composite preforms were prepared by stacking discs of ceramic-grade Nicalon™ plain-weave cloth (Nippon Carbon Company, Tokyo, Japan) in a 0/30/60 sequence in graphite holders. After immersing the preforms in acetone to remove the fiber sizing they were ready for interface coating deposition. The oxide interface coatings were deposited by a sol-gel process described previously[5]. Thin CVD carbon films were deposited on most samples on the fibers and/or on the interface coating prior to matrix infiltration. These films were not thick enough to act as effective interface coatings, but their purpose is simply to protect the samples from the corrosive CVD environment. Carbon deposition conditions were:

Temperature: 1100°C
Pressure: ~1-2 kPa
Time: 15 min
Gas flows: 25 cm^3/min C_3H_6
500 cm^3/min Ar.

The amorphous SiC interface coatings were also deposited by CVD, but at varying conditions. Only the pressure was held constant, at atmospheric pressure (101 kPa). The reaction gases in this case were methane (CH_4), methylsilane (CH_3SiH_3) and Ar.

The composites were infiltrated using forced flow chemical vapor infiltration. In this process, described in detail by Stinton et al[6], the gases are forced to flow through the preform under temperature and pressure gradients. When the pressure gradient reaches 200 kPa, the furnace automatically shuts off and the gas flows are stopped. The reactants used are 0.3 cm^3/min methyltrichlorosilane (MTS, CH_3SiCl_3) and 500 cm^3/min hydrogen. The top temperature of the preform holder is maintained at 1200°C and the pressure downstream of the part is 101 kPa.

RESULTS AND DISCUSSION

Sol-Gel Oxide Interface Coatings

Mullite and aluminum titanate precursor sols were developed for coating applications. The high temperature X-ray diffraction (HTXRD) study conducted on the precursor gels revealed that mullite and aluminum titanate formed at 1050°C and 1400°C, respectively. Based on the HTXRD results, it could be concluded that the aluminum titanate formation temperature is too high and would degrade Nicalon fibers. Since mullite forms at 1050°C, it was predicted that a mullite coating could be obtained on Nicalon fibers without damaging the fibers.

The developed mullite and aluminum titanate precursor sols were utilized for coating Nicalon tows and fabrics. Nicalon tows dipcoated in the mullite precursor sol and heat treated at 1000°C for 10 h, and cooled to room temperature broke easily during handling. In contrast, Nicalon tows dipcoated in the aluminum titanate precursor sol and heat treated similarly were relatively easy to handle. It should be noted that only an alumina and titania mixture would form on Nicalon fibers at 1000°C. Since alumina-titania did not damage the Nicalon fibers, it was considered as an interface material for further investigation.

A Nicalon/SiC composite with a mullite interface was fabricated, with the mullite (50 nm thick) interface deposited by a sol-gel process. However, the composite exhibited brittle fracture, and this could be attributed to the degradation of the Nicalon fibers during the sol-gel processing of mullite. In order to avoid damage to the fibers during the sol-gel processing of the oxide, the need to apply a thin carbon coating (inner carbon layer) prior to the deposition of an oxide coating deposition was recognized. Thermodynamic modeling studies indicated that oxide coatings would be attacked by HCl, a by-product of the SiC matrix formation reaction. It was surmised that a thin carbon coating (outer carbon layer) deposited on the oxide coating prior to the SiC matrix infiltration may help prevent the HCl attack. It should be noted that these carbon coatings are too thin to act as effective interfaces on their own.

In order to get a better understanding of the type of interface that would be appropriate to pursue, Nicalon/SiC composites with the following interfaces were considered: An oxide/C interface and a C/oxide/C interface. The composite with an oxide/C interface would identify the degradation of Nicalon fibers, if any, that might occur during the sol-gel processing of the oxide, because the oxide coating is directly applied on the fibers in this case. The composite with a C/oxide/C interface is likely to have better mechanical properties than a composite with a C/oxide interface, since the likelihood of the fiber degradation taking place during the sol-gel processing of the oxide is reduced due to an inner carbon layer.

The flexure strength results of Nicalon/SiC composites with four different interfaces are summarized in Table 1. The standard deviation of the flexure strength measurements for all the cases

was less than 25%. For the first two cases, it should be noted that there was no inner carbon layer, while the last two composites had an inner carbon layer between the fiber and the oxide. Twenty four flexure bars of approximately 2.5 x 3.0 x >33 mm dimensions were cut from each of the composites. The four-point bend testing was conducted either with inner and outer spans of 10 mm and 20 mm, or 10 mm and 30 mm, respectively. Twelve flexure bars of each of the composites were tested in the as-processed condition. For composites with low strength (< 150 MPa) in the as-processed condition, the remaining 12 bars were oxidized at 1000°C for 24 h in air, and subsequently tested at room temperature. In the case of composites with moderate or high strength (> 225 MPa) in the as-fabricated condition, the remaining 12 bars were oxidized at 1000°C in air as follows: 6 bars for 24 h, 3 bars for 200 h, and 3 bars for 500 h.

From Table 1, it is evident that composites with out an inner carbon layer had low flexure strength (< 122 MPa). The composite with a mullite/C interface had low flexure strengths (< 80 MPa) both in the as-processed and oxidized condition, and underwent brittle failure (no damage-tolerance). In contrast, the composite with an Al_2O_3-TiO_2/C interface had an average flexure strength of 122 MPa in the as-processed condition, and did not undergo any significant strength reduction on oxidation. Morevoer, it displayed damage-tolerant behavior in both the cases.

Table 1. Flexure strength results of Nicalon/SiC composites with four different interfaces

ID#	Interface	Strength (MPa)‡				Fracture Type
		As Processed	Oxidized at 1000°C in air 24 h	200 h	500 h	
1	Mullite/C	64	80	-**	-	Brittle
2	AT*/C	122	112	-	-	Composite
3	C/Mullite/C	304	286	221	217	Composite
4	C/AT/C	255	189	TBT***	TBT	Composite

‡ standard deviation < 25 % AT* - Al_2O_3-TiO_2 -** - not tested TBT***- to be tested

The composite with a C/mullite/C interface had a moderate flexure strength of around 304 MPa as-processed condition and did not have any significant strength reduction after 24 h oxidation. However, the strength dropped to 221 MPa after 200 h oxidation and remained at that level even after 500 h oxidation. In contrast to a composite without an inner carbon layer (mullite/C interface), this composite (with an inner carbon layer) had damage-tolerant behavior in the as-processed condition

and sustained this characteristic even after 500 h oxidation. Fig. 1 shows the load vs displacement curve for samples in the as-processed and after 200 h oxidation for a composite with a C/mullite/C interface. It is evident from the figure that even after 200 h oxidation, the sample displayed a non-catastrophic mode of failure.

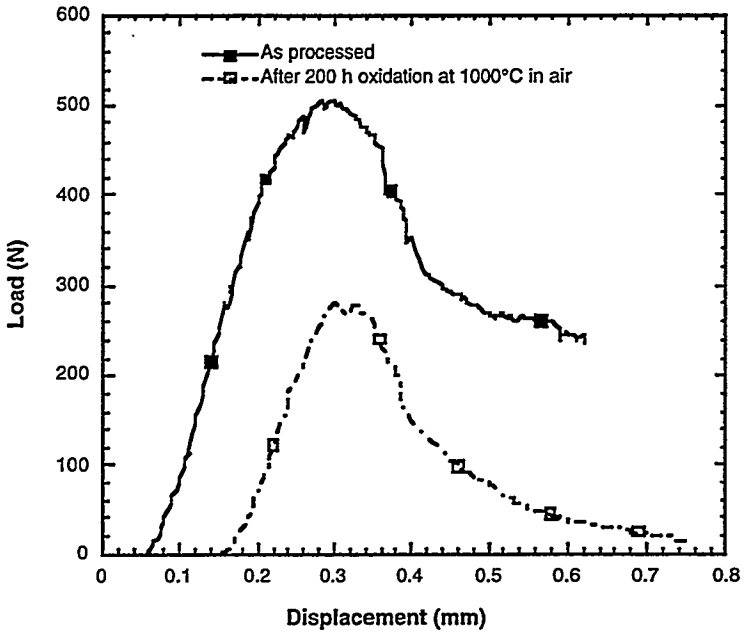

Figure 1. Composite with a Nicalon/C/mullite/C interface exhibit damage-tolerant behavior even after 200 h oxidation at 1000°C in air, but with reduced flexure strength

In the as-fabricated condition, the composite with a C/Al_2O_3-TiO_2/C interface had a higher flexure strength (255 MPa) than the composite with an Al_2O_3-TiO_2/C interface (120 MPa). This situation prevailed even after oxidation for 24 h (200 h and 500 h oxidized samples are to be tested). Similar to the composite with an Al_2O_3-TiO_2/C interface, this composite also exhibited non-catastrophic failure.

Preliminary fracture surface examination revealed that the composite which underwent catastrophic failure showed very little pullout. In contrast, the samples which displayed non-catastrophic failure showed considerable amount of pullout. Scanning auger spectrometer analysis is underway and should identify where the debonding occurred (fiber-coating interface or coating-matrix interface) and the interface coating thickness.

Amorphous SiC Interface Coatings

Previous work with a modified SiC interface coating in SiC/SiC composites yielded promising oxidation-resistance, but the coatings were generally non-uniform within the part. The primary goal of much of the recent work involving this interface material was to optimize the interface deposition uniformity. Other objectives were to repeat promising processing conditions to assess the reproducibility of the process and run longer term oxidation tests to further assess the stability of the materials in high temperature oxidative environments.

A series of experiments was performed in which the amorhpous SiC deposition temperature was varied from 880 to 1000°C. The intent of these runs was to increase the interface coating uniformity by lowering the thermal gradient across the preform. The results of these tests were inconclusive since the flexure strengths were not statistically different in samples coated at different temperatures (see Table 2), although the variability in strengths was generally decreased as the temperature decreased. The load-displacement curves were indicative of materials showing good composite behavior in all cases. Another matrix of experiments was initiated at a deposition temperature of 1000°C in which the total flow of gases as well as the methylsilane and methane concentrations were varied to study their effects on composite uniformity. Increasing the total gas flow and/or concentrations of CH_3SiH_3 and CH_4 appeared to produce composites with less uniform coatings (high standard deviations for strengths and densities). At low flow/low concentration conditions, the composite properties (density, flexure strength and graceful failures) were promising. Strength retention after exposure to air for 24 hours at 1000°C was also good.

Table 2. Density and flexure strength data for composites with amorphous SiC interfaces deposited at temperatures between 880 and 1000°C.

Sample	Deposition Temperature (°C)	Density (g/cc)			Flexure Strength (MPa)		
		Top	Middle	Bottom	Top	Middle	Bottom
CVI947	880	2.63	2.58	2.36	144.2±28.5	334.3±22.1	248.1±35.4
CVI946	925	2.56	2.46	2.25	164.2±71.7	207.9±90.4	221.3±10.3
CVI950	1000	2.60	2.56	1.84	123.1±5.4	229.7±75.8	98.4±4.3

The following set of processing conditions was determined to be optimum after further refinement of the process, combining the best conditions from each set of experiments and additional tests of deposition time:

Temperature - 900°C
Pressure - 101 kPa
Time - 1 hr
Gas flows - 40 cm^3/min CH_3SiH_3
500 cm^3/min CH_4
500 cm^3/min Ar

The optimization was based on the magnitudes and uniformity of density, coating thickness and mechanical behavior (flexure strength and load-displacement curve shape) throughout the parts. Density is a measure of the degree of infiltration, which may be affected by the distribution of the interface coating. Non-uniform distribution may lead to portions of the part sealing before they are fully dense. Flexure testing is used not only as an assessment of the strength and damage tolerance of a material, but also to determine the extent of damage caused by oxidation. The flexure behavior of samples with an amorphous SiC interface coating deposited using the above conditions is illustrated in Figure 2. The composite retained 75% of its strength after being exposed to air at 1000°C for 100 hours. Some of the damage tolerance, or composite-like behavior, was lost during oxidation as evidenced by a faster decline in load-bearing cability past the peak load (i.e. the tail of the curve drops over a smaller displacement). In addition to the optimization of properties at this set of deposition conditions, the composite characteristics were reproducible using these conditions.

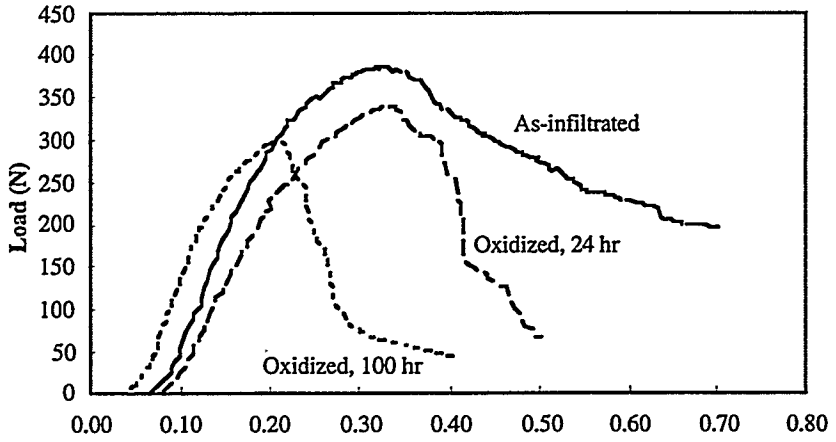

Figure 2. Flexure curves for a SiC/SiC composite (CVI993), with an amorphous SiC interface coating, as-processed and after oxidation for 24 and 100 hours at 1000°C in air.

Additional evidence that the SiC interface coating is effective even after oxidation is seen in Figure 3. This figure contains micrographs of the fracture surfaces of as-infiltrated and oxidized

composite samples. Considerable pullout is apparent in both images, indicating that the interface coating is still acting as the weak point and crack deflection is occuring at the interface.

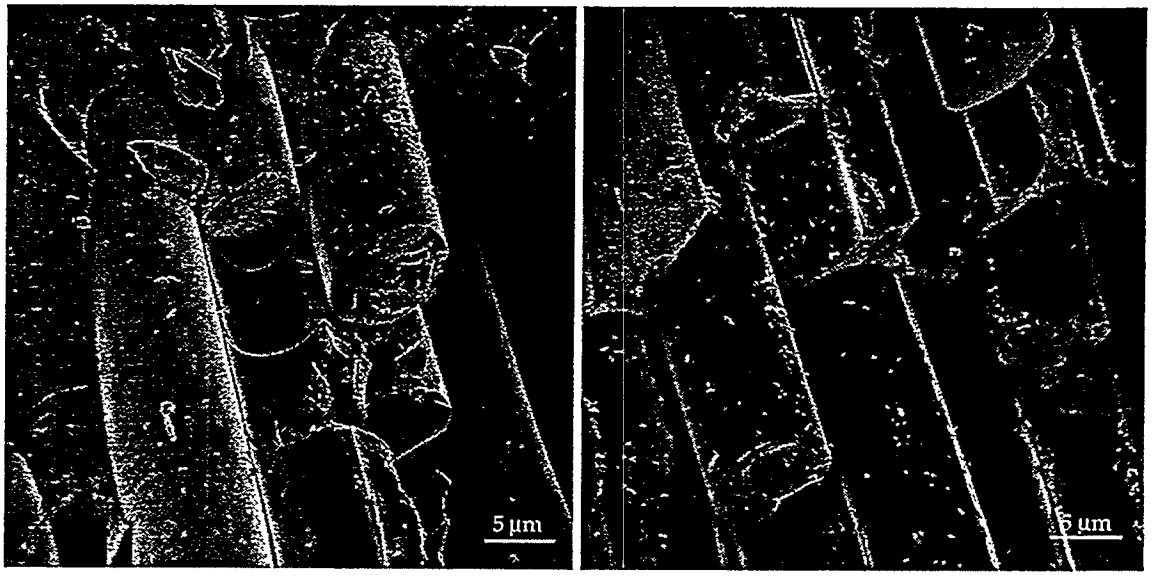

(a) (b)

Figure 3. Scanning electron micrographs of a SiC/SiC composite with an amorphous SiC interface coating showing extensive pullout in both (a) as-infiltrated and (b) oxidized (100 hr, air, 1000°C) states.

CONCLUSIONS

Composites with C/oxide/C interfaces exhibited higher flexure strengths than those of composites with oxide/C interfaces. Among the composites investigated, the composite with a C/mullite/C interface had the highest flexure strength and retained damage tolerant behavior even after 500 h oxidation. Both C/mullite/C and C/Al_2O_3-TiO_2/C interfaces have good potential as interface materials for Nicalon/SiC composites and long-term oxidation tests need to be conducted to ascertain their potential.

Amorphous SiC also shows potential as an oxidation-resistant interface material in SiC/SiC composites. The deposition process has been optimized to yield a composite that is fairly uniform from top to bottom in terms of density and mechanical behavior. Flexure strengths of 350-400 MPa have been achieved. These materials also exhibit graceful failures characteristic of composite behavior even after oxidation, although a portion of the strength and damage tolerance are lost during oxidation.

REFERENCES

1. P. F. Tortorelli, S. Nijhawan, L. Riester and R. A. Lowden, "Influence of Fiber Coatings on the Oxidation of Fiber-Reinforced SiC Composites," Ceram. Eng. Sci. Proc., 14 [7-8], 358-366 (1993).

2. S. Shanmugham, D. P. Stinton, F. Rebillat, A. Bleier, T. M. Besmann, E. Lara-Curzio, and P. K. Liaw, "Oxidation-Resistant Interfacial Coatings for Continuous Fiber Ceramic Composites," Ceram. Eng. Sci. Proc., 16 [4], 389-99 (1995).

3. C. H. Hsueh, P. F. Becher, and P. Angelini, "Effects of Interfacial Films on Thermal Stresses in Whisker-Reinforced Ceramics," J. Am. Ceram. Soc., 71 [11], 929-33 (1988).

4. R. A. Lowden, O. J. Schwarz and D. P. Stinton, "Development of Oxidation-Resistant Interface Coatings," pp. 105-116 in the Proceedings of the Eighth Annual Conference on Fossil Energy Materials, ed. by N. C. Cole and R. R. Judkins, Oak Ridge, TN, May 10-12, 1994.

5. S. Shanmugham, P. K. Liaw, D. P. Stinton, T. M. Besmann, K. L. More, A. Bleier, W. D. Porter and S. T. Misture, "Development of Sol-Gel Derived Coatings for Nicalon™/SiC Composites," to be published in Ceram. Eng. Sci. Proc., 17 (1996).

6. D. P. Stinton, A. J. Caputo and R. A. Lowden, "Synthesis of Fiber-Reinforced SiC Composites by Chemical Vapor Infiltration," Amer. Ceram. Soc. Bull., 65 [2], 347-350 (1986).

ACKNOWLEDGMENTS

"Research sponsored by the U. S. Department of Energy, Office of Fossil Energy, Advanced Research and Technology Development Materials Program and by the U. S. Department of Energy, Assistant Secretary for Energy Efficiency and Renewable Energy, Office of Industrial Technologies, Industrial Energy Efficiency Division and Continuous Fiber Ceramic Composites Program, under contract DE-AC05-96OR22464 with Lockheed Martin Energy Research Corporation"

MODELING OF FIBROUS PREFORMS FOR CVI FABRICATION

D.Y. Chiang and T.L. Starr

School of Materials Science and Engineering
Georgia Institute of Technology
Atlanta, Georgia 30332-0245

The purpose of this program is to alter our existing CVI model to account for configuration changes made to ORNL's tubular forced-flow, thermal gradient CVI. Once these changes are made, the optimal parameters for this configuration are determined to produce high density, gas-tight tubes with short process time. Experimental validation could not be performed due to lack of experimental data because of problems encountered in running the new configuration. Alternative flow patterns show the promise of simpler fixturing and comparable results

INTRODUCTION

Ceramic matrix composites are very promising materials for future fossil fuel generation technology due to their excellent elevated temperature properties such as strength, thermal shock resistance and thermal conductivity. Many of the applications of ceramic matrix composites in this technology are in the form of tubular shaped elements such as heat exchanger tubes or hot-gas filters. Previous attempts at fabricating these tubes using the forced-flow, thermal gradient chemical vapor infiltration (FCVI) technique developed at Oak Ridge National Laboratory (ORNL) discovered many significant problems. The tube furnace and related fixturing has been redesigned and altered to alleviate some of these problems. The purpose of this program is to alter the existing process model to account for the revised configuration and then to use the model to find sets of optimal processing conditions. Also, an alternative processing scheme, the isothermal, alternating flow configuration is explored.

SYSTEM CONFIGURATION FOR FREE-STANDING TUBES

The previous ORNL configuration was modeled and reported in the past. [1] Significant changes were made from this configuration because of problems that surfaced

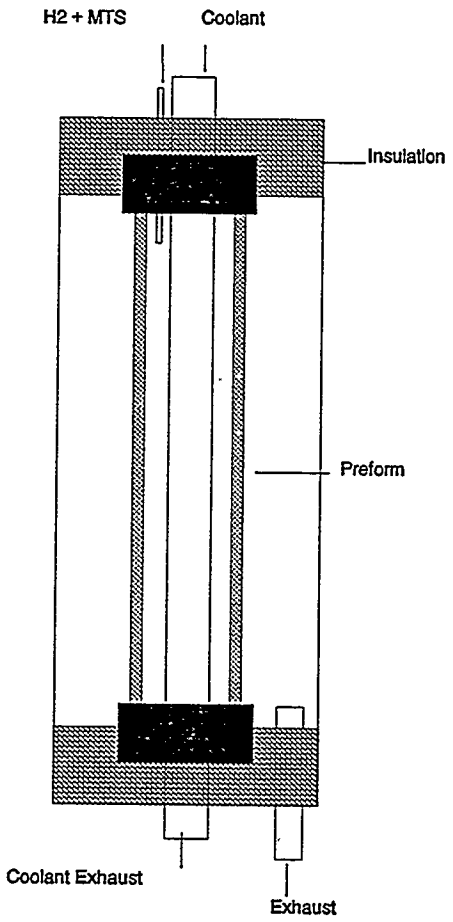

Figure 1: The new ORNL tube CVI configuration utilizes a free standing preform.

during operation. One of the most prominent problems in the original configuration was leakage of the feed gas due to poor fits between the various pieces of graphite fixturing used to hold the preform in place. Also during processing, the tube was cemented to the graphite mandrel used to hold the preform in place. To alleviate these problems, the new configuration shown in Figure 1 is used. This configuration consists of 8 layers of Nextel 312 braided fiber preform that have been rigidized with a phenolic resin to form a free standing preform, eliminating the need for the graphite mandrel. The ends of this preform along with the gas inlet tube and coolant tube are all set into an alumina castable to seal the tube and explicitly define the gas path through the reactor. The inner diameter of the preform is 2 inches with a thickness of 1/4" and a length of approximately 12.6 inches. The control temperature is a

pyrometer that views the outside of the preform. Heating of the reactor is achieved by using small resistively heated graphite rods instead of a large heating element as used previously. The use of the small graphite rods simplified the system by allowing the removal of the reaction chamber that protected the larger heating element from the by-product and waste gases of the reaction.

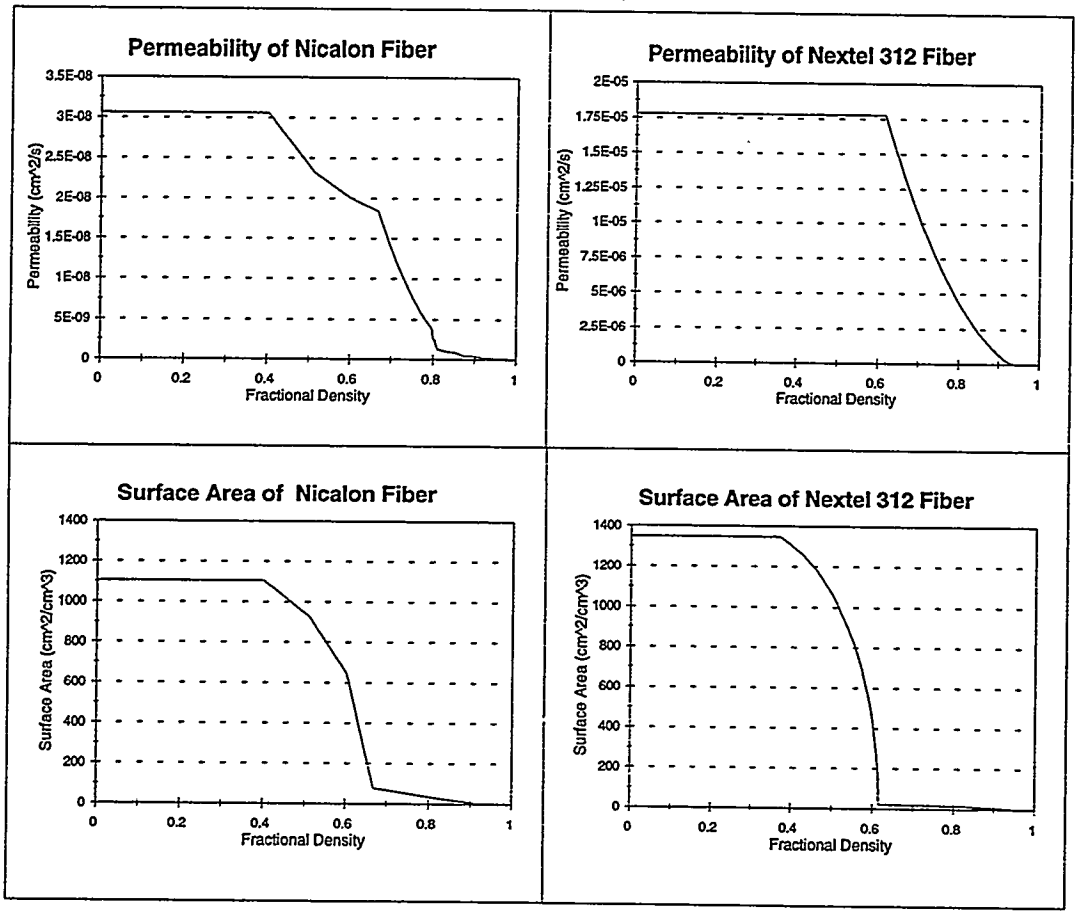

Figure 2: Gas permeability and surface area of Nextel 312 braided preforms are different than those of Nicalon square weave (Note the differences in scale for permeability)

The model used for this optimization process is GTCVI which has been described in previous reports.[2] GTCVI is a first principles based 3-dimensional finite volume process modeling program developed at the Georgia Institute of Technology. A pseudo-steady state model, GTCVI uses the conservation of mass, momentum and energy to solve for temperature, pressure, reactant concentration and densification as functions of time.

To account for the changes in experimental configuration, corresponding changes in the model were performed. First, a model with the corrected dimensions was generated. Then significant changes were made in the preform file to account for the different fiber type and preform construction used. The Nextel 312 fiber has different thermal properties than the Nicalon fibers used in previous experiments. Also, the braided structure of the preform produces different transport properties and surface area curves which are accounted for in the preform file. These differences can be seen in figure 2. Also, due to the change in the location of the control temperature, the model was simplified by moving the boundary condition from the outside of the reactor wall to the outside of the preform. To facilitate initial modeling, only a 1-d slice from the middle of the tube was used. To the extent that the furnace system maintains uniform temperature along the length of the tube, this model is expected to be representative of the whole tube with less computation time.

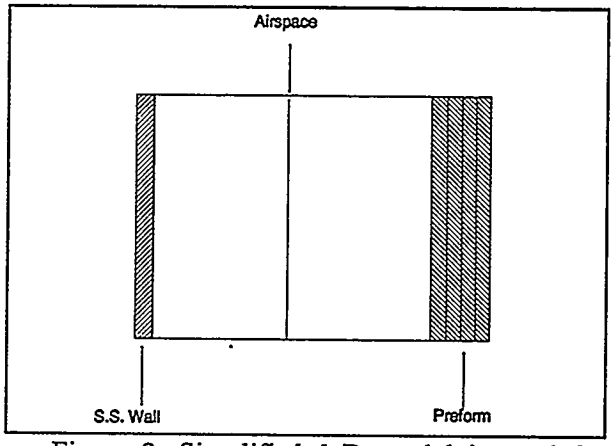

Figure 3: Simplified 1-D model is used for rapid evaluation of a range of process conditions

The model consists of a 1-d, 7 element grid incorporating a stainless steel wall (1 element), airspace (2 elements), and the preform (4 elements) as shown in Figure 3. The inlet gas flows through one end of the reactor at while the exhaust gas flows out the outside diameter of the preform. The controllable variables are the temperatures on the outside of the preform, temperature on the inside of the cooling jacket (stainless steel wall), the total inlet gas flow rate (H2 + MTS) and the MTS concentration in the inlet flow stream.

PROCESS OPTIMIZATION FOR FCVI

In order to establish optimal conditions for FCVI, a measure of merit was established. The variables of importance are considered to be average density, density gradient, total process time and reagent usage. A process that results in high average density, low density gradient, low total process time and high reagent usage is deemed as optimal. The average density was calculated using a weighted mean to account for differences in volumes of each control volume due to the cylindrical shape of the preform. The density gradient is simply the maximum density minus the minimum density. This was determined to be a sufficient representation of the density gradient since all runs in this design matrix have an almost linear density gradient with the hot side as the maximum and the cool side as the minimum densities. The reactant usage was found by dividing the amount of reactant depleted by the amount input to the system at each time step. An average value over the entire run is used. It is not possible to optimize the system for all of these measures of merit simultaneously; there are inherent tradeoffs among the process characteristics. Different applications may warrant different "optimal" process conditions. For example, if a high mechanical strength is required by the application, then a longer process time can be tolerated. On the other hand, if it is possible to use a lower density part in another application, then significant economic advantages can be gained in process time and efficient reagent usage with a different set of process parameters. Because of this, we have optimized the process for three different situations. In case I high mechanical properties are required so high density and good uniformity are the priorities. Case II emphasizes economical processing with sacrifices made in mechanical strength. Case III is a balance of all four with high density, reagent usage and uniformity, and low process time.

To find the optimal conditions, a 2 level, 4 factor full factorial set of experiments were established. The outside temperature ranged from a high of 1200 ^{o}C (the upper limit of fiber stability) to a low of 1000 ^{o}C. It was decided that temperatures below 1000 ^{o}C would not result in sufficiently rapid densification. Inside temperature ranged from 300-50 ^{o}C which corresponds to the use of different cooling media through the center of the reactor such as water, ethylene glycol or air. The total molar flow rate ranged from 1E-6 to 1E-4 (0.8-80 L/min) and the molar concentration of MTS ranged from 5% to 15%. A high concentrations

of MTS may deposit some elemental silicon instead of stoichiometric silicon carbide. The coding and actual values of the different levels used in this matrix of experiments are shown in Table 1. Note that F = total gaseous flow rate in L/min, T(o) = temperature on the outside of the preform in ^{o}C, T(i) = temperature on the inside of the cooling tube in ^{o}C, and C = concentration of MTS in the inlet stream in molar percent.

Table 1: Coded Levels and Actual Values

Variable	-	0	+
T (outside) (^{o}C)	1000	1100	1200
T (inside) (^{o}C)	50	175	150
Flow Rate (moles/cm^2 s)	800	8000	80000
Concentration (molar %)	0.05	0.10	0.15

RESULTS

The results from the factorial set of model runs are shown in Table 2 along with the appropriate variable levels used. According to our modeling results, there are no advantages to running at the lower temperature of 1000 ^{o}C

CASE I: For the highest mechanical strength, the highest density and lowest density gradient through the part are desired. For the range of experimental conditions explored, this results in a high outside temperature and high inside temperature, combined with a low flow rate and low concentration. These conditions result in the highest average density in the test matrix (0.9413%) and the lowest density gradient (0.0092%). The high temperatures allows

Table 2: Modeling Results

T(o) T(i) F C	Time	ρ (avg)	ρ(max)	usage
+ + + +	11.5	0.9155	0.0747	14.7
+ - + +	13	0.9041	0.1020	13.4
+ + - +	38	0.9326	0.0341	40.2
+ - - +	40	0.9316	0.0391	36.5
+ + + -	23	0.9073	0.0909	15.5
+ - + -	25.5	0.9080	0.1008	16.5
+ + - -	83	0.9413	0.0092	54.1
+ - - -	71	0.9219	0.0677	52.5
- + + +	65	0.9246	0.0511	6.5
- - + +	55	0.8887	0.1395	6.0
- + - +	188	0.9363	0.0216	13.6
- - - +	192	0.9240	0.0684	12.8
- + + -	138	0.9312	0.0335	7.8
- - + -	103	0.8913	0.1350	7.1
- + - -	363	0.9310	0.0384	19.0
- - - -	313	0.9287	0.0412	17.9
0 0 0 0	63	0.8983	0.0271	22.8

for a high reaction rate while the low flow rates allows for depletion to balance the temperature gradient through the part resulting in a uniformly densified part. Another advantage of running under these conditions is the low concentration coupled with the high temperature reduces the chance of codeposition of silicon with the SiC matrix. [3] The runtime under these conditions is a fairly long 83 hours.

CASE II: Process optimization from an economic standpoint involves two competing factors. Depending on the relative cost of running a reactor versus reagent costs, the optimal parameters are quite different. If, for example, reagent costs or reagent removal from the waste stream costs are very high, then utilization is the dominant factor in the economic analysis. In this case, conditions should be at high temperatures (inside and out) and low flow rates and concentrations which also gives the most thoroughly densified and uniform part but requires 83 hours to complete. If runtime is more important (factors such as reactor run costs and product throughput), then very aggressive high temperatures, flow rate and concentration can give a 92% dense tube in under 12 hours but results in a low reagent usage rate of 14.7% and a 7X increase in density gradient. Additional runs at even higher flow rates (1E-3 moles/cm^2 s) produce even faster tube seal-off but results in an extremely large density gradient. These higher flow rates can cut the densification time in half (about 5 hours) but the average density drops to 0.8579% and the gradient is a very large 0.2145%.

Case III balances all factors of interest, optimizing with respect to physical properties as well as economic concerns. The best balance between high density and uniformity as well as low runtime and good reagent usage is high temperatures and concentration while keeping a low flow rate. This results in a 0.9326% dense tube in only 38 hours with a 3X higher density gradient than in case I. Usage is also very good at over 40%.

Also of interest is the effect of the internal temperature. In the past, cooling water at approximately 50 ^{o}C has been used to produce the temperature gradient in the part. Other options are using alternative cooling media such as ethylene glycol or air to control the magnitude of the gradient. At the higher preform temperatures (1200 ^{o}C), an increase in internal temperature causes an increase in final average density as well as decreases in process time and density gradient. A change from 50 to 300 ^{o}C in the internal side of the cooling chamber causes the temperature gradient to drop approximately 35 ^{o}C across the preform. The resulting increase in temperature allows for more uniform deposition (decrease in gradient of 0.059%) and higher average densities (increase of 0.019%) at the extremes of flow rate and concentration (high flow and concentration or low flow and concentration). If the hot-side temperature is lowered to 1000 ^{o}C and high flow rates are used , the result is more dramatic allowing a significantly higher average density part (increase up to 0.0399%) and a large decrease in the density gradient (decrease up to 0.1015%). It has been shown that the internal

temperature can be quite significant in densification results and should be explored more thoroughly through experimentation.

ALTERNATING FORCED FLOW CONFIGURATION

In an effort to simplify fixturing and processing of the tubular CVI, an alternative configuration is explored. This configuration is a reversible forced-flow, isothermal process. The idea behind this processing scheme is to isothermal densify the part in one direction which results in a density gradient due to reactant depletion. To compensate for this density gradient, the flow is reversed mid-way through the process. In theory, this should allow for another density gradient in the opposite direction resulting in a uniformly densified part and significant economic savings due to less fixturing and ease of operation.

Table 3: Alternating Forced Flow Results

Process	Time (hrs)	ρ_{avg} (%)	$\rho_{gradient}$ (%)	Usage (%)
Isothermal	24	0.8694	0.1150	55.1
Alternating-isothermal	28	0.9240	0.0366	33.7
Thermal Gradient	38	0.9326	0.0341	40.2

The conditions of case III (high temperatures and concentration, low flow rate) were used. The reactor was set up so that the entire reactor was isothermal at 1200 ^{o}C and both the inlet path and outlet were of the same volume. The inlet and outlet were set at diagonally opposed ends. The same molar flow rate was used through both paths which is the same flow rate used in the thermal gradient process. The process was run in the same direction as the thermal gradient configuration for 13 hours, then the direction of the inlet flow was reversed until completion. As can be seen in Table 3, the alternating flow isothermal process can lead to significant reduction in process time with a small sacrifice in average density and almost no change in the density gradient. Not only does the alternating flow isothermal process reduce

process time, it can significantly decrease cost due to the simplicity of fixturing and the eliminated need for cooling. Because of the ease and cost savings of an isothermal process, the alternating flow scheme has the potential to produce well densified, economic tube shaped CVI parts competitive or even superior to the thermal gradient process.

SUMMARY

Changes were made to the process model to reflect configuration alterations in ORNL tubular forced-flow thermal gradient CVI process. The optimal conditions for different sets of criteria were determined. It was also determined that a change of cooling fluid which would allow a smaller temperature gradient in the preform can result in higher average densities and better uniformity. A alternative processing configuration, the alternating flow, isothermal process, shows promise in producing high density uniform tubes with short process times and simplified fixturing.

REFERENCES

1. Starr, T.L., Chiang, D.Y. "Modeling of Fibrous Preforms for CVI Fabrication" Proceedings of the Ninth Annual Conference on Fossil Energy Materials, May 16-18, 1995.

2. Starr, T.L. and Smith, A.W., "Modeling of Forced Flow/ Thermal Gradient Chemical Vapor Infiltration", Oak Ridge National Laboratory Report /ORNL/sub/85-55901/03 (September 1993).

3. Lowden, R.A., et al. "Effect of Infiltration Conditions on the Properties of SiC/Nicalon Composites", Oak Ridge National Laboratory Report /ORNL/TM-10403 (May 1987).

FIBER/MATRIX INTERFACES FOR SiC/SiC COMPOSITES: MULTILAYER SiC COATINGS

H. Halverson and W. A. Curtin

Departments of Engineering Science & Mechanics and Materials Science & Engineering
Virginia Polytechnic Institute and State University
Blacksburg, VA 24061

ABSTRACT

Tensile tests have been performed on composites of CVI SiC matrix reinforced with 2-d Nicalon fiber cloth, with either pyrolitic carbon or multilayer CVD SiC coatings [Hypertherm High-Temperature Composites Inc., Huntington Beach, CA.] on the fibers. To investigate the role played by the different interfaces, several types of measurements are made on each sample: (i) unload-reload hysteresis loops, and (ii) acoustic emission. The pyrolitic carbon and multilayer SiC coated materials are remarkably similar in overall mechanical responses. These results demonstrate that low-modulus, or compliant, interface coatings are *not* necessary for good composite performance, and that complex, hierarchical coating structures may possible yield enhanced high-temperature performance. Analysis of the unload/reload hysteresis loops also indicates that the usual "proportional limit" stress is actually slightly below the stress at which the 0° load-bearing fibers/matrix interfaces slide and are exposed to atmosphere.

INTRODUCTION

The performance and long-term durability of ceramic matrix composites for use in Fossil Energy applications relies on the stability of specifically designed fiber/matrix interfacial coatings. Carbon coatings provide the necessary interface properties for low temperature applications, but readily oxidize at elevated temperatures and limit overall composite life. There is thus a critical need for the development of new coatings and coating structures to provide high-temperature performance. Here, the results of tensile tests performed on composites of CVI SiC matrix reinforced with 2-d Nicalon fiber cloth, with either pyrolitic carbon or multilayer CVD SiC coatings[1] on the fibers, are described. To investigate the role and properties of the different interfaces, two types of

measurements are made on each sample: (i) unload-reload hysteresis loops are measured at a sequence of applied loads, and (ii) acoustic emission events are detected during loading. A comparison of the pyrolitic carbon (0.4μm) and multilayer SiC coated materials shows the overall mechanical responses to be remarkably similar in detail. The multilayer coatings, which have only very thin intermediary carbon layers, provide the same interfacial debonding and sliding as the standard thicker carbon layers. Careful analysis of the unload/reload hysteresis loops also indicates that the "proportional limit" stress does not correspond to the point at which the 0° load-bearing fibers are exposed to atmosphere, which occurs at a higher stress level. These results also demonstrate that low-modulus, or compliant, interface coatings are not necessary for good composite performance and that complex, hierarchical coating structures may be a direction for development of enhanced high-temperature performance in ceramic composites.

PHYSICAL AND MECHANICAL PROPERTIES

The materials investigated here are SiC/SiC composites fabricated using ceramic grade Nicalon plain weave fiber mats in a matrix of SiC deposited by a Chemical Vapor Infiltration technique. The differences between materials lies in the specific fiber/matrix "coatings" used. One set of samples has fibers coated with 0.4μm of pyrolitic CVD-deposited Carbon, which is the "standard" coating for SiC/SiC composites; these samples will be designated as PyC. A subsequent CVI deposition of the remaining SiC matrix material is performed after the coating deposition. The other set of samples has multilayer coatings consisting of alternating layers of SiC and PyC. The PyC layers are only ≈0.02μm in thickness while the SiC layers begin at 0.125μm at the inner (fiber) radius and increase in thickness by a factor of 1.25 as successive coatings are applied; these samples will be designated as ML. The graded "coatings" extend continuously outward until the material is fully densified; the "matrix" is thus a sequence of concentric annuli of SiC separated by very thin layers of Carbon. The fiber loadings and densities of the two sets of materials are shown in Table I.

The samples described above were supplied as tensile bar specimens of approximately 5 inches in length (aligned with one of the two orthogonal fiber directions), 1/2" inches in width, with a thickness of about 1/8". Fiberglass end tabs were applied with epoxy and strain gauges mounted in the center of an approximately 1" gauge section. The

samples were then subjected to interrupted tensile tests: samples were loaded in tension to peak stresses of 10, 15, 20, 25, and 30 ksi, and then unloaded and reloaded to measure the hysteretic response at each load level. Acoustic emission signals were detected using a standard AE transducer set-up and an attenuator.

The results of the tension tests are partially summarized in Table I. The initial small-strain Young's moduli of the ML materials are smaller than those of the PyC materials, but this is largely attributable to the lower density and higher fiber loading, since the fibers are less stiff then the CVI-SiC matrix. The "proportional limit", or matrix-cracking point, is estimated by using an 0.005% offset stress and is also shown in Table I. The ML materials have a lower offset stress, suggesting a lower matrix cracking threshold; however, we will discuss carefully below the onset of matrix cracking in the 0° fiber tows. The tangent modulus near failure is observed to be larger for the ML materials. Since after matrix cracking the modulus is fiber-dominated, this result is generally consistent with the higher fiber longitudinal loading of the ML materials, although even after normalization by $V_f/2$ the ML materials are stiffer. The additional stiffness could stem from incomplete "matrix cracking" or reduced fiber damage at failure; the former is more likely the reason, as will be seen by other comparisons. The ultimate tensile strengths (UTS) of the two materials are very nearly equal when normalized by $V_f/2$, indicating that the in-situ strengths of the as-processed fibers are essentially comparable. However, the failure strains of the ML materials are generally larger by about 10%, while equal fiber strengths would suggest that the failure strain should be consistent with the failure strength.

Table I. Physical and mechanical property data for SiC/SiC composites with pyrolitic carbon (PyC) and multilayer SiC (ML) fiber coatings, respectively.

	Dens g/cc	Fiber loading V_f	Youngs modulus E_c (Msi)	Final Tan modulus E_t (Msi)	Tensile Strength σ_{uts} (ksi)	$2\sigma_{uts}/V_f$ (ksi)	Failure Strain (%)	.005% Offset Stress
PyC	2.55	0.30	35	3.2	≈30	200.0	≈0.4	15.5
ML	2.45	0.36	30	4.4	≈35	194.4	≈0.45	11.0

Figures 1a,b show the tensile stress-strain curves and hysteresis loops obtained for two specific but representative samples of the ML and PyC materials. These curves

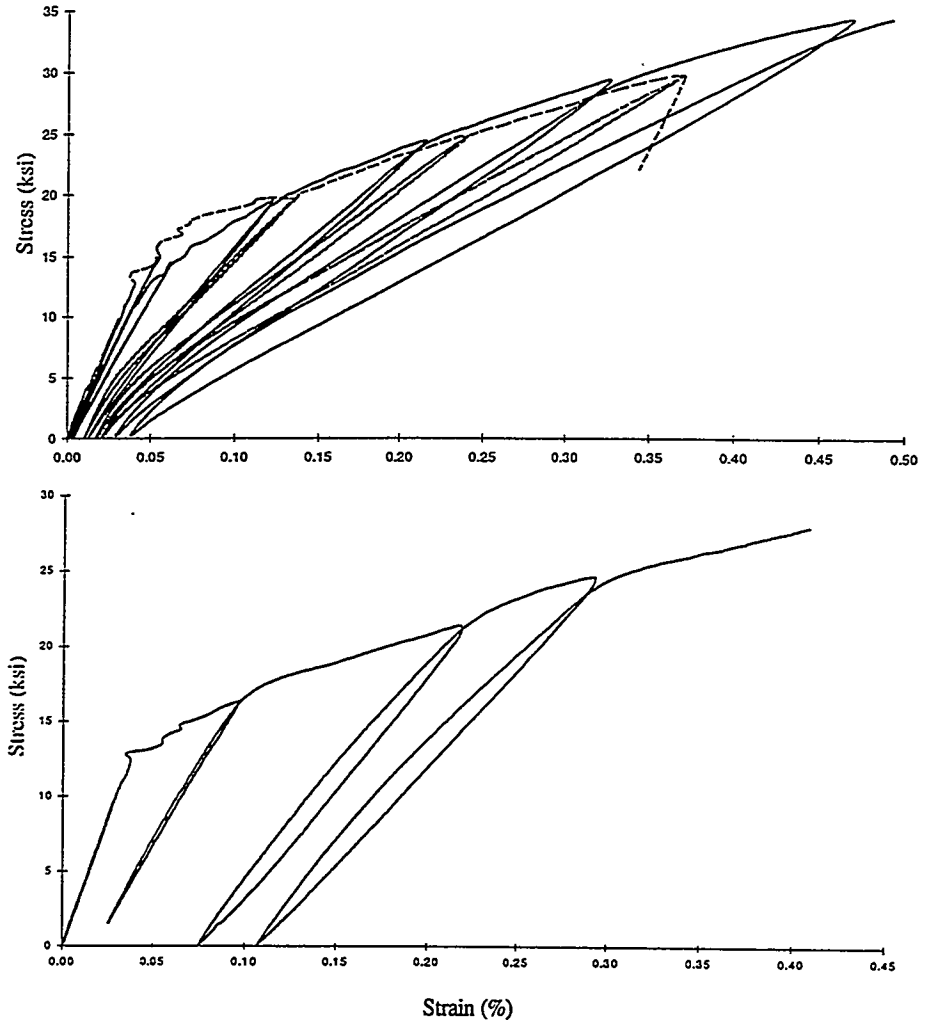

Figure 1. Stress-strain and hysteresis loops for SiC/SiC composites. Solid line - ML; dashed line - PyC Type I; dotted line - PyC Type II.

exhibit some of the general features discussed above and tabulated in Table I. However, they also show other features of interest. In particular, the PyC materials appear to fall into two classes, depending entirely on the hysteretic behavior. In one class (Type I; Figure 1a), the hysteresis loops are fairly narrow and the residual strain on complete unloading is small. In the other class (Type II; Figure 1b), the hysteresis loops are much broader and the residual strain is much larger; this behavior is more similar to that described recently by Lamon and coworkers for SiC/SiC materials.[2] The hysteretic behavior is an indicator of both extent of cracking and (irreversible) interfacial sliding between fibers and coating (or coatings and matrix) and thus highlights qualitative

differences in the interfacial behavior that are not evident from the stress-strain loading curves alone. The ML samples are almost all of the Type I class, with narrow hysteresis loops and small residual strains. The agreement in mechanical response between the PyC Type I materials and the ML materials is quite remarkable, given the rather different interface coatings in the two systems.

MATRIX CRACKING THRESHOLDS

The onset of matrix cracking and "debonding" of the fibers from the matrix or coating is of critical importance in applications of CMCs wherein chemical attack/oxidation of the exposed interfaces can rapidly degrade mechanical properties. The use stress at temperature is thus considered to be below the matrix cracking threshold. Superficially, it would appear that the ML materials are inferior in this regard because the 0.005% offset stress is rather lower than that for the PyC materials. However, what is really of importance is the exposure of the 0° fiber interfaces and not the macroscopic non-linear deformation represented by the offset stress. In fact, early non-linear behavior can be beneficial in toughening or notch resistance of CMCs, as a mechanism of stress redistribution around stress concentrators. Here, we take a more careful look at the mechanical response around the matrix cracking threshold.

The onset of non-linearity can be associated with (i) pure crack formation in the matrix material and not in the fiber tows, or (ii) crack penetration into the fiber tows, followed by debonding at one of the coating interfaces. To assess which mechanism might be operative at a particular stress level, one must examine the hysteretic behavior of the material to look for irreversable response. Matrix cracking alone will lead to increased composite strain and a decreased composite modulus but will not yield either a residual strain (aside from very small relieved thermal residual strains) or hysteretic response associated with irreversable energy dissipation mechanisms such as interfacial sliding. Debonding at the fiber coating and subsequent fiber sliding does lead to both permanent strains and irreversable sliding and hysteresis. In fact, the hysteretic behavior is now regularly used to determine the fiber/matrix interfacial sliding resistance in unidirectional composites.[3]

Figure 2 shows the permanent offset or residual strain as function of applied load for both ML and PyC materials. Figure 3 shows the hysteresis loop area as a function of applied load for both ML and PyC materials. At the lowest stress of 10 ksi, the ML materials exhibit essentially no residual strain although there has been some non-linear deformation. The ML materials also exhibit essentially zero hysteresis, as measured by the loop area, at 10 ksi. Only at 15 ksi and above is there measurable residual strain and hysteresis. In comparison to the PyC materials, the ML materials are nearly identical to the Type I PyC materials at all applied loads, whereas the Type II materials show the rapid increase in residual strain and hysteresis evident in the typical stress-strain curve of Figure 1. The presence of non-linearity in the deformation of the ML materials at 10 ksi is therefore attributed matrix material cracking external to the 0° fiber tows, which would not expose those fibers and the interfaces to potential degrading atmospheres. The enhanced matrix damage at such low stresses probably arises from the multilayer nature of the ML "matrix" material. Additional flaws in the multilayer structure plus the blunting or deflection of matrix cracks at matrix interfaces generated by the ML matrix structure can cause enhanced "microcracking" in the matrix alone at low stresses. Only at elevated stresses do the more tradiational matrix cracks extending into the 0° fiber tows appear, which gives rise to the residual strain and hysteresis behavior.

From the detailed comparison between ML and Type I PyC samples, we conclude that these two materials have nearly identical interfacial sliding characteristics, at least to the extent that such characteristics impact the macroscopic material mechanical response. This conclusion is rather surprising. It is well established that composite behavior in SiC/SiC materials with PyC coatings is not obtained when only thin coatings are utilized; coatings greater than about 0.25μm are necessary to obtain debonding, sliding, and tough behavior. One of the prevailing arguments for the need for a minimum thickness is that the low-modulus PyC coating reduces the thermal and processing clamping stresses between fibers and matrix, which also then reduces the friction stress between fiber and matrix. Composites with high friction and/or debond stresses, as measured by pushout experiments for example, can be particularly brittle. The present results indicate that substantial amounts of PyC are *not* necessary for obtaining good composite behavior. The present ML materials have multiple layers of very thin carbon coatings, but at ever increasing radii, and these coatings in total are insufficient to mimic the effects of one thick PyC coating of 0.4μm. At 60% fiber fraction in the tows and a fiber radius of 7.5μm, 8 layers of increasing SiC coating are needed to densify the tow and the total carbon

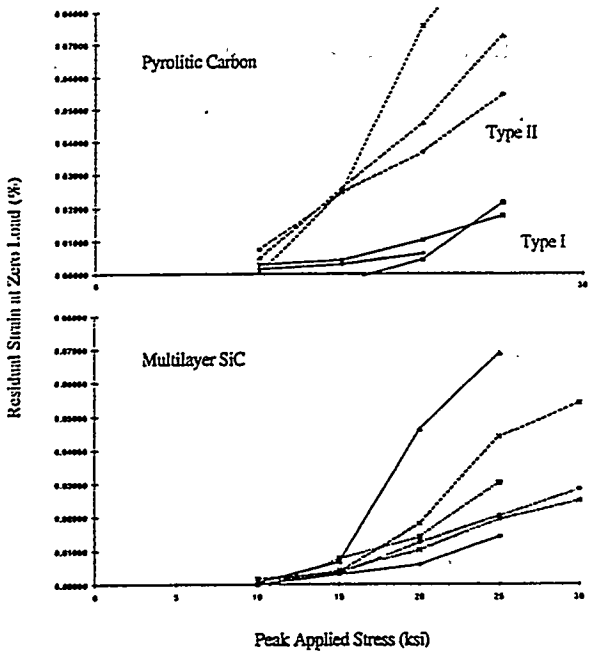

Figure 2. Residual strain at zero load versus peak applied load, for both ML and PyC SiC/SiC composites. Note the absence of residual strain in the ML samples at 10 ksi, and close similarity of ML and PyC Type I data.

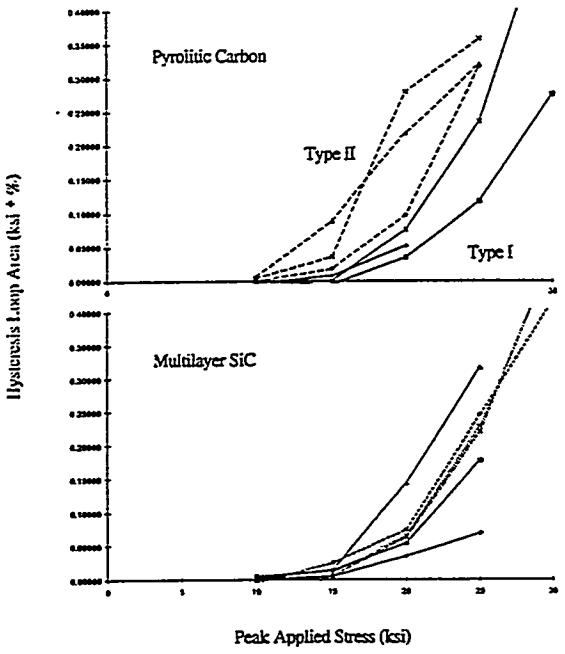

Figure 3. Hysteresis loop area versus peak applied load, for both PyC and ML SiC/SiC composites. Note the complete absence of hysteresis in the ML samples at 10 ksi despite non-linearity in the stress-strain curve prior to this stress.

deposition is then approximately 0.16μm. Hypertherm High-Temperature Composites Inc. has reported similar composite performance results for ML systems with only 2 or 4 SiC layers prior to a full densification infiltration, as well.[4] *The conceptual mechanism of reduced clamping stress from a low-modulus coating may be a sufficient design principle for coating structures but is not necessary for good composite performance. Complex coating structures can accomplish the needed goals of crack debonding and acceptable sliding resistance without low modulus.* These conclusions are consistent with recent multilayer SiC coating developments for the SEP SiC/SiC materials, which have been reported to exhibit composite behavior by Lamon et al. and others.[2]

ACOUSTIC EMISSION

We have monitored the acoustic emission from samples during loading, unloading, and reloading. Results for the number of emission events (hits) versus applied strain are shown in Figure 4 for a PyC Type II and a ML material, along with the associated stress-strain behavior. The ML materials show much greater acoustic activity than the PyC materials, starting at very low loads. The large amount of activity at low loads is consistent with the conceptual picture of extensive microcrack formation in the matrix prior to full matrix crack development. The AE signals are attributable to the matrix cracking, and it is evident that the peak AE coincides quite well with the dominant knee in the stress-strain curves, where considerable matrix cracking is driving the increasing strain in the material. In the ML materials, the peak in AE events occurs in the range of 15-20 ksi and then falls off gradually, but AE events are detected all the way up to failure in nearly all cases. In the PyC samples, the AE peak is at lower stresses, again around the knee in the stress-strain curve, but the AE events then die away rapidly with further loading, indicating a saturation of cracking. The rapid attainment of a nearly linear stress-strain curve in the PyC materials and the more gradual approach to a constant tangent modulus in the ML materials is consistent with the occurrence of broadly distributed matrix cracking in the ML materials. The greater number of events in the ML materials is attributable to the complex matrix/coating structrue which favors the blunting of larger cracks in favor of a multiplicity of smaller cracks in the layered structure. The precise

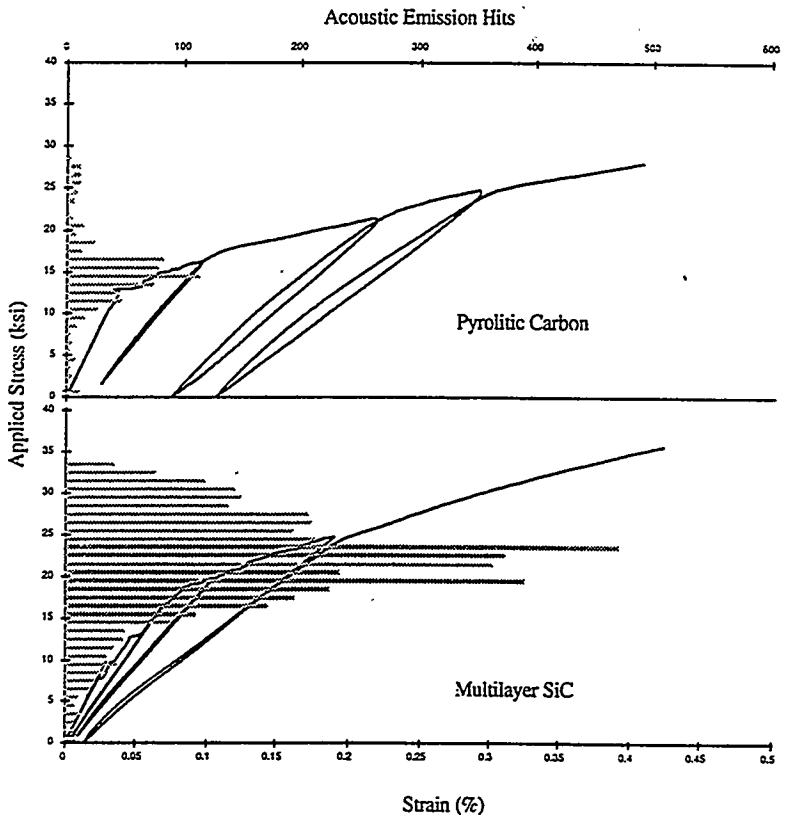

Figure 4. Acoustic emission counts versus strain, with superimposed stress-strain behavior, for typical ML and PyC Type II samples.

nature and number of AE events does not appear to have large effects on the overall deformation history, but is of interest in comparing different materials.

We have attempted to analyze the AE signals in detail to distinguish between matrix cracking and fiber breakage. However, all correlations between signal characteristics such as rise time, amplitude, duration, and energy are the same over the entire loading history. There are no simple signatures in the AE signals which suggest matrix cracking at lower loads giving way to fiber breakage at elevated loads.

Lastly, essentially all of the AE activity occurs on loading of the samples. On unloading and reloading no further AE events are detected until the load is increased beyond the prior peak load. This demonstrates the absence of any pronounced fatigue crack propagation during the measurement of the hysteresis behavior.

SUMMARY

In summary, we have presented experimental data on the mechanical response of SiC/SiC composites with novel multilayer SiC coatings, and compared their response to that of standard composites wtih pyrolitic Carbon coatings. The mechanical response is nearly identical in the two cases, including subtle aspects such as hysteretic unload/reload behavior. The early onset of non-linearity in the ML materials is not attributed to full matrix cracking, with exposure of fiber/matrix interfaces, and hence the use of a simple proportional limit stress for assessing composite use stress is probably conservative. Detailed study of the hysteretic behavior appears to help identify the onset of fiber/matrix sliding behavior. The data on ML materials demonstrates that thick low modulus coatings are not necessary for obtaining composite behavior in SiC/SiC materials, which opens new avenues for the development of potential oxidation-resistant, high temperature coatings.

REFERENCES

1. Generously supplied by Hypertherm High Temperature Composites Inc., Huntington Beach, CA.

2. C. Droillard and J. Lamon, J. American Ceramic Society 79, 849 (1996).

3. E. Vagaggini, J. M. Domergue, and A. G. Evans, "Relationships between Hysteresis Measurements and the Constituent Properties of Ceramic Matrix Composites: I, Theory", J. Am. Cer. Soc. 78, 2709 (1995); J. M. Domergue, E. Vagaggini, and A. G. Evans, "Relationships between Hysteresis Measurements and the Constituent Properties of Ceramic Matrix Composites: II, Experimental Studies on Unidirectional Materials", J. Am. Cer. Soc. 78, 2721 (1995).

4. Private communication, Hypertherm High Temperature Composites Inc.

CONDITIONS FOR TESTING THE CORROSION RATES OF CERAMICS IN COAL GASIFICATION SYSTEMS

John P. Hurley and Jan W. Nowok

Energy & Environmental Research Center
University of North Dakota
PO Box 9018
Grand Forks, ND 58202-9018

ABSTRACT

Coal gasifier operating conditions and gas and ash compositions affect the corrosion rates of ceramics used for construction in three ways: 1) through direct corrosion of the materials, 2) by affecting the concentration and chemical form of the primary corrodents, and 3) by affecting the mass transport rate of the primary corrodents. To perform an accurate corrosion test on a system material, the researcher must include all relevant corrodents and simulate conditions in the gasifier as closely as possible. In this paper, we present suggestions for conditions to be used in such corrosion tests. Two main types of corrosion conditions are discussed: those existing in hot-gas cleanup systems where vapor and dry ash may contribute to corrosion and those experienced by high-temperature heat exchangers and refractories where the main corrodent will be coal ash slag.

Only the fluidized-bed gasification systems such as the Sierra Pacific Power Company Piñon Pine Power Project system are proposing the use of ceramic filters for particulate cleanup. The gasifier is an air-blown 102-MWe unit employing a Westinghouse™ ceramic particle filter system operating at as high as 1100°F at 300 psia. Expected gas compositions in the filter will be approximately 25% CO, 15% H_2, 5% CO_2, 5% H_2O, and 50% N_2. Vapor-phase sodium chloride concentrations are expected to be 10 to 100 times the levels in combustion systems at similar temperatures, but in general the concentrations of the minor primary and secondary corrodents are not well understood. In the case of high-temperature slag corrosion of heat exchangers or refractories that will occur in entrained-flow gasifiers or advanced power systems such as the Combustion 2000 High-Performance Power System, slag corrosiveness will depend on its composition as well as viscosity. For a laboratory test, the slag must be in a thermodynamically stable form before the beginning of the corrosion test to assure that no inappropriate reactions are allowed to occur. Ideally, the slag would be flowing, and the appropriate atmosphere must be used to assure realistic slag viscosity. However, as is the case for the hot-gas cleanup systems, the influence of specific gas stream components on slag properties is poorly understood at this time.

INTRODUCTION

Many advanced power systems will combine two energy cycles to reach efficiencies as high as 47% in converting the chemical energy in coal into electrical energy. The energy cycles always include a typical steam or Rankine cycle, which usually produces 60%–80% of the electric power. The second cycle usually involves one of three possibilities. In an oxidizing system such as a pressurized fluidized-bed combustor (PFBC), one possibility is to clean the hot gas, then directly expand it in a gas turbine. In another concept, the turbine is indirectly fired by using a very high-temperature heat exchanger to transfer the energy to a clean noncondensing working fluid, such as air, which is then expanded in the turbine. The third possibility is to gasify the coal, clean the coal gas, then fire the gas directly into a gas turbine. A steam cycle combined with a gasification cycle is commonly called an integrated coal gasification combined cycle (IGCC).

Ceramics are suggested for constructing structures in these advanced energy systems because of their resistance to corrosion and high-temperature strength. At the highest temperatures, up 1650°C, refractories are used to protect structural components and reduce heat loss from the system. Dense structural ceramics are proposed for use in heat exchangers, which may be used at temperatures as high as 1425°C. Both monolithic and composite ceramics are used to construct hot-gas filters to remove ash from the gas stream at temperatures up to 900°C. To improve the acceptability of these ceramic subsystems, a better understanding of their long-term performance is required.

The University of North Dakota Energy & Environmental Research Center (EERC) is providing technical assistance and test materials to the U.S. Department of Energy Advanced Research and Technology Development (AR&TD) Materials Program investigating ceramic corrosion in fossil energy systems. During 1994–1995, suggestions and materials for testing the corrosion resistance of ceramics in combustion systems were developed and proposed.[1] This year, the focus is on gasification systems. The main activities for are to perform thermochemical equilibrium calculations to develop recommendations for appropriate test conditions and to gather materials such as gasifier slag and ash that can be used by other researchers in performing ceramic corrosion tests.

This paper describes gas, ash, and operational factors that affect the corrosion rates of structural ceramics in coal gasification systems and provides suggestions for appropriate laboratory test conditions. Particular attention is focused on two subsystems: hot-gas particulate filtration and high-temperature refractories and heat exchangers, especially those constructed of silicon- and alumina-based ceramics.

The objective is not to present specific data on rate factors, but to help experimentalists measuring these factors to better design their corrosion tests.

BACKGROUND

Approximately a dozen inorganic elements in the products of coal combustion affect the corrosion rates of silicon-based ceramics used to construct subsystems. These elements, including H, O, Na, Mg, Al, Si, P, S, Cl, K, Ca, and Fe, affect corrosion rates in three ways: as primary corrodents forming reaction products with the material, as secondary corrodents affecting the activity of the primary corrodents, or by influencing the rate of mass transfer of the primary corrodents. Although many of the elements function as more than one type of corrodent, they are listed here under what is believed to be their most active role.

The primary corrodents of silicon-based ceramics in coal-fired combustion systems include O, Mg, Ca, and Fe (refs. 2–6). These elements form silicates or silicides that are stable in the presence of the other constituents of the ash in contact with the ceramic surface. When ash is not present, such as downstream of a filter, vapor-phase Na can also be a primary corrodent of silicate ceramics, forming a sodium-enriched reaction layer through which oxygen can more rapidly diffuse than through a pure silica layer.[7] When ash is present, the more stable form of sodium is as a sodium aluminosilicate in the ash, rather than sodium silicate scale on the silicon carbide.

In contrast to the primary corrodents, the secondary corrodents have not been observed to form corrosion products with silica- or alumina-based ceramics. They are known, however, to affect the activities of some of the primary corrodents. The main elements acting in this role are H, Al, S, and Cl. Hydrogen is most important in gasification conditions, because it affects the concentration of O; in combustion conditions, it helps to form volatile hydroxides such as $Si(OH)_4$ or NaOH, which will affect corrosion rates when no other ash is present. Similarly, S and Cl affect the vapor-phase concentrations of Na_2SO_4 and NaCl, which will affect corrosion rates when ash is not present. In addition, Al affects the activity of Na, Mg, and Ca. Since these elements are more stable in an aluminosilicate phase than in a silicate corrosion product, they are less corrosive to silicate ceramics when aluminum is present in the ash.

The major role of several other elements is their effect on the transport rate of the primary corrodents. These elements include Na, Si, P, and K. Most important are their effects on the viscosity of a melt and on the rate of ion diffusion in a glass. These elements have not been observed to form

corrosion products with silicon- or alumina-based ceramics in coal fueled energy systems, except in minor roles.

Because the concentrations of many of these elements affect the activities of the primary corrodents, the surest experimental design to determine all of the interdependencies is the full factorial matrix, where the concentration of each element in the system is varied dependently on the others. However, the number of tests in such a matrix would involve x^n tests, where x is the number of variations possible for each element, and n is the number of different elements. For three variations (low, medium, and high concentrations) of each of 12 elements, the number of tests is 531,441 for a single temperature and pressure condition. The numbers can be partially reduced by using a fractional factorial test matrix, but the most cost-effective way to perform corrosion tests is to base them on realistic system conditions.

The best way to obtain appropriate test conditions is to expose the material in an operating coal-fueled system. This can be expensive, since a 100-hour pilot-scale test may cost $100,000. As the scale of the test is reduced, so are the costs, but the accuracy of the conditions may also be compromised. To improve the accuracy of laboratory-scale test conditions and allow similar tests performed in different labs to be more comparable, the EERC has been surveying the literature and holding discussions with interested researchers and industry representatives to develop appropriate baseline test conditions. In addition, ash and slag samples are being collected from operating systems and are available in quart or gallon quantities to materials researchers by contacting the lead author. Thermochemical equilibrium calculations are also being performed to determine approximate gas-phase concentrations of some of the elements. The conditions suggested for testing are harsh yet realistic (i.e., not accelerated) and should include all of the primary and secondary corrodents. The ceramic subsystems that are the focus of the research are hot-gas particulate filters and high-temperature heat exchangers/refractories under both combustion and gasification conditions. Conditions for testing under combustion conditions are presented in an earlier paper, so only gasification conditions will be described here.[1]

Gasification conditions are much more difficult to simulate in the laboratory than combustion conditions because of the wide range of gas temperatures and compositions possible in the various systems and because the gas is poisonous and explosive. During gasification, coal is heated in the presence of insufficient oxygen to completely burn. Carbon monoxide and hydrogen are among the major product gases. Variations in system pressure and temperature strongly affect the concentrations of the gases in the product. Also, to keep the calorific value of the gas as high as possible, some gasifiers operate with pure oxygen rather than air, so that the gas is not diluted with nitrogen. This is especially true in the first IGCC systems because at the time of their design, low-Btu gas burners were

not reliable. However, advances in burner design over the last decade will permit air-blown product gas to be burned efficiently in future IGCC systems. These will include the Sierra Pacific Piñon Pine Power Project and the Foster Wheeler carbonizer to be used in the Four Rivers Energy Modernization Project and in the Combustion 2000 High-Performance Power System (HiPPS).

Three main types of coal gasifiers are currently in use: entrained-flow systems such as the pressurized Shell, Texaco, and Dow gasifiers and the atmospheric Koppers–Totzek gasifier; fluidized-bed systems such as the Winkler or Kellogg-Rust-Westinghouse™ (KRW) gasifiers; and a fixed-bed system used by Lurgi. The range of measured operating temperatures and product gas compositions for these three types of gasifiers as reported by Watkinson and others are summarized in Table 1. The coals used range in rank from lignite to bituminous, and all systems shown are oxygen-blown.[8]

TABLE 1

Typical Operating Conditions for the Main Types of Oxygen-Blown Gasifiers

	Entrained Flow		Fluidized Bed		Fixed Bed		Fixed Bed (dry ash)	
	Avg.	Range	Avg.	Range	Avg.	Range	Avg.	Range
Temp, °F		2150–2500		1700–1890		2280–2880		1440–1510
Pressure, psia		15–610		15–370		310–360		390–450
Gas Composition								
CO	54	41–62	37	26–51	57	56–58	17	16–18
H_2	32	30–35	39	32–45	28	27–28	39	39–40
CO_2	6.4	2–10	19	10–39	3.8	3.3–4.3	31	30–32
CH_4	0.1	0–0.3	3.0	1.8–5.0	6.6	6.5–6.7	10	9–11
N_2	1.9	0.8–4.7	0.7	0.5–0.9	2.4	0.6–4.3	1.2	0.8–1.5
H_2S	1.1	0.3–1.8	1.4[a]		1.3	0.6–2.0	1.4[a]	
COS	0.1[a]		0.0[b]		0.0[b]		0.0[b]	
H_2O	4.4[c]		0.0[b]		0.0[b]		0.0[b]	
No. of Systems		4		5		2		2

[a] 1 in estimate. [b] No data, values estimated. [c] Calculated by difference because of lack of data.

The wide range of gasifier designs and operating conditions makes it difficult to choose one set of conditions for baseline testing of ceramic materials. As in combustion, two main subsystems should be addressed: hot-gas particle filters where corrosion is caused by dry ash and gas and heat exchangers/ refractories where the corrosion is caused by molten slag.

HOT-GAS FILTERS

In most of the new oxygen-blown gasifier systems such as the Tampa Electric (Texaco), Wabash River (Dow), and Buggenum, Netherlands (Shell), projects, particulate cleanup will be performed in relatively cool gas at around 500°F, so ceramic corrosion should not be a problem. The Tampa project will include some hot-gas particulate cleanup at 1000°F, but they are proposing to use metal filters. Therefore, our recommendation is to run ceramic particle filter gasification corrosion studies in conditions that will be experienced in the Sierra Pacific Power Company Piñon Pine Power Project fluidized-bed gasifier. The gasifier is an air-blown 102-MW_e unit employing a Westinghouse ceramic particle filter system operating at as high as 1100°F at 300 psia. Bed temperatures are expected to reach a maximum of 1850°F. Expected gas compositions in the filter will be approximately 25% CO, 15% H_2, 5% CO_2, 5% H_2O, and 50% N_2. Vapor-phase sodium chloride concentrations are expected to be 10 to 100 times the levels in combustion systems at similar temperatures, but in general the concentrations of the minor primary and secondary corrodents have not been measured. In addition, a hot-gas cleanup system to remove sulfur will be situated upstream of the filter system, and its effects on the minor species in the gas stream is not well understood.

In order to calculate approximate vapor concentrations of possible corrodents, the FACT program (Facility for the Analysis of Chemical Thermodynamics) developed by C.W. Bale, A.D. Pelton, and W.T. Thomson from Ecole Polytechnique de Montréal, was employed. It permits the calculations of stable phases in an ash–gas system over a broad range of temperatures through the minimization of free energy for the system. The FACT code is simple to implement because only chemical formulas of possible products and the mole fractions of the elements are needed. A multiple linear-regression technique estimates what stable phases are formed by minimizing errors for individual phases.

In simulating Piñon Pine gas compositions, we used a system pressure of 20 atmospheres and the design coal for the system (Utah SUFCo bituminous). The chlorine concentration in the coal is not known, so it was assumed for these calculations to be 100 ppmw, a relatively high figure. Table 2 shows the partial pressures of some corrodents in the gas stream. Concentrations are shown for two temperatures, 1110°F, the approximate maximum operating temperature of the filter vessel, and 1340°F, a temperature between that of the vessel and that of the fluid bed. Since the effects of the hot-gas cleanup system (sulfur removal) on the concentrations of minor corrodents is not known, they were not included in these calculations. Therefore, the data in Table 2 are a better simulation of conditions when the sulfur removal system is not on-line.

TABLE 2

Calculated Partial Pressures of Minor Corrodent Gas Species in the Piñon Pine System

Minor Species	1110°F	1340°F
H_2S	2200×10^{-6} atm	3600×10^{-6} atm
COS	280×10^{-6} atm	260×10^{-6} atm
HCl	76×10^{-6} atm	300×10^{-6} atm
NaCl	2.6×10^{-6} atm	72×10^{-6} atm
$(NaCl)_2$	1.5×10^{-6} atm	34×10^{-6} atm
NaOH	0.00012×10^{-6} atm	0.018×10^{-6} atm

At 1110°F, the partial pressures of sodium species are quite low. However, at 1340°F, a temperature between that of the filter vessel and the fluid bed, concentrations are approximately 25 times higher, indicating that the sodium species may rapidly condense as the gas cools on the way to the hot-gas filter. Since equilibrium may not be reached by the time the gas reaches the filter vessel, the concentration of sodium vapor species in the filter vessel may be much above the equilibrium concentration. Therefore, we suggest that gaseous corrosion tests under hot-gas filtration conditions be run with a gas stream saturated with NaCl vapor by providing an excess of sodium chloride to the system. We suggest that this be done by adding a mixture of HCl and NaCl to water that is dripped into the hot corrosion test reactor. The mixture should be added at a rate to give HCl and NaCl vapors at somewhat higher concentrations than those at equilibrium in the filter vessel. We suggest the concentrations at 1340°F (1000 K) should be used. We acknowledge that this is a somewhat arbitrary value, but believe that these values will provide a harsh, yet realistic concentration of corrodents, which will serve as a benchmark for further parametric tests. Since the correct partial pressures of major gas species cannot be obtained in a 1-atmosphere reactor, we suggest that they be added in concentrations equal to their concentrations in the full-scale system. The suggested total gas stream concentrations for these tests should be 25% CO, 15% H_2, 5% CO_2, 5% H_2O, 300 ppm HCl, and 75 ppm NaCl, with a balance of nitrogen. We suggest that the benchmark tests be run at 1100°F, with other, lower temperatures added in parametric tests.

In addition to vapor species, the ash may also corrode system components. The ash used for corrosion tests should be approximately at equilibrium at the start of the tests to prevent any unrealistic corrosion reactions from occurring as the ash attempts to reach equilibrium test conditions. Unfortunately, the Piñon Pine system is not expected to operate under standard conditions to supply ash to corrosion researchers until sometime in 1997. Therefore, the EERC is making available to corrosion researchers ash collected from the filter vessel of the EERC pilot-scale transport reactor development

unit (TRDU) from a test run performed in April 1996. The system is designed to operate under conditions similar to those at Piñon Pine, although a coal from the Belle Ayr Mine, Powder River Basin, Wyoming, was used for the tests rather than the Utah coal that is the design coal for the Piñon Pine system. The Belle Ayr ash has the advantage for corrosion tests in that it is well characterized, is available as a standard ash free of charge, and the coal will also be used at the Southern Company Services Wilsonville hot-gas filter test facility, which will also be operating fully by 1997.

MOLTEN SLAG CORROSION

At the high operating temperatures to which some heat exchangers and refractories will be exposed, the ash will be very sticky, if not molten, and therefore will coat the subsystems and prevent direct gaseous corrosion of the materials. However, the composition of the gas in the corrosion reactor will still play an important role in the test, since the atmosphere directly affects the viscosity and therefore the erosiveness and corrosiveness of the slag. Figure 1 shows the viscosity versus temperature curves of a slag prepared from ash made by burning coal in the laboratory. The coal is from the Rochelle mine of the Wyoming Powder River Basin and is considered to have a relatively high calcium content. The three curves show the changes in viscosity caused by changes in the surrounding atmosphere. The fundamental reasons for the changes in viscosity are not completely clear, but are believed to be caused by the breakup of O–Si bonds and the creation of nonbridging hydroxyl groups, which will lower viscosity (reducing gas), but may also act as a mineralizer and increase the temperature at which crystallization occurs (air+water). These effects are especially strong for the more basic coal slags because water vapor is usually more soluble in more basic silicate glasses, even dissolving in a molecular form.[9] We suggest an overall gas composition of approximately 30% H_2, 45% CO, and 25% CO_2 to which 10% water vapor is added. Because of equilibrium reactions at this temperature, we have calculated that the concentrations of CO may reach as high as 49%, H_2O as high as 18%, CO_2 as low as 13%, and H_2 as low as 20% at 1400°C. SO_2 and H_2S may cause changes in melt structure similar to those caused by water vapor, but because they are present in much lower concentrations, the sulfur-containing gases are expected to have a lesser effect, although this assumption must still be tested.

In addition to use of the correct atmosphere in slag corrosion tests, the slag should be in a relatively stable thermodynamic form at the beginning of the test. This can be best assured by producing the slag under realistic operating conditions or by collecting the slag from a large-scale operating facility.

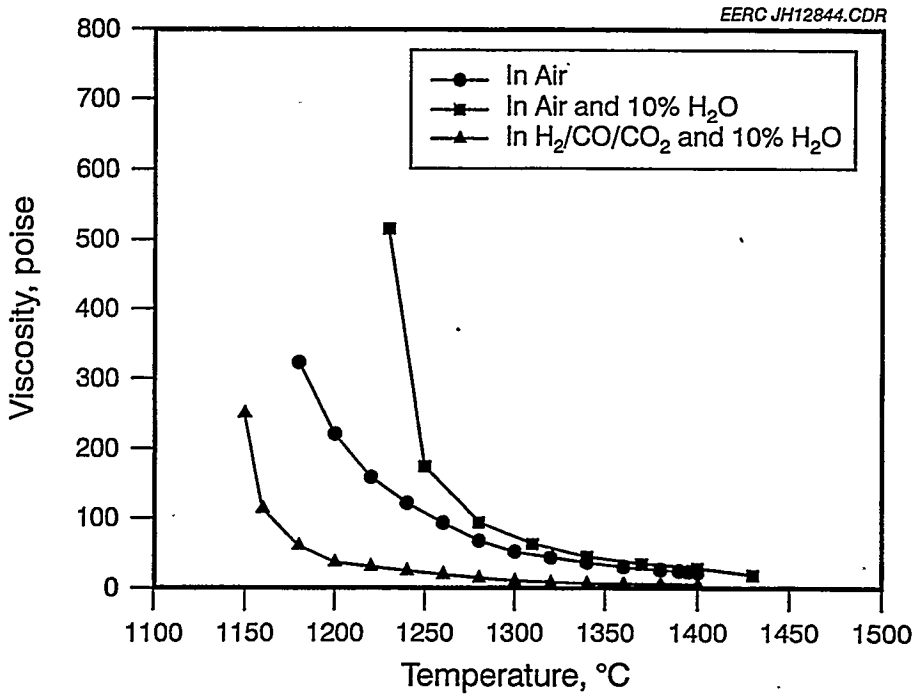

Figure 1. Viscosity versus temperature for Rochelle Mine coal ash slag under 3 atmospheres.

Unfortunately, most gasifier manufacturers and operators are very secretive about their operations, so it can be very difficult to obtain gasifier slag. However, the EERC has available coal slag donated for corrosion testing by three power plants burning economically important coals. The slags are produced in boilers fired with cyclone burners and are therefore in a mildly reduced state. High-calcium subbituminous coal slag was provided by the Northern States Power Company Riverside Plant, which was burning a coal from the Powder River Basin in Wyoming. Illinois No. 6 bituminous coal slag was provided by the Central Illinois Public Service Coffeen Plant. Analysis of the Coffeen slag showed abnormally high calcium concentrations owing to limestone additions to reduce slag viscosity, so another drum of more "pure" Illinois No. 6 slag was obtained from the Illinois Power Company Baldwin Plant. The compositions of the slags as well as the TRDU ash that can be used for corrosion tests at lower temperatures are shown in Table 3. Suggested temperatures for high-temperature slag corrosion testing are 2000°F for sintered ash conditions, 2300°F for viscous molten ash, and 2600°F for running ash. The slag layer thickness should be approximately 1 millimeter at 2600°F and 5 millimeters at 2300°F to ensure appropriate gas transport through the slag. The slag should be replenished often enough that it does not become overly concentrated with corrosion products.

TABLE 3

Chemical Compositions of Standard Ashes

Oxide, wt%	TRDU Ash	Riverside Slag	Coffeen Slag	Baldwin Slag
SiO_2	52.7	47.0	52.5	53.4
Al_2O_3	21.7	18.6	16.3	18.6
Fe_2O_3	1.5	5.3	13.5	17.6
TiO_2	0.8	1.4	0.7	0.7
P_2O_5	0.8	0.6	0.2	0
CaO	13.4	19.7	13.1	7.1
MgO	7.2	5.7	1.2	0.9
Na_2O	0.8	0.9	0.8	0.0
K_2O	0.0	0.3	1.6	1.7
SO_3	1.1	0.3	0.1	0.0

SUMMARY

For a given temperature, the rate of corrosion of ceramic materials in advanced coal-fired energy systems is affected by the composition of the gas and condensed species in contact with the material. Approximately 12 elements affect the corrosion rates of silicon- and alumina-based ceramics in coal-fueled systems: O, Mg, Ca, Fe, and Na (when no ash is present) are primary corrodents in that they have been observed to form corrosion products with silicon carbides. Secondary corrodents—H, Al, S, and Cl—have not been observed to form corrosion products but do affect the activity of the primary corrodents. The other major elements, including Na, Si, P, and K, affect the rate of transport of the primary corrodents by affecting slag viscosity and ion mobility. In general, very little work has been done under reducing conditions, so the primary and secondary corrodents in gasifier systems are not well understood at this time.

To improve the accuracy of laboratory-scale combustion test conditions and assure comparability between testing groups, the EERC has assembled 55-gallon drums of coal ash and slag from large-scale coal-fueled systems that are approximately in equilibrium for mildly reducing conditions. For hot-gas filter testing, ash from the EERC TRDU hot-gas filter is available. The suggested total gas stream concentrations suggested for these tests should be 25% CO, 15% H_2, 5% CO_2, 5% H_2O, 300 ppm HCl, and 75 ppm NaCl, with a balance of nitrogen. We suggest that the benchmark tests be run at 1100°F, with other, lower temperatures added in parametric tests.

To simulate the type of ash that will strike a high-temperature heat exchanger in a combustion system upstream of ash removal devices, slags produced under slightly reducing conditions are available from utility cyclone-fired boilers. Suggested initial conditions for slag testing are 2000°F for sintered

ash conditions, 2300°F for viscous molten ash, and 2600°F for runny molten ash. We suggest an overall gas composition of approximately 30% H_2, 45% CO, and 25% CO_2 to which 10% water vapor is added. To assure appropriate gas transport, the slag layer thickness in a static test should be approximately 1 millimeter for runny slag and 5 millimeters for viscous slags. The slag should be changed often enough to prevent it from becoming overly concentrated in corrosion products, since in a commercial system the slag will be constantly replenished.

REFERENCES

1. J.P. Hurley, "Support Services for Ceramic Fiber–Ceramic Matrix Composites," ORNL/Sub/94-SS112/01, 1995.

2. M.K. Ferber and V.J. Tennery, "Behavior of Tubular Ceramic Heat Exchanger Materials in Acidic Coal Ash from Coal–Oil Mixture Combustion," *Ceram. Bull.*, *62* (2), pp. 236–243, 1983.

3. M.K. Ferber, V.J. Tennery, "Behavior of Tubular Ceramic Heat Exchanger Materials in Basic Coal Ash from Coal–Oil Mixture Combustion," *Ceram. Bull.*, *63* (7), pp. 898–904, 1984.

4. T.M. Strobel, J.P. Hurley, C.L. Senior, J.E. Holowczak, "Coal Slag Corrosion of Silicon Carbide-Based Ceramics in a Combustion Environment," *In* Proceedings of the Symposium on Silicon Carbide-Based Structural Ceramics; American Ceramic Society PAC RIM Meeting, Honolulu, HI, Nov. 7–10; pp. 327–334, 1993.

5. T.M. Strobel, J.P. Hurley, K. Breder, J.E. Holowczak, "Coal Slag Corrosion and Strength Degradation of Silicon Carbide–Alumina Composites," *In* Ceramics Engineering & Science Proceedings, *15* (4), pp. 579–586, 1994.

6. C.L. Senior, G.A. Moniz, J.P. Hurley, T.M. Strobel, "Corrosion of Silicon Carbides by Ash and Vapor in a Coal Combustion Environment," *In* Proceedings of the Symposium on Silicon Carbide-Based Structural Ceramics; American Ceramic Society PAC RIM Meeting, Honolulu, HI, Nov. 7–10, pp. 335–342, 1993.

7 .Z. Zheng, R.E. Tressler, K.E. Spear, "A Comparison of the Oxidation of Sodium Implanted CVD Si_3N_4 with the Oxidation of Sodium-Implanted SiC Crystals," *Corrosion Science*, 33 (4), pp. 569–580, 1992.

8. A.P. Watkinson, J.P. Lucas, C.J. Lim, "A Prediction of Performance of Commercial Coal Gasifiers," *Fuel*, 70, pp. 519–527, 1991.

9. J.E. Shelby, *Handbook of Gas Diffusion in Solids and Melts*, p. 223, 1996.

FRACTURE BEHAVIOR OF ADVANCED CERAMIC HOT-GAS FILTERS

J. P. Singh, S. Majumdar, M. Sutaria, and W. Bielke

Energy Technology Division
Argonne National Laboratory
Argonne, Illinois 60439

ABSTRACT

We have evaluated the microstructural/mechanical, and thermal shock/fatigue behavior and have conducted stress analyses of hot-gas candle filters made by various manufacturers. These filters include both monolithic and composite ceramics. Mechanical-property measurement of the composite filters included diametral compression testing with O-ring specimens and burst testing of short filter segments using rubber plug. In general, strength values obtained by burst testing were lower than those obtained by O-ring compression testing.

During single-cycle thermal-shock tests, the composite filters showed little or no strength degradation when quenched from temperatures between 900 and 1000°C. At higher quenching temperatures, slow strength degradation was observed. The monolithic SiC filters showed no strength degradation when quenched from temperatures of up to ≈700-900°C, but displayed decreased strength at a relatively sharp rate when quenched from higher temperatures. On the other hand, a recrystallized monolithic SiC filter showed higher initial strength and retained this strength to higher quenching temperatures than did regular SiC filters. This may be related to the difference in strength of grain boundary phases in the two cases. In thermal cycles between room temperature and 800-1000°C, both monolithic and composite filters show a small strength degradation up to three cycles, beyond which the strength remained unchanged.

Results of rubber-plug burst testing on composite filters were analyzed to determine the anisotropic elastic constants of the composite in the hoop direction. When these results are combined with the axial elastic constants determined from axial tensile tests, the composite can be analyzed for stress due to mechanical (e.g., internal pressure) or thermal loading (thermal shock during pulse cleaning). The stresses can be compared with the strength of the composite to predict filter performance.

INTRODUCTION

Hot-dirty gas exiting from a gasifier or an advanced combustor contains sufficient particulates to make the gas undesirable for direct utilization in gas turbines and heat engines. Today's hot-dirty gas cleanup systems, such as cyclones, can remove only the fraction

containing the larger particulates. Smaller particulates can be removed only by cooling and filtering the gas. The resulting enthalpy loss causes a significant decrease in overall system efficiency. Thus, there is a critical need for cleaning hot-dirty gas with little or no cooling.

This project supports the development of candle ceramic/composite filters for cleanup of hot-dirty gases. Effort has been directed toward developing materials qualification technology needed to ensure satisfactory performance of filters in hot-dirty gas streams. To predict the long-term performance of such filters, it is important to understand and evaluate fracture behavior of these filters in service environments. Mechanical properties should be evaluated to establish baseline data. Thermal-shock resistance should be measured to predict filter performance in the service environment.[1] Failure modes must be identified and failure mechanisms must be established.

SPECIMENS FOR FRACTURE STUDY

The filters examined in this study were obtained from 3M (Nextel/SiC composite filters), DuPont Lanxide (PRD-66 filters), Babcock & Wilcox (oxide composites), Industrial Filter and Pump Mfg. Co. (IFPM) (regular monolithic SiC with high alumina binder and binderless recrystallized SiC filters) and Pall Corp. (monolithic SiC). The 3M filters consist of layered composite structures; a tubular filter element is sandwiched between two Nextel/SiC composite tubes. Bonding between the Nextel/SiC composite tubes and the filter layer is achieved by the chemical vapor infiltration (CVI) of SiC. The inner and outer diameters of these filters are ≈5.08 and ≈5.72 cm, respectively. Filters were obtained in both as-fabricated and exposed (in the Tidd demonstration plant for ≈1100 h) conditions. The PRD-66 is an all-oxide ceramic consisting of layered microstructure of alumina, mullite, cordierite, and amorphous material; the inner and outer diameters are ≈4.52 and ≈5.96 cm, respectively. The Babcock & Wilcox filter is made by a sol-gel technique and consists of an oxide composite with chopped and continuous Nextel fibers. The inner and outer diameters of the filters are ≈5.00 and ≈5.96 cm, respectively. Both of the monolithic SiC filters consist primarily of SiC grains; inner and outer diameters of the filters are ≈4.52 and ≈5.96 cm, respectively.

EVALUATION OF STRENGTH AND THERMAL-SHOCK AND FATIGUE RESISTANCE

Filter strength was evaluated by both diametral compression testing of O-ring specimens and by burst testing of short filter segments with rubber plugs.

O-Ring Compression Testing

One-inch-wide O-ring specimens were machined from each of the filters and then loaded to failure in a diametral compression mode at a crosshead speed of 0.13 cm/min. Maximum stress develops at the inner diameter across the load points, which simulates the thermal-shock stresses developed during a pulse-cleaning cycle. The fracture stress σ_f is given by Eq. 1.[2]

$$\sigma_f = \frac{PK}{\pi bl}, \tag{1}$$

where P is the fracture load, K is a function of the ratio of inner and outer diameters,[2] b is the outer radius of the specimen, and l is the length of the tube. Load displacement plots for the filter specimens in as-fabricated condition indicated a nonbrittle failure mode for all composites and brittle failure for the monolithic filters. A limited number of O-ring specimens machined from one of the composite filters exposed in the Tidd demonstration plant for ≈1100 h were tested in compression mode; strength was 7.72 ± 1.13 MPa. The corresponding strength of the unexposed filter was 19.47 ± 2.11 MPa. This represents a strength loss of 60% during filter exposure, which correlates very well with the strength loss of the reinforcing fibers and may be related to in-situ fiber damage during filter exposure.[3]

Burst Testing

Burst testing was performed on 1-in.-wide O-ring specimens machined from a Nextel/SiC composite filter in as-fabricated condition. As shown in Fig. 1, uniform radial loading was applied to the O-rings through a rubber plug (slightly smaller in diameter than O-ring) that was compressed between two aluminum plates. Figure 2 shows a typical load-displacement plot for a specimen in as-fabricated condition.

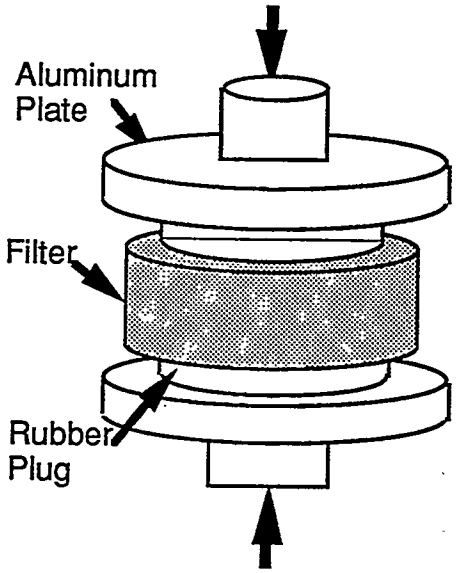

Fig. 1. Schematic diagram of burst test.

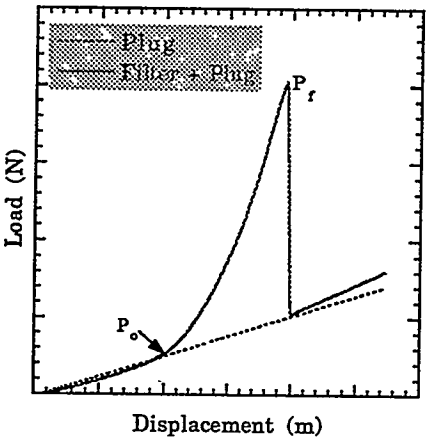

Fig. 2. Typical load-displacement plot for Nextel/SiC filter specimen.

The maximum hoop stress (σ_t) occurs at the inner wall and is given by Eqs. 2 and 3:[4,5]

$$\sigma_t = p^L\left(\frac{r_o^2 + r_i^2}{r_o^2 - r_i^2}\right) \tag{2}$$

$$p^L = \frac{\nu}{(1-\nu)}\frac{(P_f - P_o)}{\pi r_i^2} \tag{3}$$

where p^L is is the radial pressure on the inner wall of the filter; r_o and r_i are the outer and inner radii of the filter, respectively; P_f is the maximum applied load at fracture, P_o is the load at which the rubber plug makes radial contact with the filter; and ν is the Poisson's ratio (value taken to be 0.5). The fracture load P_f and contact load P_o were obtained from the load-displacement plot. To date, a limited number of specimens have been evaluated by burst testing to compare the strength data with those obtained by O-ring compression testing. For the Nextel/SiC composite filter specimens, burst strength was 6.4 ± 0.22 MPa, a lower value than that obtained by O-ring tests. This difference is believed to be due to the larger specimen volume subjected to high stresses during burst testing than that in O-ring compression testing.

Thermal-Shock Testing

Thermal-shock testing was performed on 1-in.-wide ring specimens machined from the filters. The ring specimens were insulated on the outer surface to simulate the heat transfer conditions in service. These specimens were heated to preselected temperatures (25-1100°C) in an electric furnace. Subsequently, the specimens were quenched in silicone oil at room temperature (≈25°C). Thermal-shock damage was estimated by measuring the strength of ring specimens by O-ring compression testing before and after thermal quenching.

The results of the thermal-shock experiments are given in Fig. 3, which shows the retained strength of specimens subjected to varying degrees of thermal quench (ΔT). Vertical bars represent the standard deviation when three or four specimens were tested. Other data points represent values for single specimens.

Results obtained so far indicate that the composite filters show little or no strength degradation when quenched from ≈900-1000°C. At higher quenching temperatures, slow strength degradation was observed. The regular monolithic SiC filters showed no strength degradation when quenched from ≈700-900°C. At higher temperatures, strength decreased at a relatively sharp rate. On the other hand, as seen in Fig. 3b, the recrystallized monolithic SiC filter specimens showed higher initial strength that was retained to higher quenching temperatures than in the regular SiC filter specimens. This may be related to differences in strengths of grain boundary phases in the two cases.

Evaluation of Thermal-Fatigue Behavior

Thermal-fatigue testing of both monolithic and composite filters was performed on 1-in.-wide ring specimens machined from the filters. These specimens were thermally cycled between room temperature and preselected elevated temperatures of 800-1000°C. The elevated temperatures were close to the critical quenching temperature observed in the single-cycle thermal quenching experiments. The ring specimens were insulated on their outer surfaces, as before, to simulate heat transfer conditions in service. Thermal-fatigue damage was estimated by measuring strength (in O-ring compression tests) of the specimens before and after thermal cycling.

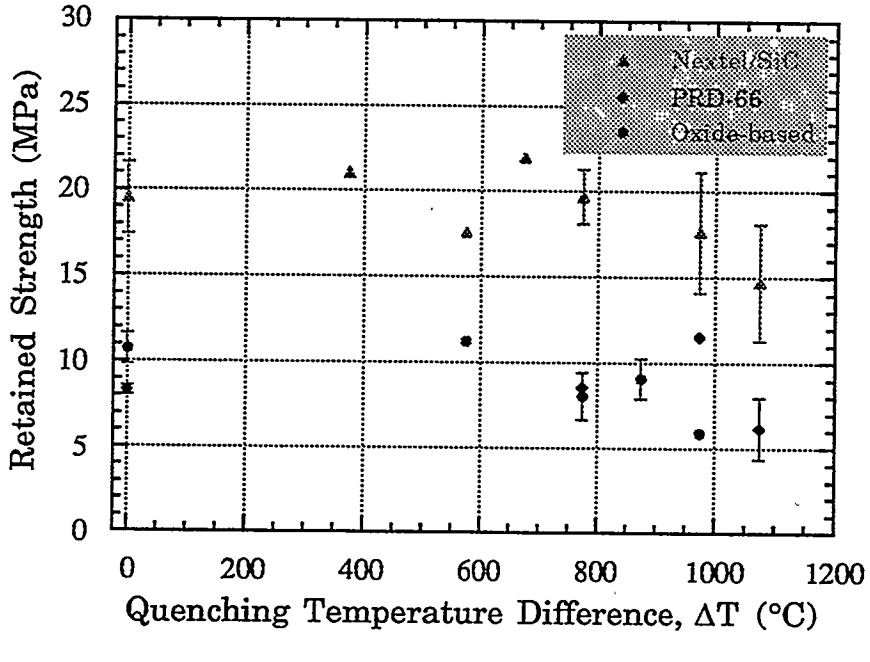

(a)

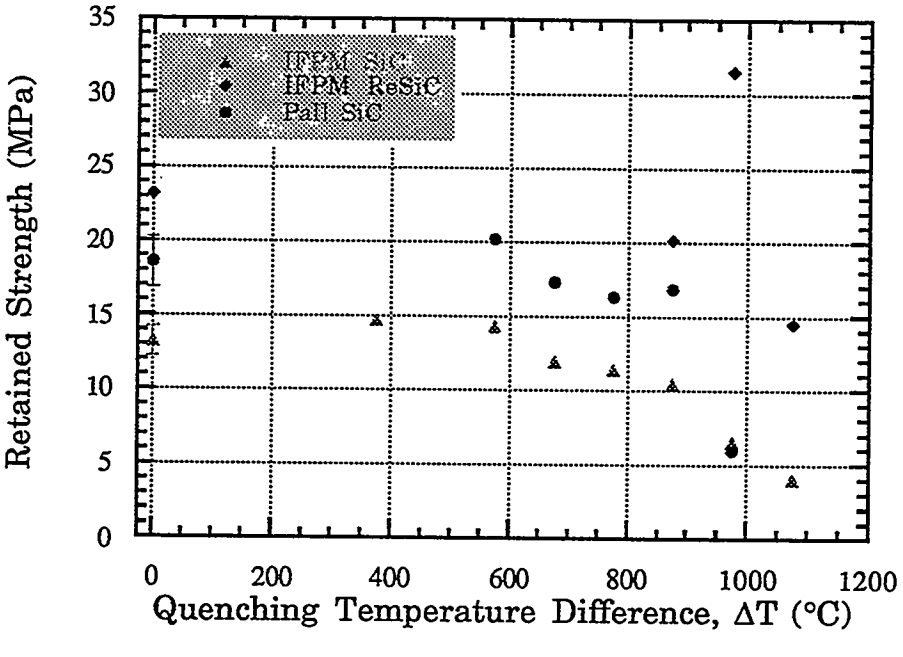

(b)

Fig. 3. Dependence of retained strength of ring specimens on quenching temperature difference (ΔT): (a) 3M Nextel/SiC, DuPont Lanxide PRD-66, and Babcock & Wilcox oxide-based composite filters; (b) IFPM monolithic SiC, IFPM monolithic recrystallized SiC, and Pall monolithic SiC filters.

The results of the thermal-fatigue experiments are given in Fig. 4, which shows retained strength of filter specimens as a function of thermal cycles. Vertical bars represent the standard deviation when three or four specimens were tested. Other data points represent values for single specimens.

In thermal cycling between room temperature and 800-1000°C, Nextel/SiC, PRD-66, and Babcock & Wilcox composite filters show a small strength degradation (18-24%) up to three cycles, beyond which strength remained unchanged. Similar behavior was observed for the monolithic filters that were thermally cycled between room temperature and 800°C; initially, strength decreased by 15-28% up to about three cycles, beyond which the strength remained constant. On the other hand, in thermal cycling between room temperature and 900°C, a large drop in strength was observed for the Pall monolithic filter; the reason for this behavior is currently under investigation to determine if the drop is just a scatter in data. Only one specimen was tested per condition because of limited filter. As expected, both the monolithic and the composite filters showed a slight decrease in strength when thermally cycled at higher temperatures. Microstructural evaluations are in progress to evaluate the failure modes and mechanisms; the results will be used for analytical modeling to predict filter performance in service.

STRESS ANALYSIS OF O-RING BURST TESTS

Recently, a series of burst tests were conducted on the composite filters by using an internal plug. This section summarizes an analysis of the results conducted in order to deduce the elastic stiffness properties of the composite materials.

Geometry

The geometry and loading of the composite O-ring burst tests are shown in Fig. 5. Radial pressure loading is achieved by an internal rubber plug that has an initial radial clearance at the inner diameter (ID) of the composite. The rubber plug is loaded axially in an Instron machine. Initially, the O-ring does not see any load, but after the radial gap between the O-ring and the composite is closed by lateral expansion of the plug (due to Poisson's ratio effect), the composite experiences a radial pressure loading.

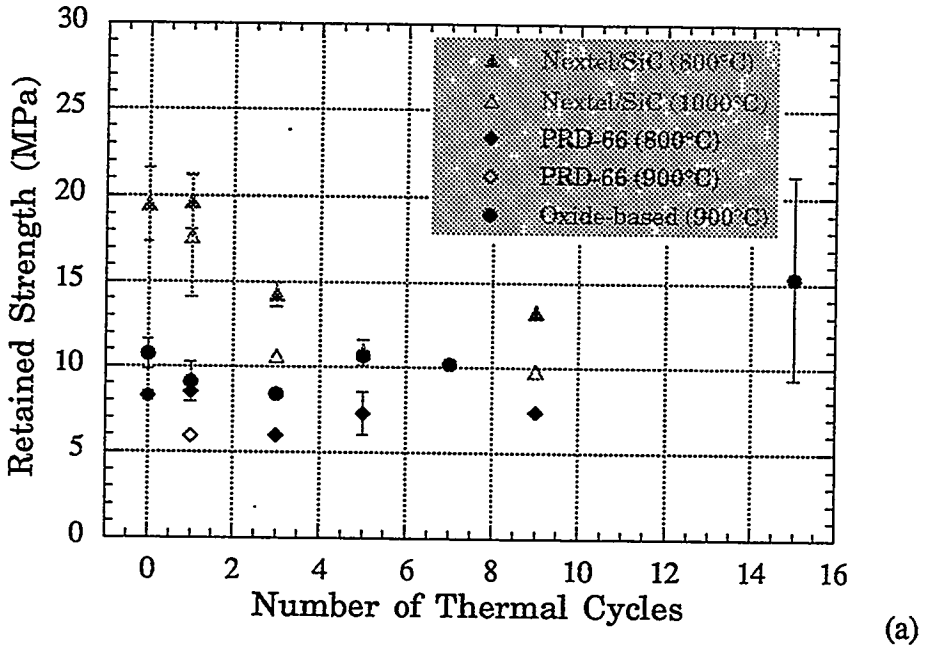

(a)

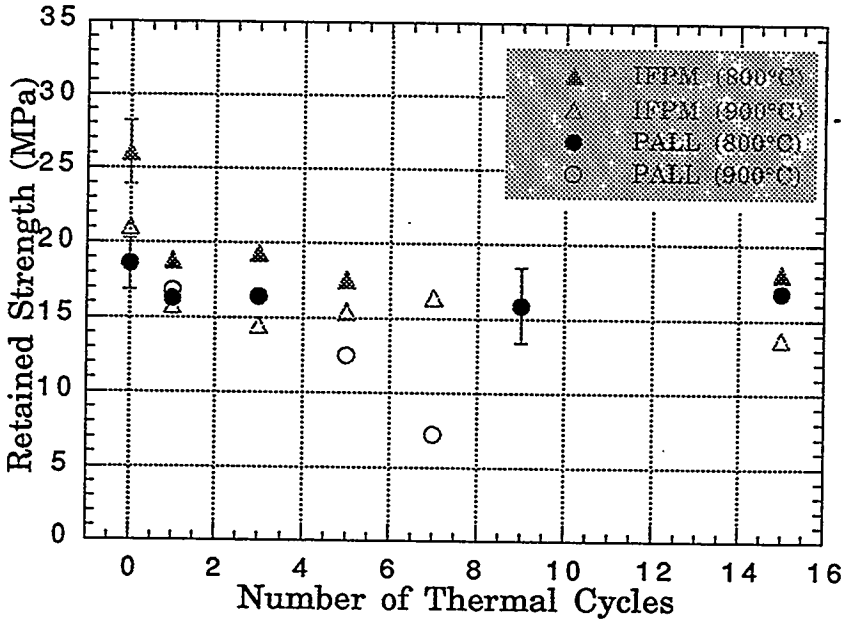

(b)

Fig. 4. Dependence of retained strength on number of thermal cycles: (a) 3M Nextel/SiC, DuPont Lanxide PRD-66, and Babcock & Wilcox oxide-based composite filters; (b) IFPM monolithic SiC and Pall monolithic SiC filters.

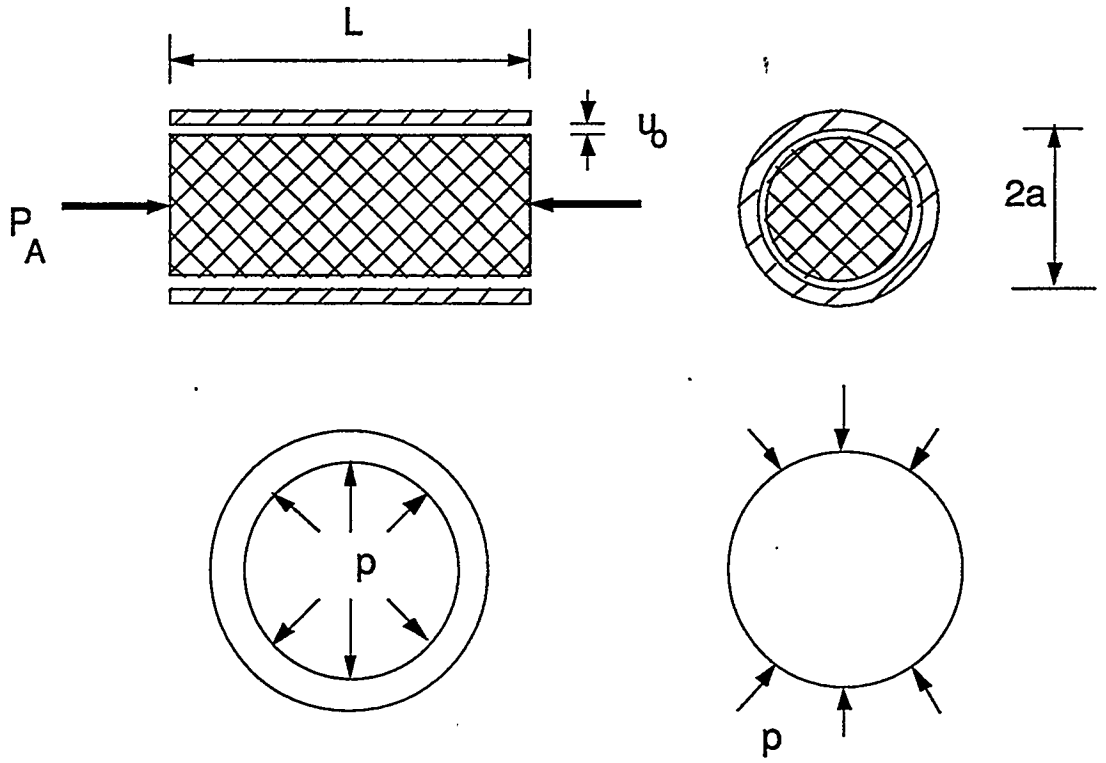

Fig. 5. Typical setup for O-ring burst test. Interfacial pressure p = 0 until radial clearance u_o is closed at axial pressure $p_{Ao} = P_{Ao}/\pi a^2$.

Analysis

The in-plane stress resultants in the composite are related to the membrane strains by the stiffness coefficients K_x, K_y, and K_{xy} as follows:

$$N_x = K_x \varepsilon_x + K_{xy}\varepsilon_y \tag{4a}$$

$$N_y = K_{xy}\varepsilon_x + K_y\varepsilon_y , \tag{4b}$$

where N and ε are the stress resultants and strains, respectively; and subscripts x and y denote the axial and circumferential directions, respectively. We assume that the friction effects at the interface between the rubber plug and the composite O-ring are negligible, so that after contact, the composite experiences hoop stress only, i.e., $N_x = 0$. In such a case, the above stress-strain relationship reduces to:

$$N_y = E_y \varepsilon_y = \left(K_y - \frac{K_{xy}^2}{K_x} \right) \varepsilon \ . \tag{4c}$$

The radial clearance u_o between the plug and the O-ring is closed at an axial pressure of p_{Ao}, where

$$p_{Ao} = E\varepsilon_{Ao} = \frac{E\varepsilon_o}{\nu}, \tag{5}$$

where $\varepsilon_o = u_o/a$, and E and ν are the Young's modulus and Poisson's ratio of the plug, respectively. Assuming the rubber plug to be incompressible ($\nu = 0.5$), the interfacial pressure p beyond the initial contact at an axial pressure p_A is derived by:

$$p = \frac{p_A - p_{Ao}}{1 + \frac{2Ea}{E_y}} = \left(1 - \frac{E}{E_1} \right) (p_A - p_{Ao}), \tag{6}$$

where

$$E_1 = \frac{p_A - p_{Ao}}{\varepsilon_A - \varepsilon_{Ao}} = E\left(1 + \frac{E_y}{2Ea} \right). \tag{7}$$

In Eqs. 6 and 7, E and E_1 are the slopes of the axial stress-strain curve of the rubber plug before and after contact with the O-ring, respectively (Fig. 6).

An estimate for the stiffness of the O-ring can be obtained by solving Eq. 7 as

$$E_y = 2a(E_1 - E). \tag{8}$$

Therefore, the hoop stress resultant corresponding to any axial pressure p_A is given by

$$N_y = pa = \frac{E_y}{2E_1}(p_A - p_{Ao}) = \left[1 - \frac{E}{E_1} \right] (p_A - p_{Ao})a. \tag{9}$$

O-Ring Burst Test

In an ideal O-ring burst test (Fig. 6) starting at O, the plug contacts the O-ring at a stress p_{Ao} and strain ε_{Ao} (point A), after which the load-displacement curve follows the steep curve

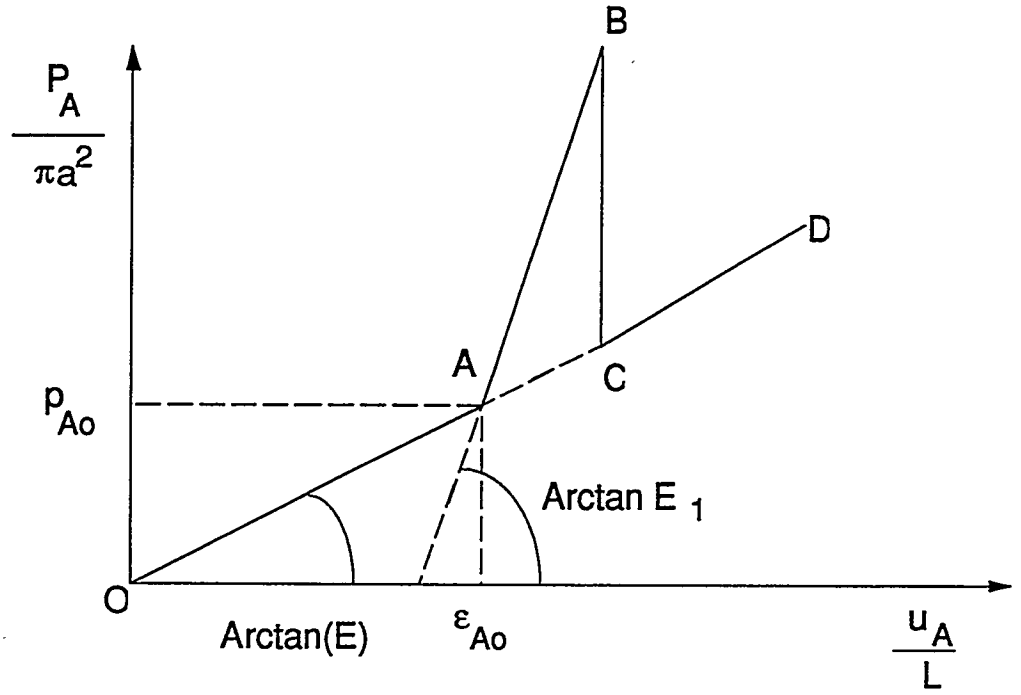

Fig. 6. Calculated idealized load-displacement curve.

AB with slope E_1. After bursting of the ring at B, the load rapidly drops to C and follows the original load-displacement curve for the plug along CD. In reality, the discontinuous changes in slopes are replaced by gradual changes.

The measured values of the slopes, based on three tests are

$$E = (2.455 \pm 0.136) \text{ MPa}$$

$$E_1 = (27.67 \pm 1.097) \text{ MPa}$$

Using Eq. 8, we find that

$$E_y = (1.2703 \pm 0.037) \text{ MN/m.}$$

The stiffness properties (E_x, E_y, etc.) of the composite substrate tube (without filter layer) can be estimated from the measured values of the matrix and fiber properties. With known values of stiffness (E_y) for the composite filter (composite tube and filter layer) and composite substrate alone, elastic properties of the filter layer can be estimated. These

properties will be used to analyze global stresses (thermal stresses, etc.) in composite filters to predict filter performance.

ACKNOWLEDGMENTS

The work was supported by the U.S. Department of Energy, Office of Fossil Energy, Advanced Research and Technology Materials Program [DOE/FE AA 15 10 10 0, Work Breakdown Structure Element ANL-1A], under Contract W-31-109-Eng-38. The authors thank D. J. Pysher, B. L. Weaver, and R. G. Smith of the 3M Company, J. A. Chambers of DuPont Lanxide Composites, Inc., P. Eggerstedt and J. Zievers of the Industrial Filter & Pump Manufacturing Company, R. A. Wagner and R. W. Goettler of Babcock & Wilcox, and John Sawyer of Pall Corporation for providing filter specimens and for their helpful discussions.

REFERENCES

1. J. P. Singh, S. Majumdar, A. S. Wagh, T. Wenzel, and R. B. Poeppel, "Materials Qualification Technology for Ceramic Cross-Flow Filters," Argonne National Laboratory Report ANL/FE-91/1 (July 1991).

2. E. A. Ripperger and N. Davis, "Critical Stress in Circular Ring," Trans. Amer. Soc. Civ. Engr., Paper No. 2308, pp. 619-35 (1948).

3. J. P. Singh, D. Singh, and M. Sutaria, "Effects of Flaws on Fracture Behavior of Structural Ceramics," in this Proceedings.

4. M. G. Stout and J. J. Petrovic, "Multiaxial Loading Fracture of Al_2O_3 Tubes: I, Experiments," J. Am. Ceram. Soc., 67[1] 14-18 (1984).

5. O. M. Jaddan, D. L. Shelleman, J. C. Conway, Jr., J. J. Mecholsky, Jr., and R. E. Tressler. "Prediction of the Strength of Ceramic Tubular Components: Part I-Analysis," J. Testing and Evaluation, 19 [3] 181-191 (1991).